ASSIMILATION OF SATELLITE AND RADAR DATA INTO MESOSCALE PREDICTION MODELS
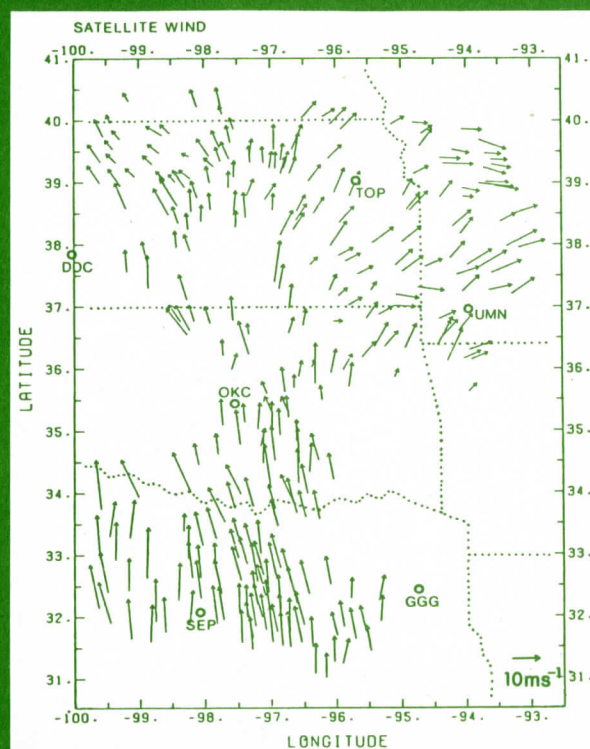
D. D. Houghton, Principal Investigator

FINAL TECHNICAL REPORT

Contributions by

W. H. Campbell	D. K. Lee
G. R. Diak	S. S. Lindstrom
P. L. Earl (Mlynczak)	A. Nierow
D. D. Houghton	N. D. Reynolds
R. A. Hyde	G. F. Sill
K. A. Jungbluth	B. L. Slye (Rotter)
M. W. Kalb	

Department of Meteorology
University of Wisconsin—Madison
1225 W. Dayton Street
Madison, Wisconsin 53706

Submitted June 15, 1986

This Report is submitted to satisfy the
National Science Foundation requirements
of a Final Technical Report
for Grant ATM-805369

Principal Investigator   David D. Houghton

June 15, 1986

TABLE OF CONTENTS

I. INTRODUCTION

This report provides a technical summary of the project supported by research grant NSF ATM-805369. The wide scope of the project is evident in the range of scientific problems addressed and in the large number of students supported. Specifically, four published papers, six conference papers, two Ph.D. theses and five M.S. theses resulted from the project and two other related Ph.D. theses were partially supported. An overview of the specific scientific accomplishments is presented here. The details of the science can be found in the written papers and theses. For convenience copies of the publications, conference preprints and theses abstracts are included at the end of this report.

II. Nontechnical Summary (from NSF Form 98A)

The extraction of useful data fields and physical insights from the growing number of atmospheric mesoscale observations was investigated with a wide range of studies. The research emphasized perspectives relevant to numerical simulation models recognizing the key role of modeling in mesoscale analysis.

Specifically, the work dealt with the production and analysis of mesoscale information from satellite and radar data, model initialization and data assimilation, impact analysis of such data on model simulations, model simulation quality evaluation, and mesoscale phenomena. Comprehensive mesoscale data sets for tropospheric temperature and low level winds were derived from satellite information and compared with conventional rawinsonde observations. Several objective analysis techniques were tested on the highly spatially nonuniform mesoscale wind data sets. Historical sequences of radar image data were analyzed to determine size, shape and evolution characteristics of mesoscale structures involving precipitation. Both directly analyzed and modified (filtered) data fields were tested for model input using either insertion at one time or

"nudging" into the model over a finite time interval. Impacts of input information for wind, temperature and moisture respectively on model simulation were isolated by model diagnostic and intercomparison studies. Evaluation of model simulation quality was done with the limited verification data available. Theoretical and numerical studies of gravity inertial waves helped to identify relevant properties of this important mesoscale phenomenon.

Results showed that meaningful mesoscale representation can be obtained from current data sources such as satellites. However, the primary contribution of the studies was identifying the enormity and complexity of the task for realizing routine, dependable, and meaningful data fields from mesoscale observations.

III. Technical Description of Project and Results

This project extended mesoscale studies begun in 1975 under NSF Grant ATM-7503617 and continued with NSF Grant ATM-7720231. Satellite data considerations were emphasized but radar data, numerical model experiments and studies of mesoscale phenomena were also included. As noted above an important contribution of the work was to enlarge our understanding of the many complexities involved with mesoscale meteorology research.

The technical summary that follows is subdivided according to topical areas to facilitate understanding. These areas generally correspond to the sub-topics in the original proposal.

A. Production and analysis of data

1. Satellite cloud winds

The basic low level mesoscale wind data derived for May 20, 1977 over the central U.S. by Lee (1981) and presented at conferences, Lee and Houghton, 1981a and b) were expanded to cover a larger area and examined in detail for

error particularly that related to height assignment uncertainty. It was found that the height error can introduce variability into the horizontal fields comparable to, but not obliterating, that expected in natural mesoscale phenomena with 100 km horizontal length scales (Lee and Houghton, 1984a). The random component of this error can be reduced by averaging, possible because of the large data density. Details of the random component and its reduction with area averaging were examined by computing root mean square and mean vector differences between satellite wind data and rawinsonde observations.

The objective analysis of the highly non-uniform May 20, 1977 data set was attempted with five different methods (Lee and Houghton, 1984a). There was a large variation in results with differences being comparable to those expected from other error sources.

2. Satellite temperature soundings

High density TIROS-N satellite temperature profiles over the central United States for April 10, 1979 were compared to the high density SESAME radiosonde observations (Kalb 1983). Average RMS differences were typically 1.5°K with a maximum around 2°C at the tropopause level. The satellite data show a cold bias in the middle troposphere and horizontal temperature gradients larger than those from the SESAME data. Although basic patterns were similar in the two data sets, there were significant regional differences. Nevertheless, both data sets described important sub-synoptic scale structure linked with subsequent mesoscale evolution including the precipitation systems.

Moisture fields were also derived from the satellite soundings in order to obtain an exclusively satellite-based data set for model initialization. However, these were not subjected to the quality examination given the temperature data.

The satellite temperature and moisture data were more evenly spaced than the satellite wind data, so the objective analysis procedure was not considered an important matter for separate study.

3. Radar data

Several analyses were performed on National Weather Service radar image data to investigate the correspondence of precipitation area evolution to concurrent synoptic and lower boundary conditions.

In the first analysis (Sill, 1981), the detailed relationship of precipitation bands to the dynamical and thermodynamical structure of the atmosphere was determined for the extratropical cyclone system in the U.S. Midwest April 3-4, 1974. Morphology details such as band dimensions, orientation and movement were determined from a time sequence of images. The relationship of the rain bands to the warm front showed some consistency with that in theoretical instability models.

In the second study (Slye, 1985) image data for a 7-year sequence of Novembers covering Lake Michigan and the area to the west were analyzed for morphology details of the precipitation areas and systematic differences between the land and lake areas that could be attributed to differences in the lower boundary conditions. Little systematic difference was found. There was reasonable correlation between echo movement and 700 mb winds over both areas.

4. Other data analysis studies

In a Ph.D. research program only peripherally related to this project, an intercomparison was made of basic objective analysis methods used in the National Weather Service numerical weather prediction systems (Nierow, 1983). Specifically, the optimal interpolation, Cressman, and Hough function methods were applied to common observational data sets for two case studies in January 1977. Important differences in the analysis for the lower tropospheric humidity fields were found. The precipitation forecasts were found to be sensitive to the initialization.

Smoothing procedures for initialization and data analysis were explored in several studies. Low-pass and band-pass filters helped to delineate the scale dependency of model impacts (Lee and Houghton, 1984b). A strong low-pass filter was used to produce initial data fields with only synoptic scale content to complement fields containing both synoptic and mesoscale for model impact studies (Earl, 1985; Mlynczak, Diak and Houghton, 1986).

B. Model initialization and data assimilation

Although this project did not focus on model initialization, several initialization and assimilation methods were used and additional experience with mesoscale (and subsynoptic scale) initialization was gained.

Effects of "nudging" (inserting observational data over a finite time interval) when the input data was very incomplete (e.g., low level satellite winds over only part of the model domain) were found to include high-frequency, large-scale pressure oscillations (Lee and Houghton, 1984b). However, in another experiment where observed surface winds were used to nudge the lower layers of a model over the whole domain and for a longer time period (90 instead of 30 minutes) such a pressure oscillation was not dominant and, in fact, the overall surface pressure forecast was improved in a case where initialization at all higher levels had been done with satellite data (Kalb, 1983).

General intercomparison of static initialization methods was made for the April 10, 1979 case study by using actual winds, balanced winds, and balanced winds with quasi-geostrophic divergence, respectively, for initial states (Kalb 1983). It was found that the balanced wind initial state gave both reduced initial noise and better subsequent surface pressure forecasts compared to the actual wind initial state. The addition of the quasi-geostrophic divergent component had little effect.

C. Model Impacts

Model intercomparison experiments made it possible to isolate impacts of satellite derived data on mesoscale simulations. These impacts were considered independently of simulation improvement or degradation based on verification data. In all cases the general quality of the simulation was reasonable. The impacts for satellite winds were considered separately from those for satellite temperature and moisture information.

1. Satellite wind impacts

The May 20, 1977 case was simulated with the 35 km horizontal grid version of the Drexel University comprehensive mesoscale model (LAMPS). Experiments made with and without the satellite wind information but with the same initial pressure, temperature, and moisture data clearly depicted the impact of this data (Lee, 1981 and Lee and Houghton, 1981a and b, 1984b).

The impact was characterized by considerable noise since the satellite data was only at low levels and over only part of the horizontal domain and initialized without any adjustment in the mass field specification. This was true even for the nudging initialization mentioned above in which an additional large scale high frequency wave component was introduced. This situation emphasized impacts expected from significantly unbalanced states which may be present, but less evident, in cases with more complete initial mesoscale data sets.

The divergent and non-divergent components of velocity were analyzed separately. Two horizontal scale ranges were examined corresponding to "large" and "small" mesoscale, the latter being in the 150-400 km wavelength range. The divergent winds characterized the noise component (free-mode-type inertial gravity waves). It was shown that the "small" scale noise component became dissipated/dispersed within 30 min whereas the "large" scale was not dissipated/dispersed until about 3 hours (the inertial frequency time scale). The "signal"

(more-enduring) component was monitored by the non-divergent velocity. Here information in the satellite winds could be identified throughout the entire 6-hour forecast for both scale ranges.

Overall impacts on the simulation, including the precipitation features, were minimal. The development and evolution of the dominant mesoscale structures that developed after the initial time were the same in both cases except for some differences in the amplitude. A pronounced "large" scale divergence feature in the satellite wind data, which did persist up to 3 hours, suppressed slightly precipitation in the area of the divergence during the 3-hour period.

2. Satellite temperature and moisture

Simulations were made for the April 10, 1979 case again using the 35 km horizontal resolution mesoscale model (LAMPS). Primary attention was given to the temperature. Experiments using the satellite information were compared with those using data from the enhanced SESAME rawinsonde network (Kalb, 1983; Kalb and Houghton, 1983). Generally complete initial data fields were obtained from the satellite information by utilizing balanced winds derived from the mass (temperature) data. The impact was measured primarily by the model forecast evaluation discussed in the next section rather than noise-type elements in model intercomparisons. It was shown that the satellite derived information was adequate in itself to initialize the mesoscale aspects of the case study.

In a separate study the impact of the mesoscale content of satellite temperature and moisture data was isolated by comparing a numerical simulation where the full satellite data set was compared to one where the mesoscale component was removed (Earl, 1985; Mlynczak, Diak and Houghton, 1986). The Australian mesoscale model (SSM) with 67 km horizontal resolution was used. It was clearly shown that predicted rainfall amounts were reduced when the initial mesoscale structure was omitted.

D. Model evaluation

In two case studies, sufficient mesoscale verification information was available so that performance of the LAMPS mesoscale model could be examined. In both cases much of the mesoscale structure developed after the initial time, particularly for precipitation. In the second case it was possible to identify the relative merits of a satellite-data-only initial state.

A detailed analysis of the structure and environment of the simulated convective precipitation band, "squall line", for the May 20, 1977 severe weather day in the U.S. Midwest was made for a large number of dynamical and thermodynamical variables (Jungbluth, 1981). For many of the variables correspondence to idealized or observed squall line structure was found. However, the vertical tilt of the structures tended to be "downstream" (in the direction of movement) in the model in contrast to observed squall lines. This suggested that some basic energy transfers might be of the wrong sign.

Analyses were made for model simulations of the April 10, 1979 severe weather case (Kalb, 1983 and 1985). Observations showed a well-defined precipitation band associated with a short wave trough in the 700 mb height field as well as an intense squall line which produced severe weather (including the Wichita Falls tornado). The model simulation was remarkably good for the precipitation band representing correctly both the movement and vertical tilt of the structure. The simulation made using the satellite data alone to define the initial state also reproduced these features. Simulation for the squall line was far less satisfactory for both the conventional data and satellite data initialization. The relative roles of subgrid (convective) and grid-scale precipitation in both precipitation systems were quite different in the forecasts from these two initializations highlighting the very sensitive nature of the hydrological cycle in the mesoscale model.

E. Mesoscale description, dynamics and theory

Advances in mesoscale meteorology depend upon advances in the observational data base, modeling, and analysis focused on the physical phenomena, themselves. Although the primary emphasis of this research was on the data and modeling aspects, there were a number of results concerning the mesoscale phenomena.

The radar image analyses (Sill, 1981, and Slye, 1985) provided morphological description of precipitation systems and details on their relationship to wind flow and thermodynamic properties of the atmosphere. The qualitative nature of the radar data precluded study of the structure of the precipitation systems and associated dynamical processes.

Some basic dynamical properties of precipitation systems were identified in several studies. Vertical cross-section analysis showed the apparently erroneous upstream tilt in the May 20, 1977 squall line simulated by the LAMPS model (Jungbluth 1983). A similar upstream tilt was found in the precipitation band modeled for April 10, 1979 (Kalb, 1983; Houghton, 1984; Kalb, 1985). However, in this case the band was in a general baroclinic zone and the tilt was consistent with that expected from symmetric instability theory. A symmetric instability theory index was calculated for the 1979 case and shown to correlate with the growth characteristics of the band (Lindstrom, 1984; Lindstrom and Houghton, 1985). The band showed development where the index was small (denoting instability conditions) and weakening where the index was larger (denoting stability with respect to symmetric circulations).

The dynamics of inertial gravity waves were investigated in two theoretically oriented studies. Simulations with a two layer model were analyzed to isolate the inertial gravity wave component associated with a propagating jet

stream maximum. The inertial gravity wave structure tended to remain with the jet and not to propagate away indicating dynamical linkages between inertial gravity and quasigeostrophic phenomena (Houghton, Campbell and Reynolds, 1981). Interactions between inertial gravity waves and mean flow were studied with a one-layer model experiment (Hyde, 1982). Results isolated the effects of mean shears on the structure of normal mode waves and equilibria in the mean flow that included wave-mean flow interactions.

Houghton, D.D., W.E. Campbell, and R.R. Reynolds, 1981. Isolation of the gravity-inertial motion component in a nonlinear atmospheric model. J. Atmos. Sci., 109, 2133-2150.

Hyde, R., 1982. On the interactions between inertia-gravity normal modes and geostrophic currents in a simple fluid model. Ph.D. Thesis, Dept. of Meteorology, University of Wisconsin, 335 pp.

Langblarh, E.A., 1983. "An evaluation of mesoscale model results for squall line structure, dynamics and environment". M.S. Thesis, Dept. of Meteorology, University of Wisconsin, 130 pp.

Kalb, M.W., 1983. "Initialization of a mesoscale model for April 10, 1979 using alternate data sources." Ph.D. Thesis, Dept. of Meteorology, University of Wisconsin, 230 pp.

Kalb, M.W., 1985. Results from a limited area mesoscale numerical simulation for 10 April 1979. Mon. Wea. Rev., 113, 1644-1662.

Kalb, M. and D.D. Houghton, 1983. "Mesoscale model simulations for the 10 April 1979 SESAME case." Oral presentation at First AMS Conference on Mesoscale Meteorology, Norman, OK, May 31 - June 3, 1983.

Lee, D.K., 1981. Impact of mesoscale satellite wind data on numerical model simulations. Ph.D. Thesis, Dept. of Meteorology, University of Wisconsin, 110 pp.

Lee, D.K. and D.D. Houghton, 1981a. Utilizing satellite wind data in a mesoscale numerical model. Proceedings IAMAP Symposium, Hamburg, 25-28 August 1981 (ESA SP-165, June 1981), pp. 265-270.

Lee, D.K. and D.D. Houghton, 1981b. Impact of mesoscale satellite wind data on numerical model simulations. Preprint Volume: Fifth Conference on Numerical Weather Prediction, Nov. 2-6, 1981, Monterey, California, American Meteorological Society, Boston, Mass., pp. 171-175.

Lee, D.K., and D.D. Houghton, 1984a. A quantitative study of satellite winds for mesoscale meteorology. Mon. Wea. Rev., 112, 990-1004.

F. References for technical description

Earl (Mlynczak), P.L., 1985. "Impact of the initial specification of moisture and vertical motion on precipitation forecasts with a mesoscale model." M.S. Thesis, Dept. of Meteorology, University of Wisconsin, 87 pp.

Houghton, D.D., 1984. "Mesoscale structure and dynamics of precipitation producing weather systems." Oral presentation at International Conference on Mesoscale Meteorology, Melbourne, Australia, Feb. 6-10, 1984. Australian Royal Meteorological Society and American Meteorological Society.

Houghton, D.D., W.H. Campbell, and N.D. Reynolds, 1981. Isolation of the gravity-inertial motion component in a nonlinear atmospheric model. J. Atmos. Sci., 109, 2118-2130.

Hyde, R., 1982. On the interactions between inertia-gravity normal modes and geostrophic currents in a simple fluid model. Ph.D. Thesis, Dept. of Meteorology, University of Wisconsin, 129 pp.

Jungbluth, K.A., 1983. "An evaluation of mesoscale model results for squall line structure, dynamics and environment". M.S. Thesis, Dept. of Meteorology, University of Wisconsin, 130 pp.

Kalb, M.W., 1983. "Initialization of a mesoscale model for April 10, 1979 using alternate data sources." Ph.D. Thesis, Dept. of Meteorology, University of Wisconsin, 230 pp..

Kalb, M.W., 1985. Results from a limited area mesoscale numerical simulation for 10 April 1979. Mon. Wea. Rev., 113, 1644-1662.

Kalb, M. and D.D. Houghton, 1983. "Mesoscale model simulations for the 10 April 1979 SESAME case." Oral presentation at First AMS Conference on Mesoscale Meteorology, Norman, OK, May 31 - June 3, 1983.

Lee, D.K., 1981. Impact of mesoscale satellite wind data on numerical model simulations. Ph.D. Thesis, Dept. of Meteorology, University of Wisconsin, 110 pp.

Lee, D.K. and D.D. Houghton, 1981a. Utilizing satellite wind data in a mesoscale numerical model. Proceedings IAMAP Symposium, Hamburg. 25-28 August 1981 (ESA SP-165, June 1981), pp. 265-270.

Lee, D.K. and D.D. Houghton, 1981b. Impact of mesoscale satellite wind data on numerical model simulations. Preprint Volume: Fifth Conference on Numerical Weather Prediction, Nov. 2-6, 1981; Monterey, California, American Meteorological Society, Boston, Mass., pp. 171-178.

Lee, D.K., and D.D. Houghton, 1984a. A quantitative study of satellite winds for mesoscale meteorology. Mon. Wea. Rev., 112, 990-1004.

Lee, D.K., D.D. Houghton, 1984b. Impact of mesoscale satellite wind data on numerical model simulations. Mon. Wea. Rev., 112, 1005-1016.

Lindstrom, S.S., 1984. "Analysis of mesoscale model results using a bandpass filter." M.S. Thesis, Dept. of Meteorology, University of Wisconsin, 138 pp.

Lindstrom, S.S. and D.D. Houghton, 1985. "Correspondence between moist convective activity and a symmetric instability index in a mesoscale numerical model simulation." Oral presentation at Second AMS Conference on Mesoscale Meteorology, Pennsylvania State University, June 3-7, 1985.

Mlynczak, P.E., G.R. Diak and D.D. Houghton, 1986. Impact of the initial specification of moisture and vertical motion on precipitation forecasts with a mesoscale model - implications for a satellite mesoscale data base. Preprint Volume Second Conference on Satellite Meteorology/Remote Sensing and Applications, May 12-16, 1986; Williamsburg, Virginia, American Meteorological Society, Boston, Mass., pp. 136-141.

Nierow, A., 1983. "A comparison of NMC models (1977) on precipitation forecasts for East Coast cyclogenesis." Ph.D. Thesis, Dept. of Meteorology, University of Wisconsin, 316 pp.

Sill, G.F., 1981. Rainbands ahead of a warm front: A case study. M.S. Thesis, Dept. of Meteorology, University of Wisconsin, 108 pp.

Slye (Rotter), B.L., 1985. "A radar study of mesoscale precipitation areas over Wisconsin and Lake Michigan in late autumn." M.S. Thesis, Dept. of Meteorology, University of Wisconsin, 82 pp.

IV. Publication and Conferences Summary

A. Journal Papers

Houghton, D.D., W.H. Campbell, and N.D. Reynolds, 1981. Isolation of the gravity-inertial motion component in a nonlinear atmospheric model. J. Atmos. Sci., 109, 2118-2130.

Kalb, M.W., 1985. Results from a limited area mesoscale numerical simulation for 10 April 1979. Mon. Wea. Rev., 113, 1644-1662.

Lee, D.K., and D.D. Houghton, 1984a. A quantitative study of satellite winds for mesoscale meteorology. Mon. Wea. Rev., 112, 990-1004.

Lee, D.K., D.D. Houghton, 1984b. Impact of mesoscale satellite wind data on numerical model simulations. Mon. Wea. Rev., 112, 1005-1016.

B. Conference Presentations
(Published preprints for 3rd, 4th and 6th papers listed)

Houghton, D.D., 1984. Mesoscale structure and dynamics of precipitation producing weather systems. International Conference on Mesoscale Meteorology, Melbourne, Australia, Feb. 6-10, 1984. Australian Royal Meteorological Society and American Meteorological Society.

Kalb, M. and D.D. Houghton, 1983. Mesoscale model simulations for the 10 April 1979 SESAME case. First AMS Conference on Mesoscale Meteorology, Norman, OK, May 31 - June 3, 1983.

Lee, D.K. and D.D. Houghton, 1981a. Utilizing satellite wind data in a mesoscale numerical model. Proceedings IAMAP Symposium, Hamburg. 25-28 August 1981 (ESA SP-165, June 1981), pp. 265-270.

Lee, D.K. and D.D. Houghton, 1981b. Impact of mesoscale satellite wind data on numerical model simulations. Preprint Volume: Fifth Conference on Numerical Weather Prediction, Nov. 2-6, 1981; Monterey, California, American Meteorological Society, Boston, Mass. pp. 171-178.

Lindstrom, S.S. and D.D. Houghton, 1985. Correspondence between moist convective activity and a symmetric instability index in a mesoscale numerical model simulation. Second AMS Conference on Mesoscale Meteorology. Penn State June 3-7, 1985.

Mlynczak, P.E., G.R. Diak and D.D. Houghton, 1986. Impact of the initial specification of moisture and vertical motion on precipitation forecasts with a mesoscale model - implications for a satellite mesoscale data base. Preprint Volume: Second Conference on Satellite Meteorology/ Remote Sensing and Applications, May 12-16, 1986; Williamsburg, Virginia, American Meteorological Society, Boston, Mass., pp. 136-141.

C. Student Degrees

1. Ph.D. Theses

Hyde, R., 1982. On the interactions between inertia-gravity normal modes and geostrophic currents in a simple fluid, 129 pp.

Kalb, M.W., 1983. "Initialization of a mesoscale model for April 10, 1979 using alternate data sources." 230 pp.

Lee, D.K., 1981. Impact of mesoscale satellite wind data on numerical model simulations. 110 pp.

Nierow, A., 1983. "A comparison of NMC models (1977) on precipitation forecasts for East Coast cyclogenesis." 316 pp.

2. M.S. Theses

Earl (Mlynczak), P.L., 1985. Impact of the initial specification of moisture and vertical motion on precipitation forecasts with a mesoscale model. 87 pp.

Jungbluth, K.A., 1983. "An evaluation of mesoscale model results for squall line structure, dynamics and environment." 130 pp.

Lindstrom, S.S., 1984. "Analysis of mesoscale model results using a bandpass filter." 138 pp.

Sill, G.F., 1981. Rainbands ahead of a warm front: A case study. M.S. Thesis, Dept. of Meteorology, University of Wisconsin, 108 pp.

Slye (Rotter), B.L., 1985. A radar study of mesoscale precipitation areas over Wisconsin and Lake Michigan in late autumn. 82 pp.

V. Data on Scientific Collaborators

A. Scientific Staff

Dr. George R. Diak, Scientist, Space Science and Engineering Center,
      University of Wisconsin-Madison

Dr. David D. Houghton (PI), Department of Meteorology,
      University of Wisconsin-Madison

Dr. Dong K. Lee, Project Associate, Department of Meteorology,
      University of Wisconsin-Madison

B. Students

William H. Campbell
Pamela L. Earl (Mlynczak)
Glenn A. Field (Thesis not completed yet)
Richard A. Hyde
Karl A. Jungbluth
Michael W. Kalb
Scott S. Lindstrom
Alan Nierow
Nathaniel D. Reynolds
Gordon F. Sill
Barbara L. Slye (Rotter)

VI. Abstracts of Theses   (Given in the order listed in IV.C)

Hyde, Richard Alexander, 1982: On the interaction between inertia-gravity normal modes and geostrophic currents in a simple fluid model.

Ph.D. Thesis.

ABSTRACT

The interaction between a zonally averaged mean current and an inertia-gravity wave perturbation is examined during the evolution of a geophysical fluid from an initial state of imbalance. The problem is modeled with the shallow water equations confined to a channel on a tangent plane with constant rotation. The nonlinear zonal current (initially geostrophic) and the linear inertia-gravity wave (initially a periodic normal mode of the current) are integrated simultaneously using standard, numerical finite difference techniques. The results indicate that the physics of their interaction can be found alternatively by calculating the inertia-gravity normal mode compatible with the initial geostrophic current and then calculating the current's (steady state) equilibria consistent with the forcing of the nonlinear wave advections.

For a variety of currents and for various scales, numerical computations show how stable inertia-gravity normal modes are deformed from their pure Kelvin and pure Poincare structures by the shear and the depth variations of their mean state environments; this alteration is quite small for long waves but increases with zonal wavenumber. Because these channel normal modes are standing waves, certain wave advections and stresses vanish identically. Consequently, two significant results are found: First, there can be no absorption of wave momentum by the mean current even at a critical line. However, the singularity at $c = U \pm (gH)^{1/2}$ and two associated turning points may produce a caustic (total wave reflection) in which case the wave is trapped between the caustic and the channel wall. Second, the waves only indirectly interact with the zonal current via the secondary circulations of the mean state; that is, to first order, there is no wave-mean current interaction.

The action of the waves on the mean current produces equilibria which are ageostrophic and which obey the scale law of classical geostrophic adjustment: mass adjusts at small scales; velocity, at large scales. A conserved potential vorticity can be defined which specifies the rearrangement of mass and momentum in the mean current to balance the forcing due to the wave.

Kalb, Michael W., 1983: Initialization of a mesoscale model for April 10, 1979 using alternative data sources. Ph.D. Thesis.

ABSTRACT

A 35 km grid limited area mesoscale model was initialized with high density SESAME radiosonde data and high density TIROS-N satellite temperature profiles for April 10, 1979. These data sources were used individually and with low level wind fields constructed from surface wind observations.

The primary objective was to examine the utility of satellite temperature data for initializing a mesoscale model by comparing the forecast results with similar experiments employing radiosonde data. The impact of observed low level winds on the model forecasts was also investigated with experiments varying the method of insertion. All forecasts were compared with each other and with mesoscale observations for precipitation, mass and wind structure.

Preliminary forecasts initialized with radiosonde winds and balanced winds showed that balanced winds substantially reduced initial model shock and provided smoother and more accurate mass fields.

The radiosonde and satellite precipitation forecasts differed significantly although both had some very realistic qualities. A low level short wave which was present in both the radiosonde and satellite initial states was retained by the model and propagated around the synoptic scale trough from Oklahoma to Nebraska. The radiosonde short wave was associated with a mesoscale precipitation band that verified with a short wave band evident in radar and SESAME radiosonde observations. The satellite short wave showed a weaker association with a precipitation band, however, the satellite forecast gave a slightly better depiction of convective precipitation over Oklahoma, exhibiting the same general location and orientation as observed.

Continuous insertion of low level winds during the initialization period had impacts on mass, wind and precipitation fields. The most dramatic was an improvement in sea level pressure patterns by reducing the fast eastward propagation of the mass field experienced in other forecasts.

The model simulated several additional mesoscale features including intensification of a low level dry line and generation of a low level jet. Several forecasts produced convective precipitation systems with characteristics satisfying criteria for a mesoscale convective complex.

The study demonstrated that high density satellite temperature data and balanced winds can be used in a mesoscale model to produce forecasts which verify favorably with observations.

Lee, Kong Kyou, 1981: Impact of mesoscale satellite wind data on

numerical model simulations. Ph.D. Thesis.

ABSTRACT

The initialization of a comprehensive mesoscale numerical prediction
model is investigated using actual high-spatial-resolution satellite wind obser-
vations. Attention is focused on the impacts of this mesoscale data as part of
an initial specification for a dynamical numerical model and on the use of
diagnostic methods to assess the forecast impacts.

Comparisons of the satellite wind data to special 1800 GMT rawinsonde
observations provide some confidence in satellite winds and thus in the
mesoscale features defined by these winds. Four objective analysis methods are
tested on these data to determine sensitivity to analysis procedure. It is
possible to obtain reasonable gridded data sets with the data containing large
spatial variation in density.

Four six-hour forecast experiments are made with the Drexel University/
NCAR mesoscale prediction model with 35 km horizontal resolution to examine the
assimilation characteristics of the mesoscale wind data. Both initially imposed
and gradually imposed insertion techniques are tested. The initial mass field
in the test experiments is the same as in the control forecast. Numerous
diagnostic methods are made for assessing forecast impact of the inserted wind
data.

The primary impact of the inserted data is to alter the amplitude of
mesoscale features developed in the control. The gradually imposed insertion
technique in contrast to the initially imposed insertion produces the larger
local extrema and an extra spurious external mode pressure oscillation. The
divergence signal for the inserted data is lost after 1/2 h for the smaller
mesoscale component and by 3 h for the larger mesoscale component. The vor-
ticity signal persists for the entire 6 h period for both scale components.
Assimilation of the satellite wind data into the model proceeds according to
recognizable adjustment processes with time scales of 3 h and 1/2 h depending
on motion scales. Changes in the 1 to 3 h precipitation forecasts due to the
insertion data exist and are not evident after 3 h.

Nierow, Alan, 1983: A comparison of NMC models (1977) on precipitation forecasts for east coast cyclogenesis. <u>Ph.D. Thesis.</u>

ABSTRACT

The 9 Layer Global (9LGLB), 7 Layer Primitive Equation (7LPE) and Limited Fine Mesh (LFM) models are evaluated with respect to their accuracy in predicting precipitation associated with two east coast winter storms. Various forecast model fields are examined in order to determine the causes for model errors. The models' 700 mb postprocessed vertical motion fields are compared to the vertical motion fields calculated from Quasi-Geostrophic theory. The LFM is initialized with different analysis schemes in order to determine what effect this has on rainfall forecasts. A new convective algorithm is introduced into the LFM in order to emulate more realistically the convective precipitation from the real atmosphere.

The results from this study reveal that in comparison with the 9LGLB model, both the 7LPE and especially the LFM are more accurate with their respective precipitation forecasts. The model's postprocessed vertical motion field is significantly different in comparison to the vertical motion field calculated from QG theory. The results from employing different analysis schemes in the LFM are inconclusive in deciding which analysis methods to employ in this model. The new convective algorithm improves the LFM precipitation forecasts during the occluding stage of each case and yet, for the developing and maturing stages, this new method actually impairs the LFM's rainfall forecast.

This thesis provides valuable insight into what elements contribute to the models over or under-forecasting the areal size and amounts of precipitation associated with an east coast winter storm. The elements are:
1. The models' sigma boundary layer (lowest 50 mb) relative humidity forecast fields.
2. The erroneous sea surface temperatures used as input into the numerical models.
3. The models' 500 mb vorticity advection and surface to 500 mb relative humidity fields.

The inability of the models' to accurately predict the correct rainfall is caused predominately by the large scale precipitation component being in error. From the results obtained in this thesis, various recommendations are suggested in order to improve the precipitation forecasts from NMC numerical models that are associated with east coast storms.

Earl, Pamela Lynn, 1985: Impact of the initial specification of moisture and vertical motion on precipitation forecasts with a mesoscale model. M.S. Thesis.

ABSTRACT

Four simulations are made with a numerical mesoscale model to determine the effects of suppressing the initial mesoscale information in the moisture and wind fields on the precipitation forecasts. The second half of a 12-hour control forecast represents the ideal reference forecast. This reference forecast can be thought of as being "initialized" with fields from the six-hour control forecast that contain both mesoscale and synoptic scale features. The first experiment is initialized with the same six-hour control forecast, but the moisture fields are smoothed to eliminate the mesoscale component. The horizontal wind fields are replaced with nondivergent winds in the second experiment, but all the other variables come from the six-hour control. This experiment therefore contains only a topographically-induced vertical motion field initially. The third experiment contains both smoothed moisture fields and nondivergent winds initially and is considered the experiment with the most degraded conditions.

All of the experiments' six-hour simulations produce less precipitation than the control forecast. Precipitation rates lag behind the control forecast, and areal coverage is generally less. The third experiment has the worst performance compared to the control, which is expected based on its initial conditions. The smoothed moisture experiment produces less precipitation than the nondivergent experiment in areas over the ocean where moisture magnitudes are reduced by the smoothing process. Over a land area, however, the smoothed moisture experiment forecasts more precipitation than the nondivergent experiment, although moisture magnitudes are reduced in that area also. Generally, the differences between the first two experiments' forecasts are not large enough to conclude whether either mesoscale moisture or initial vertical motion is more essential to precipitation forecasting with a mesoscale model.

Jungbluth, Karl Allan, 1983: An evaluation of mesoscale model results

for squall line structure, dynamics and environment. <u>M.S. Thesis.</u>

ABSTRACT

A detailed analysis of numerical model results has been carried out for
two case studies on May 20, 1977 and April 10-11, 1979. Atmospheric variables
representative of the environment favorable for organized convection have been
identified and examined in terms of scales, magnitudes and structures. The
small scale model grid spacing of 35 km allowed the close evaluation of horizon-
tal maps and cross sections of atmospheric variables, both within the squall
line regions and the surrounding environment. Relationships between forecast
parameters and the modelled convective precipitation rate were also discussed.

Parameters most closely related to the intensity and location of the con-
vective precipitation, as identified in the model results, were then compared
with parameters found to be closely linked to convection through observational
and theoretical work. The comprehensive nature of the model forecast fields
allowed the enhancement and clarification of our knowledge of squall line struc-
ture and environment.

Lindstrom, Scott Shipman, 1984: Analysis of mesoscale model results using a bandpass filter. <u>M.S. Thesis.</u>

ABSTRACT

A detailed diagnostic analysis of mesoscale model results for a numerical simulation of 10-11 April 1979 is performed using a 25-point bandpass filter to highlight mesoscale features. The numerical model has comprehensive physics and a fine mesh 35-kilometer grid. The correspondence of the locations of the meso-scale structures to regions of low value in a symmetric stability index field (where mesoscale circulations are theoretically most apt to occur) is examined to assess whether mesoscale circulations are generated in the model consistent with this theory. A Rossby number is computed for the flow field to determine if mesoscale features identified by the bandpass filter have a tendency to exist where the Rossby number is large in order to test the supposition that order one Rossby number defines the mesoscale. Classic meso- and synoptic scale theory is also tested against model results, and model representation of various mesoscale features is evaluated.

The model simulation has circulations that are indeed consistent with classic meso- and synoptic scale theory for the upper tropospheric jet streak, the low level jet, and the dry line. The relationship between small values of symmetric stability and initiation or continuation of convection is also strongly present in the model results. Adequate simulation of mesoscale phenom-ena commonly observed in the atmosphere allow for confidence in results.

Sill, Gordon Fredrick, 1981: Rainbands ahead of a warm front: A case study. M.S. Thesis.

ABSTRACT

A case study of mesoscale precipitation areas (rainbands) was performed for a storm which passed through the Midwest on 3, 4 April, 1974. Tracings from the PPI scope of seven radars were correlated to obtain an entire radar picture of each rainband's movement. Twenty-six rainbands were studied with respect to the wind, temperature, and moisture fields of the storm. The average rainband length was 386 km, the average width 38 km, and the average length-to-width ratio was 29:1. The average duration of a rain-band was about 5 hours.

The rainbands occurred in two "belts" one south and one north of the warm front. The rainbands would develop and grow at the southern end of the belt, travel to the northern end and stop. At the beginning of the storm the rainbands would dissipate when they reached the northern end of the belt, but as the storm progressed they did not dissipate, but rather began to "stack up" as each successively reached that end. Eventually, this produced a wide, stationary area of precipitation within each belt about 95-140 km wide and 185-650 km long. Thus the entire area north and south of the warm front became covered by a large stationary area of precipitation as is commonly associated with warm fronts as seen on radar.

The cloud layer in which the rainbands developed was between 14,000 and 16,000 feet asl. A potentially unstable layer was associated with the cloud layer and it is assumed that the rainbands were caused by the release of this instability as the air rose over the warm front. The greater majority of the rainbands moved to the left of the wind in the cloud layer. They did not move perpendicular to their orientation, but averaged 46° to it. The rainbands were approximately parallel to the warm front and were found to be approximately parallel with the shear vector in the cloud layer in accord with Asai's (1972) theory. About 50% of the rainbands had significant changes in their orientation as they travelled north, most rotating counterclockwise. A rainband signature in the surface pressure field was looked for, but not found.

The rainbands were found to have a systematic evolution, organization, and movement. The results were in agreement with the results and theories of other researchers throughout the world. This points to the general applicability of the results to cyclonic storms.

Slye, Barbara Linn, 1985: A radar study of mesoscale precipitation areas over Wisconsin and Lake Michigan in late autumn. <u>M.S. Thesis.</u>

ABSTRACT

Mesoscale radar echo systems passing over Wisconsin and Lake Michigan were analyzed from microfilm for the month of November for the years 1972-1978. Two categories of echoes, those over land and those over water, were defined. Echo velocity and area change were correlated with 700 mb wind velocity, horizontal divergence of surface layer moisture flux and total surface layer moisture supply and the results compared between the two categories to determine any lake effect on echo movement or growth. For each relationship no significant difference was found between the means of the two categories. Additional correlations were made for lake echoes between area change and vertical surface moisture flux, water temperature and surface stability.

Correlation coefficients ranging from .69 to .92 were found between echo movement and 700 mb wind velocity. However, correlations between area change and surface conditions were not as good with few significant correlation coefficients. If the size of the original data set was increased, results might be improved.

VII.   Copies of Publications and Conference Paper Preprints
        (Given in the order listed in IV. A and B.)

Isolation of the Gravity-Inertial Motion Component in a Nonlinear Atmospheric Model

DAVID D. HOUGHTON, WILLIAM H. CAMPBELL AND NATHANIEL D. REYNOLDS

Isolation of the Gravity-Inertial Motion Component in a Nonlinear Atmospheric Model

DAVID D. HOUGHTON, WILLIAM H. CAMPBELL[1] AND NATHANIEL D. REYNOLDS[2]

Department of Meteorology, University of Wisconsin, Madison 53706

(Manuscript received 10 September 1980, in final form 26 May 1981)

ABSTRACT

Diagnostic methods are considered for isolating gravity-inertial motions in the output of a nonlinear atmospheric numerical model. The gravity-inertial component is defined by the nongeostrophic motions not directly incorporated with the synoptic-scale evolution according to quasi-geostrophic or balance model relationships. The analysis methods are applied to the solutions for a propagating jet stream maximum generated by a simple two-layer hydrostatic numerical model. Results identify a coherent pattern in the gravity-inertial motion component but details of the horizontal structure and propagation characteristics are only partially resolved. Results also elucidate relative merits of a number of physical variables and difference fields for defining the gravity-inertial component.

1. Introduction

The existence of gravity-inertial waves in the spectrum of atmospheric motions has been recognized for a long time. They have been associated with a wide variety of subsynoptic-scale phenomena ranging from large mesoscale structures in the middle-latitude polar jet stream to smaller scale orographic and shear instability situations. They also show up as a noise component in numerical model simulations generated by inaccuracies in the initial conditions and approximations present in the mathematical representation of the atmosphere. Gravity-inertial waves are an essential part of the atmospheric adjustment process. Describing and understanding the adjustment process is fundamental to our understanding of larger scale atmospheric motions and to evaluating initialization procedures for numerical models. Despite all these factors that have provided interest in the gravity-inertial motion component, there remains the serious problem of actually identifying and describing this component both in real atmospheric observations and in numerical model output.

It is possible to think of large-scale atmospheric motions as consisting of two components. One is the quasi-geostrophic or balanced state which describes the general evolution of large-scale features. The other is the unbalanced gravity-inertial component which incorporates both adjustment processes of the large scale and structures with smaller scale energy sources. This subdivision is fundamental to analyses of geostrophic adjustment (Obukhov, 1949). Okland (1970) studied the linear geostrophic adjustment problem and alluded to the fact that in the general case, if a solution to the problem could be found, it would consist of the high-frequency gravity-inertial waves and also the balanced wind and mass fields. Blumen (1972) developed a linear model that was actually able to separate the gravity-inertial component from the quasi-geostrophic flow.

For the general nonlinear case, the definition of the gravity-inertial component is not a trivial matter. Normal mode analysis for global and hemispheric domains has been shown to be useful for cases where isolation of nonphysical high-frequency gravity-inertial waves is particularly important (Daley and Puri, 1980; Leith 1980). The definition of the normal modes is complicated for more local domain situations. Techniques of scale separation (Doswell, 1977; Maddox, 1980) also offer a means of isolating some gravity-inertial wave components. Nevertheless, an important class of fundamentally unbalanced gravity-inertial motions exist in conjunction with middle-latitude baroclinic jet flows for which simple frequency or space scale isolation is not likely to be effective because of frequency and phase distortions due to advective and shear flow dynamics.

The purpose of this paper is to examine a diagnostic methodology to identify and isolate gravity-inertial motions in the nonlinear case based on comparing fields with those derived from diagnostic filtered models. Such an approach offers a dynami-

[1] Current affiliation: Technical Services Division, Air Force Global Weather Central, Offutt Air Force Base, Omaha, NE 68113.

[2] Current affiliation: Department of Meteorology, Florida State University, Tallahassee, 32306.

cally meaningful and readily applied method for isolating the gravity-inertial component; however, it will not give a unique result considering the multiplicity of filtered models that can be used (e.g., quasi-geostrophic, balanced and semigeostrophic). The methodology is applied to a simple two-level primitive equation simulation for a jet stream. It is expected that the approach could be generalized to more comprehensive model output and real observations.

For such a simple model, it might be considered feasible to also isolate the gravity-inertial component by comparison of the primitive equation model solutions with those from a corresponding filtered model of prognostic type. This approach would have the advantage of including feedback effects of the gravity-inertial mode in terms of the evolutionary process. Nevertheless, such a method would have virtually unavoidable disadvantages of model incompatibility and resultant differences in the synoptic-scale component. In the diagnostic approach, on the other hand, the primitive equation model solutions themselves are analyzed according to filtered equation relationships, thus avoiding problems of model incompatibility.

The extent to which a comment on the classical atmospheric adjustment theory can be made from the results of this study is limited by the fact that the scale of motion considered is of comparable magnitude to the Rossby deformation radius. Thus, the limiting case of truly large or small scales of motion is not examined. The significant contribution of this study lies in the attempt to describe the character of the gravity-inertial component present in the evolving primitive equation model solution. It is not of interest whether this component was generated by initial imbalances or by the jet flow itself. The focus is on the capability of a method to identify and isolate any gravity-inertial component that is present regardless of its origin.

2. Basic primitive equation model

The model structure and basic variables are shown in Fig. 1. It is a two-layer hydrostatic and adiabatic model with constant Coriolis parameter and no viscosity.

The governing prognostic relationships are the equations of motion,

$$\frac{\partial \mathbf{V}_n}{\partial t} + \mathbf{V}_n \cdot \nabla \mathbf{V}_n - \left(\frac{\omega_n + \omega_{n+1}}{2\Delta p}\right)(\mathbf{V}_n - \mathbf{V}_{n+1})$$

$$+ f\mathbf{k} \times \mathbf{V}_n = -\nabla[\tfrac{1}{2}(\phi_n + \phi_{n+1})], \quad (1)$$

the thermodynamic "thickness" equation,

$$\frac{\partial}{\partial t}(\phi_{n+1} - \phi_n) + \mathbf{V}_n \cdot \nabla(\phi_{n+1} - \phi_n)$$

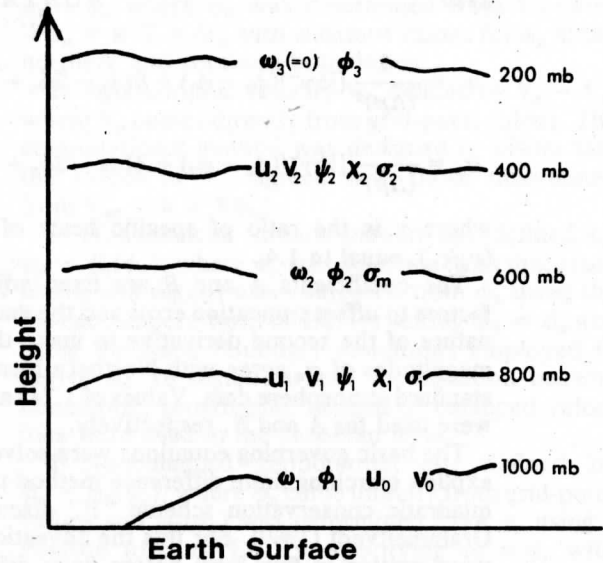$$+ \tfrac{1}{2}(\omega_n + \omega_{n+1})\sigma_n \Delta p = 0, \quad (2)$$

Fig. 1. Vertical structure and placement of variables in the model. Variables are defined in the text.

a special equation for the geopotential height of the lowest level derived from the integrated hydrostatic relationship, the definition of ω and assuming that mean values in the layer from the earth's surface to 1000 mb are given by values at 1000 mb,

$$\frac{\partial}{\partial t}\phi_1 + \mathbf{V}_0 \cdot \nabla \phi_1 = \frac{\omega_1}{\rho^*} - \phi_1(\nabla \cdot \mathbf{V}_0), \quad (3)$$

and the continuity equation,

$$\omega_n = \omega_{n+1} - (\nabla \cdot \mathbf{V}_n)\Delta p. \quad (4)$$

Variables are defined as follows with integer subscripts denoting location in the vertical as shown in Fig. 1:

t time

∇ horizontal gradient operator

n integer subscript with value of 1 or 2 denoting location in the vertical

$\mathbf{k}$ unit vector in the vertical

Δp vertical pressure thickness of a layer (equal to 400 mb in this study)

f Coriolis parameter (constant in this study)

$\mathbf{V}$ horizontal velocity vector with components of u and v in the east-west (x) and north-south (y) directions, respectively

ω "pressure" vertical motion (dp/dt)

ϕ geopotential

ρ^* mean density in the layer from the earth's surface to 1000 mb

σ static stability parameter.

In order to close the system additional relationships were used as follows:

$$\omega_3 = 0,$$
$$\mathbf{V}_0 = \tfrac{3}{2}\mathbf{V}_1 - \tfrac{1}{2}\mathbf{V}_2 \quad (5)$$

$$\sigma_1 = \frac{1}{(\Delta p)^2} [\tfrac{1}{2}\gamma^{-1}(\phi_2 - \phi_1) + B(\phi_3 - 2\phi_2 + \phi_1)], \quad (6)$$

$$\sigma_2 = \frac{1}{(\Delta p)^2} [\tfrac{1}{2}\gamma^{-1}(\phi_3 - \phi_2) + A(\phi_3 - 2\phi_2 + \phi_1)], \quad (7)$$

where γ is the ratio of specific heats of dry air (c_p/c_v), equal to 1.4.

The coefficients A and B are fixed adjustment factors to offset truncation error and the uncentered nature of the second derivative to make the mean magnitudes of σ_n agree with Northern Hemisphere standard atmosphere data. Values of 1.745 and 0.472 were used for A and B, respectively.

The basic governing equations were solved by an explicit marching finite difference method using the quadratic conservation scheme "F" discussed by Grammeltvedt (1969). For this the advection terms were written in flux form before finite differences were taken.

An east-west channel model with width 3800 km and length 4000 km was employed. Boundary conditions were periodic in x and the v component of velocity was set to zero at the channel walls. Initial conditions were defined by specifying a streamfunction at the 800 and 400 mb levels. The pressure variables were then determined using the balanced relationships given in Section 3 along with standard atmosphere data (to get proper mean heights). The vertical motion and divergence component of horizontal motion were then obtained from the quasi-geostrophic relationship. Grid spacing was 200 km and the time step was 3 min.

3. Filtered model systems

Both quasi-geostrophic and balanced equation systems were used diagnostically to define filtered reference data with the difference between those solutions and those from the primitive equation systems being interpreted as the gravity-inertial component.

a. Quasi-geostrophic (QG) Model

The horizontal velocity parameters were derived directly from the geopotential field of the primitive equation model using the geostrophic relationship $\mathbf{V}_g = f^{-1}\mathbf{k} \times \nabla\phi$ to compute the velocity $\mathbf{V}_g$ and an integrated form $\psi_g = f^{-1}\phi$ to determine the geostrophic streamfunction ψ_g. These velocity parameters were determined at 800 and 400 mb (the levels where horizontal velocity is defined in the primitive equation model) by linear interpolation from the levels where ϕ is defined.

Vertical motion, omega (ω), was derived from the quasi-geostrophic omega equation which defines the quasi-geostrophic vertical motion at 600 mb, i.e., ω_{QG2},

$$\left[\nabla^2 - \frac{2f^2}{\sigma_m(\Delta p)^2}\right]\omega_{QG2}$$
$$= \frac{f}{\sigma_m \Delta p}[J(\psi_{g1}, \nabla^2\psi_{g1}) - J(\psi_{g2}, \nabla^2\psi_{g2})]$$
$$- \frac{1}{g\sigma_m \Delta p}\nabla^2\left[J\left(\frac{\psi_{g1} + \psi_{g2}}{2}, \phi_1 - \phi_3\right)\right], \quad (8)$$

where ∇^2 is the Laplacian operator, J the Jacobian operator

$$\left[J(a, b) = \frac{\partial a}{\partial x}\frac{\partial b}{\partial y} - \frac{\partial a}{\partial y}\frac{\partial b}{\partial x}\right],$$

σ_m a constant static stability defined at 600 mb, and ψ_{gn} the geostrophic streamfunction at level n defined as $\tfrac{1}{2}f^{-1}(\phi_n + \phi_{n+1})$. Note that since the Coriolis parameter is constant, it does not appear in the vorticity advection terms. Vertical motion is non-zero at only one level so henceforth the subscript 2 is omitted. Thus $\omega_{QG2} = \omega_{QG}$.

b. Balanced (B) model

The equations for this two-layer model are a simplified subset of the general system described by Krishnamurti (1968). The pressure-velocity relationship is

$$\nabla^2\phi_B = f\nabla^2\psi_B + 2J(u_B, v_B), \quad (9)$$

where u_B and v_B are the balanced (and nondivergent) horizontal velocity components. Omega was set equal to zero at the upper and lower boundaries yielding

$$\left[\nabla^2 - \frac{2f^2}{\sigma_m(\Delta p)^2}\right]\omega_{B2} = \frac{f}{\sigma_m \Delta p}[J(\psi_{B1}, \nabla^2\psi_{B1}) - J(\psi_{B2}, \nabla^2\psi_{B2})]$$

$$- \frac{1}{4\sigma_m \Delta p}\nabla^2\{(\psi_{B1} + \psi_{B2}), (\phi_{B1} - \phi_{B3})\} - \frac{2}{\sigma_m \Delta p}\frac{\partial}{\partial t}[J(u_{B1}, v_{B1}) - J(u_{B2}, v_{B2})]$$

$$- \frac{f'}{\sigma_m \Delta p}[\nabla^2\psi_{B1}\nabla^2\chi_{B1} - \nabla^2\psi_{B2}\nabla^2\chi_{B2}] - \frac{f}{\sigma_m \Delta p}[\nabla\chi_{B1}\cdot\nabla(\nabla^2\psi_{B1}) - \nabla\chi_{B2}\cdot\nabla(\nabla^2\psi_{B2})], \quad (10)$$

where

$$\nabla^2\chi_{B1} = -\frac{\omega_{B2}}{\Delta p}, \quad u_B = -\frac{\partial\psi_B}{\partial y}$$

$$\nabla^2\chi_{B2} = \frac{\omega_{B2}}{\Delta p}, \quad v_B = +\frac{\partial\psi_B}{\partial x}$$

with χ being the velocity potential for horizontal motions, and where time derivatives were obtained using the vorticity equation which has a general form

$$\nabla^2\frac{\partial\psi_B}{\partial t} = -J(\psi_B, \nabla^2\psi_B) + \nabla\chi_B\cdot\nabla(\nabla^2\psi_B)$$

$$+ (\nabla^2\psi_B + f)\nabla^2\chi_B - \nabla\omega_B\cdot\nabla\frac{\partial\psi_B}{\partial p}$$

$$- \omega_B\frac{\partial}{\partial p}\nabla^2\psi_B. \quad (11)$$

Subscript B refers to variables satisfying the balance relationship. Since omega is nonzero at only one level, the subscript 2 is henceforth omitted. Thus $\omega_{B2} = \omega_B$. This system had to be solved by iterative techniques with either ψ_B or ϕ_B specified.

4. Diagnostic analysis methods

Even for this simple two-layered model situation, there were numerous physical variables that could be examined diagnostically. Many of these parameters were studied to see their relative merits for identifying the gravity-inertial mode component.

The diagnostic balanced model relationships were used to specify balanced velocity and pressure fields for comparison with the unfiltered primitive equation model solutions. To arrive at the balanced pressure field, the primitive equation and balanced streamfunctions were set equal enabling calculation of the geopotential via the balance equation. To arrive at the balanced velocity field, the primitive equation and balanced geopotential fields were set equal enabling calculation of the streamfunction via the balance equation.

Parameters are summarized in this section with subscript notation defined as follows:

p	primitive equation model
g	geostrophic
ag	ageostrophic
B	balanced model
QG	Quasi-geostrophic diagnostic model
NB	nonbalanced model component
χ	divergent component
ψ	nondivergent component

The following five horizontal motion and mass field functions were used:

1) Ageostrophic streamfunction ψ_{ag} defined by

$\psi_p - \psi_g$ where ψ_p was determined from V_p using $\nabla^2\psi_p = \mathbf{k}\cdot\nabla\times V_p$ with constant values for ψ_p at the northern and southern boundaries.

2) Ageostrophic velocity V_{ag} defined by $V_p - V_g$, where V_p comes directly from grid-point values. The computational method was designed to assure that the values of V_{ag} agreed with those determined from $V_{ag} = \mathbf{k}\times\nabla\psi_{ag}$.

3) Nonbalanced streamfunction ψ_{NB} defined by $\psi_p - \psi_B(\phi_p)$, where ψ_p was determined as discussed above and $\psi_B(\phi_p)$ was computed from ϕ_p using the Monge Ampere form of Eq. (9) setting $\phi_B = \phi_p$ and using the same boundary conditions employed to derive ψ_p. In regions where the equation became nonelliptic, geostrophic instead of balanced velocities were used in the Jacobian term.

4) Nonbalanced geopotential ϕ_{NB} defined by $\phi_p - \phi_B(\psi_p)$, where ϕ_p came directly from grid-point values and $\phi_B(\psi_p)$ was determined from ψ_p using a Poisson form of Eq. (9) specifying $\psi_B = \psi_p$ with constant values of ϕ_B at the northern and southern boundaries set to be compatible to the boundary values used for ψ_B.

5) Divergent velocity component V_χ defined from ω_p using $\nabla^2\chi = \partial\omega_p/\partial p$ with the normal derivative of χ set equal to zero at the northern and southern boundaries, and then using $V_\chi = -\nabla\chi$. The value of V_χ computed in this manner was essentially equal to $V_p - V_{\psi_p}$ where $V_{\psi_p} = \mathbf{k}\times\nabla\psi_p$.

The following four vertical motion fields were used defined only at the mid-level (600 mb):

1) Primitive equation model vertical motion ω_p taken directly from grid point values at 600 mb.

2) Quasi-geostrophic diagnostic model vertical motion ω_{QG} obtained from Eq. (8) assuming ω to be zero at the northern and southern boundaries.

3) Balanced vertical motion determined from the mass field $\omega_B(\psi_B, \phi_p)$, obtained by setting $\phi_B = \phi_p$ in Eqs. (9)–(11) and assuming ω to be zero at the northern and southern boundaries.

4) Balanced vertical motion determined from the velocity field $\omega_B(\psi_p, \phi_B)$, obtained by setting $\psi_B = \psi_p$ in Eqs. (9)–(11) and assuming ω to be zero at the northern and southern boundaries.

5. Case study

The basic data for the analysis were generated by a 24 h forecast with the primitive equation model. The initial state was an axially symmetric jet flow structure with vertical shear in the center of the channel (see Fig. 2). The half-width of the jet structure was 500 km. Maximum velocity was 26 and 9 m s^{-1} in the upper and lower layers respectively, giving a Rossby number that ranged as high as 0.26.
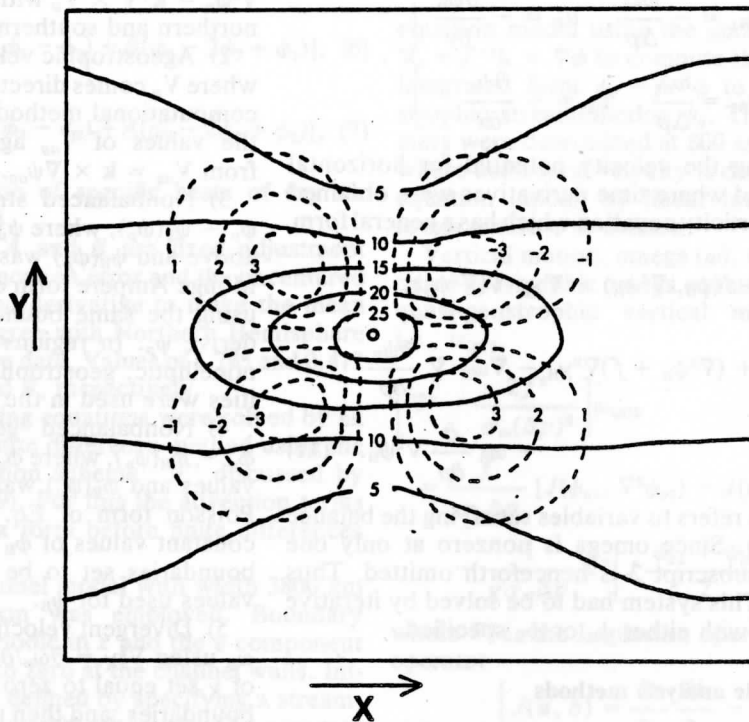
FIG. 2. The initial conditions for the u component magnitudes (m s^{-1}) at 400 mb (solid lines) and the vertical motion ω_2 (10^{-2} N m^{-2} s^{-1}) at 600 mb (dashed lines). The small circle at the isotach pattern center marks the initial position of the jet maximum.

For the specified average stability parameters and layer thicknesses the linear gravity wave speeds with no rotation or advection effects were 260 and 35 m s^{-1} for the external and internal modes respectively. Assuming the internal mode to be the fundamental one for the ageostrophic motions, the Rossby radius of deformation is 350 km which compares closely to the half-width of

FIG. 3. Vertical motion at 600 mb after 21 h computed by the diagnostic quasi-geostrophic model ω_{QG} (10^{-2} N m^{-2} s^{-1}). The cross in this and in all remaining figures (except Fig. 14) shows the jet maximum position.

the jet implying that adjustment processes are affected both by initial velocity and pressure field imbalance characteristics. The magnitude of the Rossby number suggests that non-quasi-geostrophic motions developed will be noticeable but still not dominate the solution.

During the integration the jet core propagated down the channel at a speed of ~14 m s^{-1} and after 24 h it had traversed nearly one-third the length of zonal periodicity. It held a relatively steady shape and amplitude reflecting the stable nature of the initially prescribed baroclinic field. The gross features of the four-cell vertical motion pattern were preserved although they were modified due to the presence of the non-quasi-geostrophic gravity-inertial wave component that was generated by the initial conditions and which subsequently propagated relative to the jet core. Fig. 3 shows the basic configuration for large-scale vertical motion near the end of the period provided by the diagnostic quasi-geostrophic model.
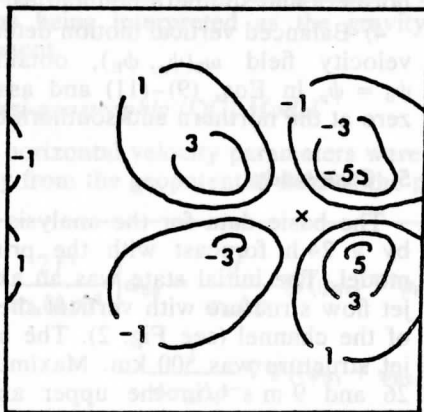
6. Discussion of Results

a. Horizontal motion parameters

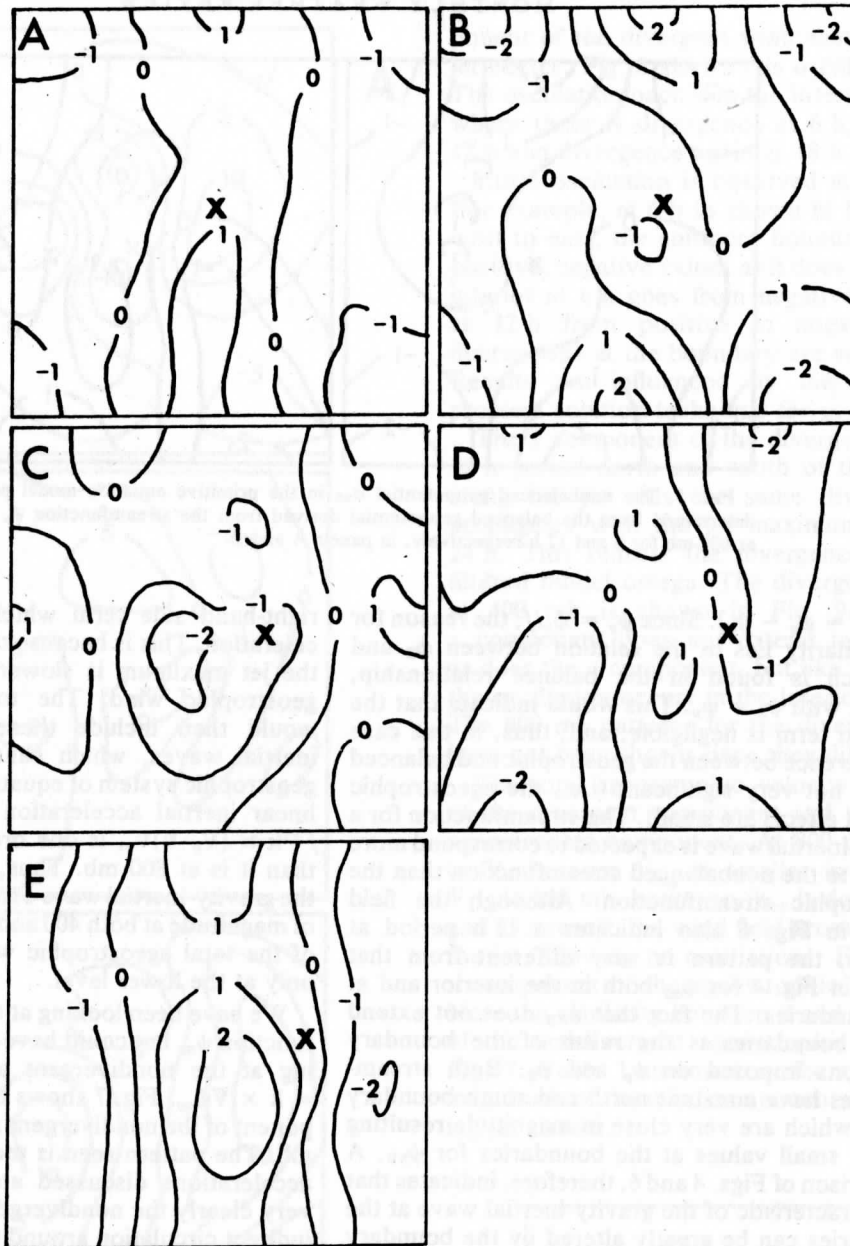The 800 mb ageostrophic streamfunction shows a 12 h period oscillation as shown in Fig. 4. Note

FIG. 4. Ageostrophic streamfunction ψ_{ag} (10^5 m² s⁻¹) at 800 mb for 3, 6, 9, 12 and 15 h
(panels A, B, C, D and E, respectively) in the primitive equation model results.

the similar structure at 3 h and at 15 h. The wave is seen to fill the entire domain, extending all the way to the boundaries. Since the boundary condition on ψ_p is constant, the boundary oscillations observed in Fig. 4 are due to the boundary values of ϕ_p which were allowed to vary in the p model from which the height data were generated. The dominant scale is the fundamental wavelength in both the x and y directions, ~4000 km in both directions. There appears to be two waves present, one propagating to the east and the other to the west.

These waves travel 4000 km in 12 h giving a propagation speed of ~93 m s⁻¹. Comparison with the eigenvalues for an equivalent linearized two-layer model without mean flow identifies these motions as internal gravity-inertial waves.

It is interesting to note the similarity between the ageostrophic streamfunction and the nonbalanced geopotential field at 800 mb (cf Figs. 4 and 5). The similarity in patterns implies that the ageostrophic streamfunction is very nearly equal to the nonbalanced geopotential field divided by f [i.e., (ϕ_B

FIG. 5. The nonbalanced geopotential ϕ_{NB} in the primitive equation model prediction determined from the balanced geopotential derived from the streamfunction ψ_p (10^{-1} m) at 800 mb for 6 and 12 h respectively, in panels A and B.

$- \phi_p)/f \approx \psi_p - \psi_g]$. Since $\psi_g = \phi_p/f$, the reason for the similarity lies in the relation between ϕ_B and ψ_p which is found in the balance relationship, Eq. (9), with $\psi_B = \psi_p$. This would indicate that the Jacobian term is negligible; and, thus, in this case the difference between the geostrophic and balanced wind is not very significant (i.e., the ageostrophic gradient effects are small). The streamfunction for a gravity-inertial wave is expected to correspond more closely to the nonbalanced streamfunction than the ageostrophic streamfunction. Although the field shown in Fig. 6 also indicates a 12 h period at 800 mb, the pattern is very different from that shown in Fig. 4 for ψ_{ag} both in the interior and at the boundaries. The fact that ψ_{NB} does not extend to the boundaries is the result of the boundary conditions imposed on ψ_p and ψ_B. Both streamfunctions have constant north and south boundary values which are very close in magnitude resulting in very small values at the boundaries for ψ_{NB}. A comparison of Figs. 4 and 6, therefore, indicates that the characteristic of the gravity-inertial wave at the boundaries can be greatly altered by the boundary conditions that are imposed on the streamfunctions from which the gravity-inertial wave streamfunction is derived.

At 400 mb the patterns derived from the streamfunction and height fields are also similar. However, they do not display any kind of oscillation but instead propagate along with the jet maximum. The reason for this lack of oscillation can be found in the definition of the ageostrophic wind in quasi-geostrophic theory:

$$\mathbf{V}_{ag} = f^{-1}\mathbf{k} \times \frac{\partial \mathbf{V}_g}{\partial t} + f^{-1}\mathbf{k} \times (\mathbf{V}_g \cdot \nabla)\mathbf{V}_g. \quad (13)$$

The first right-hand side term is the isallobaric wind which at 400 mb is smaller than the second

right-hand side term which is the advective acceleration. This is because the propagation speed of the jet maximum is slower than the speed of the geostrophic wind. The total ageostrophic wind would then include these effects plus gravity-inertial waves, which cannot exist in the quasi-geostrophic system of equations. At 400 mb the non-linear inertial acceleration effect from the term, $f^{-1}\mathbf{k} \times (\mathbf{V}_g \cdot \nabla)\mathbf{V}_g$, is one order of magnitude larger than it is at 800 mb. Thus, since the amplitude of the gravity-inertial wave oscillation is the same order of magnitude at both 400 and 800 mb, this component of the total ageostrophic wind is easily detectable only at the lower level.

We have been looking at the ageostrophic streamfunction ψ_{ag} but could have just as easily been looking at the nondivergent ageostrophic wind, $\mathbf{V}_{\psi_{ag}} = \mathbf{k} \times \nabla \psi_{ag}$. Fig. 7 shows the pattern of the v component of the nondivergent ageostrophic wind at 400 mb. The pattern seen is the result of the advective accelerations discussed above. The figure shows very clearly the nondivergent part of the direct and indirect circulation around the entrance and exit regions, respectively, of a jet core in the westerlies associated with large-scale evolution processes.

The divergent component of the wind exhibits further evidence of a 12 h period. The divergent wind component for a gravity-inertial wave should be equivalent to the divergent component of the total wind, $\mathbf{V}_x$, minus the divergent component related to the filtered model. The filtered model vertical motion field will be discussed later, but suffice it to say at this point that the vertical motion pattern propagates along steadily with the jet. Thus, the contribution to the total divergent wind is steady, which indicates that any oscillation observed in $\mathbf{V}_x$ must be due to gravity-inertial motions.
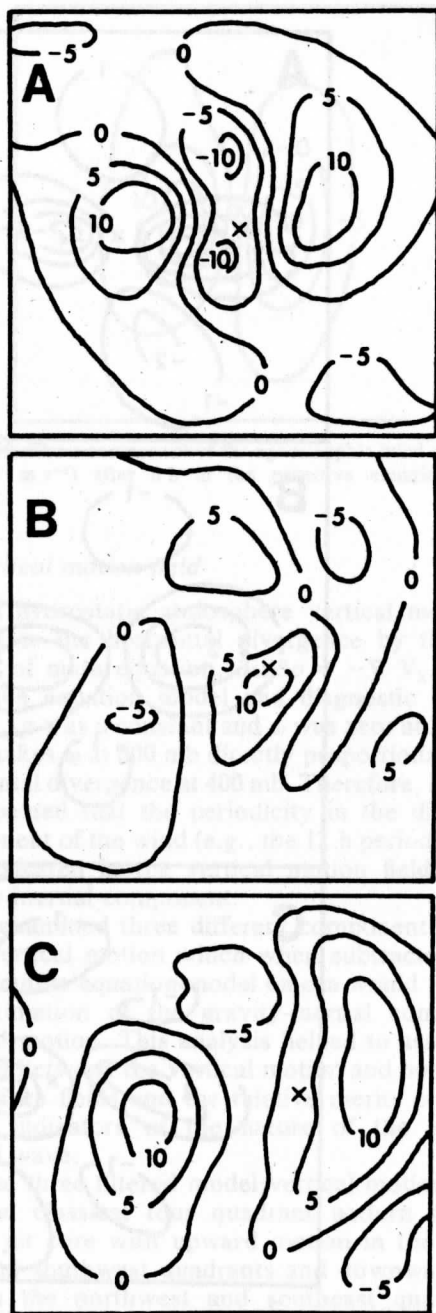
FIG. 6. The nonbalanced streamfunction ψ_{NB} (10^4 m^2 s^{-1}) at 800 mb at 6, 12 and 18 h in panels A, B, and C, respectively.

Unlike what we found with the ageostrophic streamfunction, the oscillations in the divergent component of the wind are observed not only at 800 mb but also at 400 mb. The behavior of the divergent patterns at the two levels is similar except that they are nearly 180° out of phase with each other which is consistent with Dynes' compensation. The 12 h oscillation can be seen in the *u* com-

ponent of the divergent wind east and west of the jet center. Fig. 8 shows this oscillation at 400 mb. The oscillation occurs in the interior of the domain where there is divergence at 6 h, convergence at 12 h and divergence again at 18 h.

Little oscillation is observed at the boundaries. For example, at 6 h as shown in Fig. 8 going from west to east, the southern boundary has negative, positive, negative values as it does at 12 h, while the interior at 6 h goes from negative to positive and at 12 h from positive to negative. Thus, the fluctuations at the boundary are strongly inhibited. Results are influenced by the boundary value problem solution technique for χ.

The *v* component of the divergent wind shows a 12 h period north and south of the jet; however, along the jet axis the same divergence pattern propagates with the jet maximum throughout all 24 h. This reflects the divergence related to the filtered model omega. The divergent *v* component at 400 mb is shown in Fig. 9. The divergent *v* component does not extend to the boundaries as does the *u* component, but like the *u* component the oscillation occurs in the interior of the domain. The 800 mb patterns for the divergent wind fields have not been shown since they differ only in sign.

The total ageostrophic velocity is just the sum of the divergent component and the nondivergent ageostrophic component. At 800 mb V_{ag} is similar to V_{χ} because $V_{\psi_{ag}}$ is smaller in magnitude than V_{χ}. At 400 mb, however, V_{ag} is dominated by $V_{\psi_{ag}}$, and as a result, the wind field propagates along with the jet, showing no oscillations. Fig. 10 shows the *v* component of the ageostrophic wind at 400 mb. Note the similarity between it and the *v* component of the nondivergent ageostrophic wind shown in Fig. 7. Table 1 summarizes the typical maximum magnitude of the wind components in this propagating jet stream.
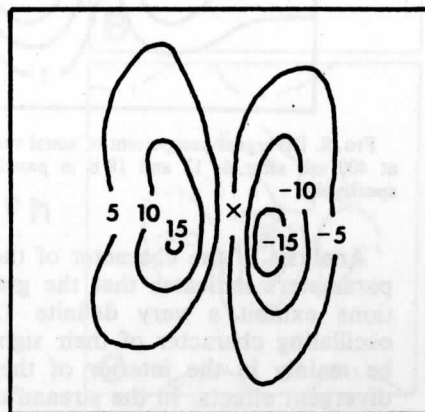

FIG. 7. The nondivergent ageostrophic *v* component of velocity $v_{\psi_{ag}}$ (10^{-1} m s^{-1}) in the primitive equation results after 6 h at 400 mb.
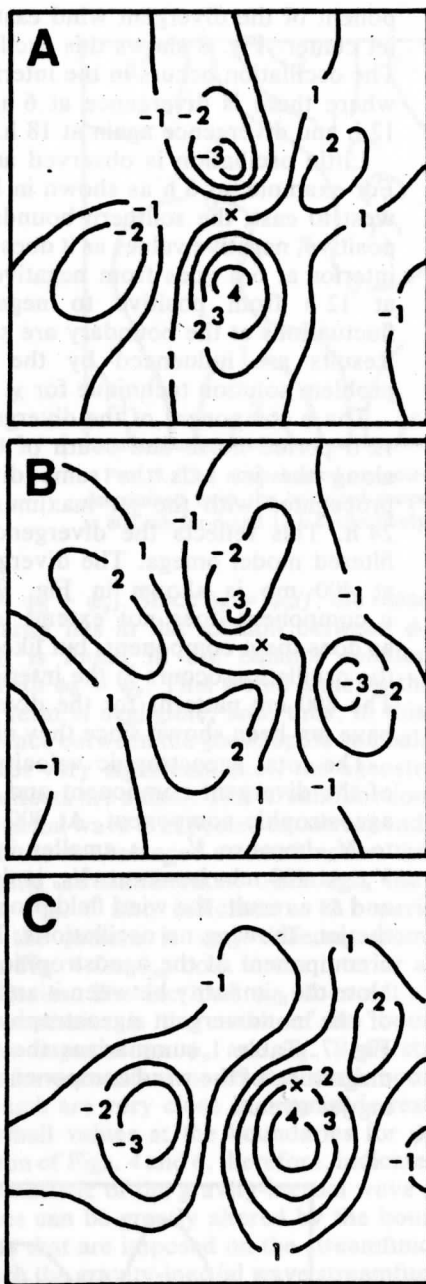
FIG. 8. Divergent component of zonal velocity u_x (10^{-1} m s^{-1}) at 400 mb after 6, 12 and 18 h in panels A, B, and C, respectively.
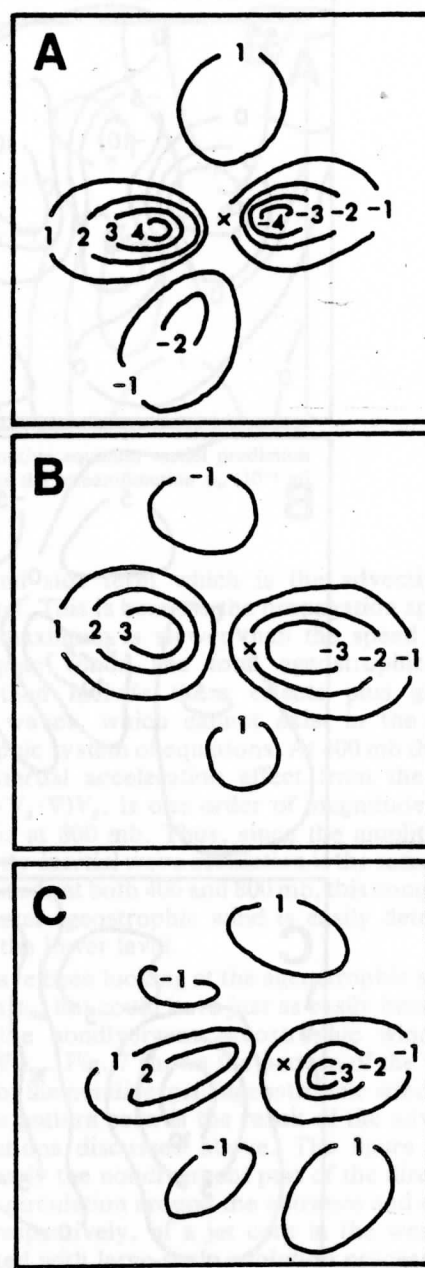
FIG. 9. Divergent component of the meridional velocity v_x (10^{-1} m s^{-1}) at 400 mb after 3, 9, and 15 h in panels A, B and C, respectively.

Analysis of the character of the horizontal flow parameters indicates that the gravity-inertial motions exhibit a very definite 12 h period. The oscillating character of their signature appears to be mainly in the interior of the domain for the divergent effects. In the streamfunction field, both the ψ_{ag} and ψ_{NB} patterns show an interior oscillation, while the ψ_{ag} oscillation also extends to the

boundaries. It was not clear whether the boundary oscillation in the streamfunction ψ_{ag} was part of the gravity-inertial wave signature or whether it was the result of the imposed boundary conditions. However, the coherency in the period and in the shape of the patterns as shown in Fig. 4 would tend to indicate that the gravity-inertial wave did extend to the boundary.
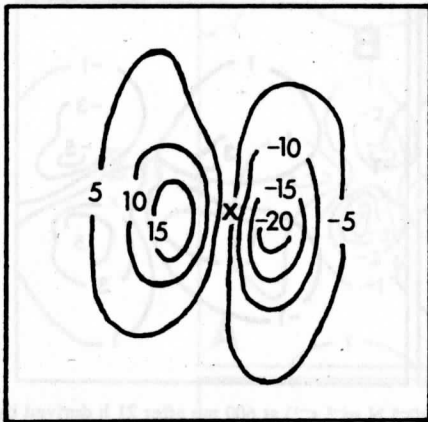
FIG. 10. The v component of the ageostrophic wind at 400 mb v_{ag} (10^{-1} m s^{-1}) after 6 h in the primitive equation model forecast.

b. Vertical motion field

In a hydrostatic atmosphere vertical motion is related to the horizontal divergence by the continuity of mass equation, $\partial\omega/\partial p = -\nabla \cdot \mathbf{V}_\chi$. In the primitive equation model and diagnostic balance model Δp was a constant and ω was zero at 200 mb. This makes ω at 600 mb directly proportional to the horizontal divergence at 400 mb. Therefore, it would be expected that the periodicity in the divergent component of the wind (e.g., the 12 h period) would be duplicated in the vertical motion field of the gravity-inertial component.

We examined three different components of the total vertical motion which when subtracted from the primitive equation model omega would yield an approximation of the gravity-inertial component vertical motion. This analysis helped to assess the relation between the vertical motion and horizontal divergence fields and the relative merits of ω and $\mathbf{V}_\chi$ as indicators of the nature of the gravity-inertial wave.

These three filtered model vertical motion fields had the classical four quadrant pattern relative to the jet core with upward motion in the northeast and southwest quadrants and downward motion in the northwest and southeast quadrants. The basic pattern persisted throughout the 24 h period. In all three cases the differences between these fields and the primitive equation vertical motion fields showed a basic oscillation with a half-period of 6 h which was not discernible after 9 h.

The diagnostic quasi-geostrophic omega ω_{QG} field began with equal magnitudes in all four quadrants and then the vertical motions in both the northeast and northwest quadrants intensified while the two quadrants south of the jet decreased in magnitude. After about 6 h the downward motion in the southeast quadrant began to intensify so that toward the

TABLE 1. Typical maximum magnitudes (m s^{-1}) in the jet stream system for horizontal velocity components.

	u_p	$u_{\psi_{ag}}$	u_χ	u_{ag}	v_p	$v_{\psi_{ag}}$	v_χ	v_{ag}
800 mb	8.8	0.26	0.34	0.44	1.7	0.39	0.36	0.51
400 mb	26.0	0.70	0.36	0.76	4.4	1.21	0.41	1.40

later times the strongest downward motion was to the right of the jet. Fig. 3 shows ω_{QG} at 21 h. When ω_{QG} is subtracted from ω_p, the pattern shown in Fig. 11 results. The oscillation of the primitive equation omega about the quasi-geostrophic omega has a 6 h half-period. This oscillation is not observable after 9 h.

The diagnostic balance model omega, $\omega_B(\psi_p, \phi_B)$, began with stronger vertical motions to the north of the jet. However, after 12 h the strongest downward
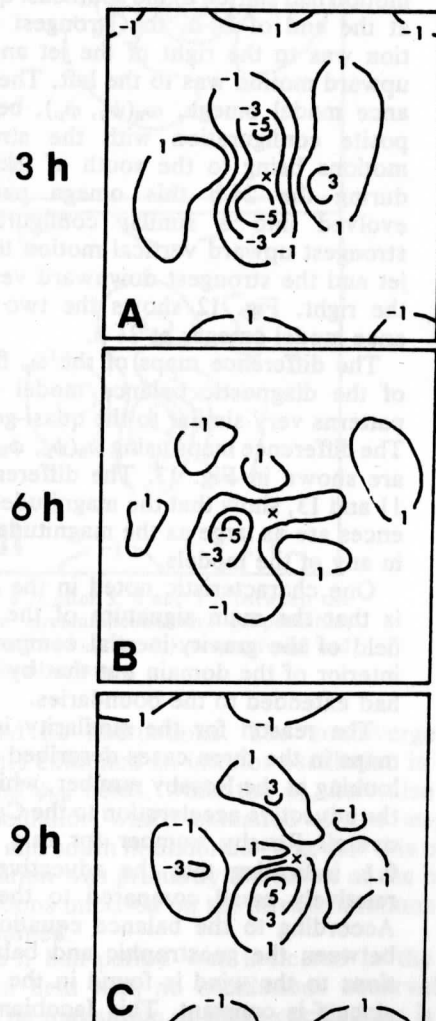

FIG. 11. Difference in 600 mb omega (10^{-2} N m^{-2} s^{-1}) after 3, 6 and 9 h between the primitive equation model values and the diagnostic quasi-geostrophic model.
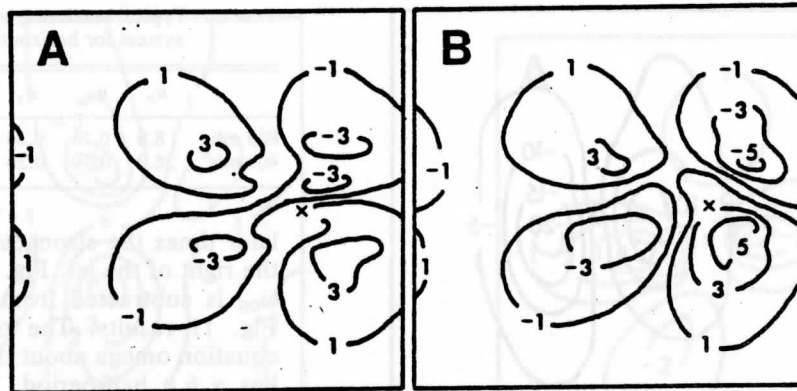
FIG. 12. Balanced model vertical motion (10^{-2} N m^{-2} s^{-1}) at 600 mb after 21 h derived by matching the streamfunction and geopotential in turn to the primitive equation values [$\omega_B(\psi_p, \phi_B)$ and $\omega_B(\psi_B, \phi_p)$, respectively] in panels A and B.

motion had shifted to the southeast quadrant, so that at the end of 24 h, the strongest downward motion was to the right of the jet and the strongest upward motion was to the left. The diagnostic balance model omega, $\omega_B(\psi_B, \phi_p)$, began in the opposite configuration with the strongest vertical motions being to the south of the jet. However, during the 24 h this omega pattern gradually evolved into a similar configuration with the strongest upward vertical motion to the left of the jet and the strongest downward vertical motion to the right. Fig. 12 shows the two diagnostic balance model omegas at 21 h.

The difference maps of the ω_p field minus each of the diagnostic balance model omegas yielded patterns very similar to the quasi-geostrophic case. The difference maps using $\omega_B(\psi_p, \phi_B)$ and $\omega_B(\psi_B, \phi_p)$ are shown in Fig. 13. The difference maps, Figs. 11 and 13, show that the magnitudes of the ω differences are as large as the magnitudes of the omegas in any of the models.

One characteristic noted in the difference fields is that the main signature of the vertical motion field of the gravity-inertial component was in the interior of the domain but that by 15 h the pattern had extended to the boundaries.

The reason for the similarity in the difference maps in the three cases described can be found by looking at the Rossby number, which is the ratio of the advective acceleration to the Coriolis force. The overall Rossby number for this experiment was 0.1, indicating that the advective acceleration is relatively small compared to the Coriolis force. According to the balance equation the difference between the geostrophic and balance approximations to the wind is found in the term $2J(u_B, v_B)$, since f is constant. This Jacobian term comes directly from the fact that the advective acceleration terms are retained in the development of the bal-

ance equation. Thus, with the advective acceleration relatively small, the Jacobian term is small; and the difference between the geostrophic and balance approximations is minimized. This was substantiated earlier in the comparison of the ageostrophic streamfunction with the nonbalanced geopotential field.

In a localized area around the jet maximum, however, the Rossby number is quite a bit larger because the advective accelerations are large. In this localized area one would expect to see the greatest difference between the geostrophic and balance approximations, and it is in this area that the omega fields show the greatest difference. By comparing Figs. 13 and 11 in the vicinity of the jet maximum, one can see that even though the overall patterns are very similar, a difference does occur in the region of the jet maximum.

Mudrick (1974) noted the tendency for stronger downward vertical motion to the right of the jet. The fact that this result is observed in the quasi-geostrophic and balance model omega fields as well as the primitive equation omega fields (see Fig. 14) indicates that it is at least partly a result of the effects of the gradient flow and not a result of the presence of the gravity-inertial component.

Because the omega patterns and resulting difference maps of both the diagnostic balance model cases are so similar, it is not possible to accurately assess which of the two approaches to the solution of the balance model omega provided a better means of obtaining the vertical motion field of the gravity-inertial component. The usefulness of the analysis technique of subtracting the balance model omega from the primitive equation model omega to obtain the vertical motion field of the gravity-inertial wave appears to lie mainly in showing the presence of the gravity-inertial wave rather than enabling a clearer understanding of whether the
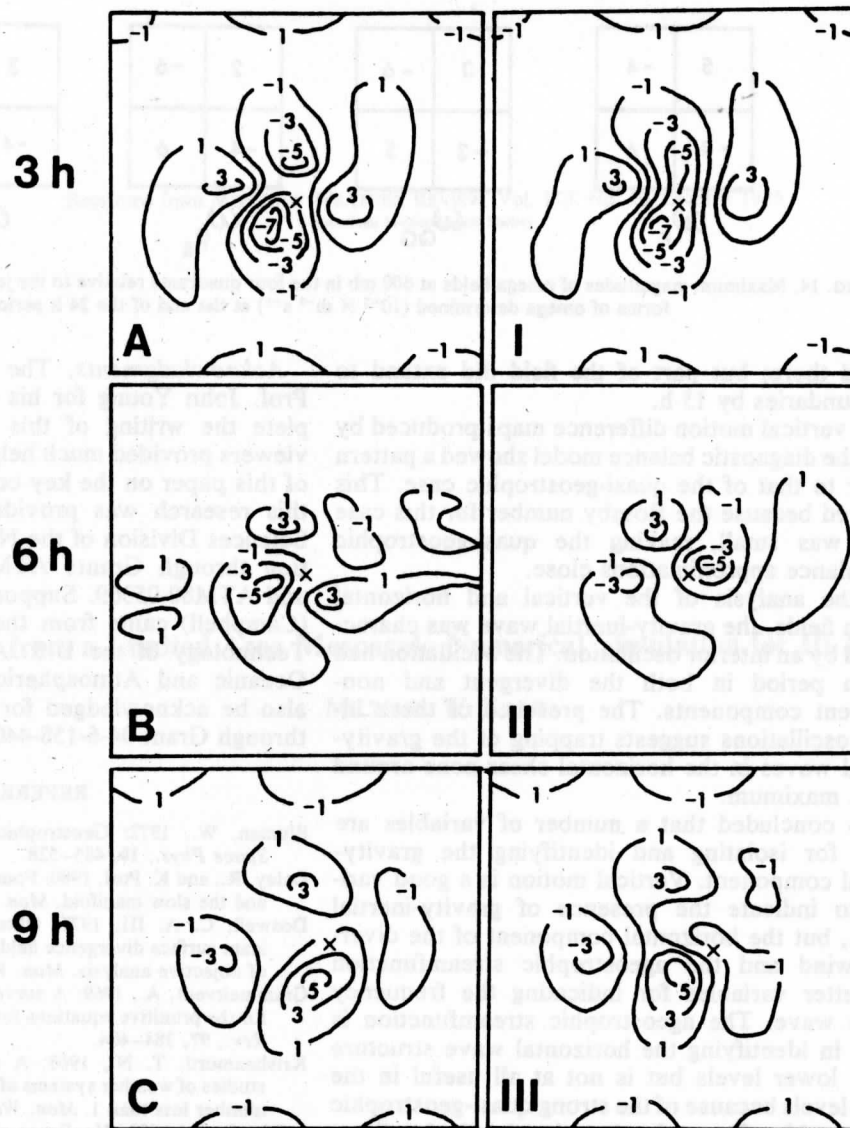
FIG. 13. Difference in 600 mb omega (10^{-2} N m^{-2} s^{-1}) after 3, 6 and 9 h between the balanced model omegas derived by matching the streamfunction and geopotential, respectively, to the primitive equation values [$\omega_B(\psi_p, \phi_B)$ and $\omega_B(\psi_B, \phi_p)$, respectively] and the primitive equation omega ω_p in the left and right-hand columns.

pressure or wind field is adjusting. We reached the same conclusion using the difference maps produced by the quasi-geostrophic model omega.

7. Summary and conclusions

Both the divergent and nondivergent components exhibited a structure on the scale of the jet maximum with a definite 12 h period. The structure had a propagation speed and period consistent for an internal gravity-inertial wave. The divergent u and v components of the wind showed an oscillation in the interior of the domain only, for their magnitudes at the boundaries were small and

showed no fluctuations. The nondivergent components exhibited an interior oscillation in both the ψ_{ag} and ψ_{NB} fields, while the ψ_{ag} field also showed an oscillation which extended all the way to the north and south boundaries. Whether this boundary oscillation was primarily the result of the boundary conditions imposed on the streamfunctions was not determined.

A 6 h half-period was indicated in the vertical motion field with no oscillations observable after 9 h. The magnitude of these oscillations is as large as the magnitude of the primitive equation omega itself. The vertical motion field began in the interior of the domain and the largest magnitudes re-
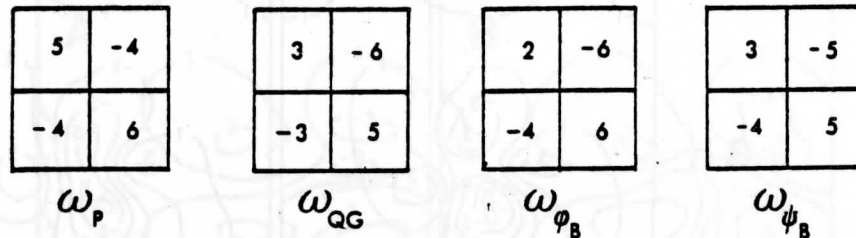
FIG. 14. Maximum magnitudes of omega fields at 600 mb in the four quadrants relative to the jet maximum for the four forms of omega determined (10^{-2} N m^{-2} s^{-1}) at the end of the 24 h period.

mained there; but part of the field did extend to the boundaries by 15 h.

The vertical motion difference maps produced by using the diagnostic balance model showed a pattern similar to that of the quasi-geostrophic case. This occurred because the Rossby number for this case study was small, making the quasi-geostrophic and balance approximations close.

In the analysis of the vertical and horizontal motion fields, the gravity-inertial wave was characterized by an interior oscillation. The oscillation had a 12 h period in both the divergent and nondivergent components. The presence of these interior oscillations suggests trapping of the gravity-inertial waves in the horizontal shear zone around the jet maximum.

It is concluded that a number of variables are useful for isolating and identifying the gravity-inertial component. Vertical motion is a good variable to indicate the presence of gravity-inertial waves, but the horizontal component of the divergent wind and the ageostrophic streamfunction are better variables for indicating the frequency of the wave. The ageostrophic streamfunction is useful in identifying the horizontal wave structure in the lower levels but is not at all useful in the upper levels because of the strong quasi-geostrophic ageostrophic effects. On the other hand, the divergent component of the wind can be used at both levels to observe the periodicity of the gravity-inertial waves.

It is clear that the gravity-inertial motions found here could not have been identified by a simple separation of horizontal scales. It would be of great interest to determine how well time filtering or normal mode techniques would isolate the gravity-inertial component.

REFERENCES

Blumen, W., 1972: Geostrophic adjustment. *Rev. Geophys. Space Phys.*, 10, 485–528.
Daley, R., and K. Puri, 1980: Four-dimensional data assimilation and the slow manifold. *Mon. Wea. Rev.*, 108, 85–99.
Doswell, C. A. III, 1977: Obtaining meteorologically significant surface divergence fields through the filtering property of objective analysis. *Mon. Wea. Rev.*, 105, 885–892.
Grammeltvedt, A., 1969: A survey of finite-difference schemes for the primitive equations for a barotropic fluid. *Mon. Wea. Rev.*, 97, 384–404.
Krishnamurti, T. N., 1968: A diagnostic balance model for studies of weather systems of low and high latitudes, Rossby number less than 1. *Mon. Wea. Rev.*, 96, 197–208.
Leith, C. E., 1980: Nonlinear normal mode initialization and quasi-geostrophic theory. *J. Atmos. Sci.*, 37, 958–968.
Maddox, R. A., 1980: An objective technique for separating macroscale and mesoscale features in meteorological data. *Mon. Wea. Rev.*, 108, 1108–1121.
Mudrick, S. E., 1974: A numerical study of frontogenesis. *J. Atmos. Sci.*, 31, 869–891.
Obukhov, A., 1949: On the question of the geostrophic wind. *Izv. Akad. Nauk SSSR Geofiz. Geogr.*, 13, 281–306.
Okland, H., 1970: On the adjustment toward balance in primitive equation weather prediction models. *Mon. Wea. Rev.*, 98, 271–279.

Results from a Limited Area Mesoscale Numerical Simulation for 10 April 1979

MICHAEL W. KALB

Results from a Limited Area Mesoscale Numerical Simulation for 10 April 1979

MICHAEL W. KALB*

Universities Space Research Association, Atmospheric Sciences Division, Marshall Space Flight Center, Huntsville, AL 35812

ABSTRACT

Results are presented from a nine-hour limited area fine mesh (35 km) mesoscale model simulation initialized with SESAME-AVE I radiosonde data for 10 April 1979 at 2100 GMT. Emphasis is on the diagnosis of mesoscale structure in the mass and precipitation fields.

The model simulated most of the life cycle of a propagating mesoscale short wave/precipitation band (≈ 250 km wide) which developed from a dry low-level (700 mb) mesoscale short wave trough in the initial state. The short wave, which was supported initially by balanced winds, was retained by the model, propagated around a synoptic scale trough from Oklahoma to Nebraska, while initiating and organizing precipitation into a mesoscale band along the trough axis. The short wave and precipitation propagated northward together at about 18 m s^{-1}. The onset of precipitation was accompanied by a decrease in width of the short wave. The system displayed distinctive vertical structure including downwind tilt with height. The short wave precipitation band verified well with a similar band evident in NMC hourly radar summaries in terms of location, rate of movement and spatial dimensions.

Along the Texas/Oklahoma border, independent of the short wave, convective precipitation formed several hours into the simulation and was organized into a narrow band suggestive of the observed 10 April squall line. The orientation and location of model convective precipitation were generally consistent with observed convective weather areas over Texas and Oklahoma.

The good results of model simulation are attributed to a combination of comprehensive model physics, fine grid resolution and subsynoptic scale initial data.

1. Introduction

In the last decade a class of three-dimensional primitive equation numerical prediction models have been developed which operate with grid spacings from 10 to 100 km (Perkey, 1976; McGregor *et al.*, 1978; Kaplan *et al.*, 1982; Anthes *et al.*, 1982; Ross and Orlanski, 1982). Such models are frequently referred to as mesoscale models because in principle they are capable of simulating atmospheric events occurring naturally on space scales down to about 50 km, consistent with the scales designated by Orlanski (1975) as meso-alpha (200–2000 km) and meso-beta (20–200 km). While lacking high spatial or temporal density meteorological observations, diagnostic studies of the internally consistent and quantitative view of the mesoscale atmosphere provided by high resolution models may represent the best hope for understanding mesoscale dynamics and mesosynoptic scale interactions. For example, recent studies have examined the role of diabatic processes in cyclone development based on mesoscale model output (Chang *et al.*, 1982; Robertson and Smith, 1983).

To an even greater extent than for larger scale models, mesoscale models are subject to limitations on forecast accuracy imposed by: a) numerical considerations such as boundary conditions and finite differencing accuracy, b) adequacy of parameterizations for subgrid scale physical processes and c) suitability of existing observational data for specifying a model initial state. While mesoscale models may differ in their handling of numerics and physical parameterizations (see Anthes, 1983), all are usually limited by initial data having characteristics attributable to the same conventional synoptic scale radiosonde network.

The question as to what would constitute better initial data for mesoscale models is not easily answered. One viewpoint is that a mesoscale model should be capable of generating many realistic mesoscale structures from an initial state carefully constructed from synoptic scale observations (Anthes *et al.*, 1981). One such structure might be a frontal zone resulting from a confluence of two synoptic scale flows. On the other hand, there is evidence that substantial positive impacts may result in mesoscale precipitation forecasts when high density initial moisture data are used that are capable of depicting detailed moisture gradient information (Perkey, 1980). The need for higher density temperature observations is more controversial since the importance of detail in an initial temperature field to the forecast of meteorological phenomena, according

---

* Previous affiliation: Department of Meteorology, University of Wisconsin–Madison, Madison, WI 53706.

to geostrophic adjustment theory, decreases as the scale of the phenomenon decreases. Smaller meteorologically important (but nongravity wave) solutions of a model atmosphere evolve mainly in response to the initial wind field without regard to fine structure in the initial temperature. However, the word "small" is relative and there is an intermediate scale range in the meso-alpha scales for middle latitudes where the wind versus mass (temperature) initialization problem is not well defined. In these scales initial wind and temperature structure may be equally important to a mesoscale forecast.

This study approaches the initial data issue directly by initializing the Drexel University-LAMPS (Limited Area Mesoscale Prediction System; Perkey, 1976) mesoscale model with subsynoptic scale radiosonde data from the SESAME AVE-I observing period of 10–11 April 1979. This SESAME data set has been used in mesoscale modeling studies by Anthes et al. (1982) and Kaplan et al. (1982). Those studies initialized at 1200 GMT 10 April over a much larger domain than is used here, and with the SESAME radiosonde data input to merely complement the conventional radiosonde network. In the Anthes study, a twenty-four hour simulation was performed on a 111 km grid and employed a parameterization for convective precipitation. The Kaplan study used a very fine mesh ($\approx$48 km); convective effects, however, were not included.

In this study, the SESAME-AVE radiosonde data are used to initialize over a limited area approximating the SESAME regional scale domain while employing a very fine grid mesh capable of resolving meso-alpha structure in the initial data and incorporating a convective parameterization. In further contrast to the other studies, the LAMPS model was initialized at 2100 GMT (rather than 1200 GMT) on 10 April when at least one well documented short wave was present in the SESAME network. Sections 2, 3 and 4 of this paper provide background on the model, synoptic situation of 10 April and data acquisition and analysis, respectively. Model results presented in Sections 5 and 6 will show that a combination of comprehensive model physics in the LAMPS model, fine grid resolution and subsynoptic scale initial data provide an excellent simulation of the observed mesoscale evolution of mass and precipitation fields for 10–11 April 1979. The last section consists of a summary and concluding remarks.

2. The model

LAMPS is a 15-level hydrostatic primitive equation model with options for different grid spacings and nesting of the finer resolution grids within the coarser. A terrain following sigma-height coordinate is used in the vertical with levels at 0, 0.025, 0.375, 0.750, 1.25, 2.0, 4.5, 6.0, 7.5, 9.0, 10.5, 12.0, 14.0 and 16.0 km.

The prognostic model variables are the wind components u and v, specific humidity q, potential temperature θ as well as rain water, cloud water, and the Exner function which is predicted at the model top and diagnosed hydrostatically at all lower levels. Vertical velocity is diagnosed from a model continuity equation subject to the constraint that it be zero at the model top and bottom.

Horizontal finite differencing is fourth order accurate. Time differencing is second order accurate leapfrog with a weak filter applied to avoid the inherent computational mode. A fourth order diffusion term applied to all prognostic equations eliminates smallscale features which can not be handled numerically. The diffusion coefficient is increased near the lateral boundaries. Lateral boundary conditions for the prognostic variables are normally linearly time varying (see Perkey and Kreitzberg, 1976).

Precipitation is partitioned into grid scale ("stable") and convective modes. Convective precipitation is parameterized by a one-dimensional plume model as described by Kreitzberg and Perkey (1976). The main features of the convective scheme are its ability to initiate convection at any level through release of layer potential instability and to fuel that convection with a supply of moisture from an arbitrary level. The LAMPS convective parameterization can also give realistic vertical profiles of convective latent heating based on vertical profiles of parameterized condensation and evaporation. This flexibility in the determination of diabatic heating profiles can have a significant effect on the development of modeled weather systems just from simple static stability considerations.

The planetary boundary layer is modeled with K-theory. Fluxes of mass, momentum and heat through the surface layer are handled with Monin–Obukhov similarity theory. Boundary layer height is specified as a simple function of time.

3. Synoptic weather events of 10–11 April 1979

The date of the Wichita Falls tornado outbreak which resulted in over 50 deaths and nearly 400 million dollars in property damage was 10 April 1979 (Moller, 1980). The synoptic scale events leading to conditions favorable for severe weather began with a north–south oriented upper-level trough centered over the western Rocky Mountains at 1200 GMT 10 April. The trough developed negative tilt as its axis rotated toward the Texas Panhandle during the following 12 hours (see Fig. 1). An upper-level jet streak propagated around the trough via Mexico, entering southwest Texas by 2100 GMT.

A 988 mb surface low in northcentral Colorado at 1200 GMT moved to the southeastern part of the state where it remained until 0900 GMT 11 April. However, a cold front extending southward from the low into Mexico entered from the west at 1800 GMT. As the front continued into central Texas during the next six hours, a warm front moving northward from the Gulf of Mexico to the Texas/Oklahoma border by 2100
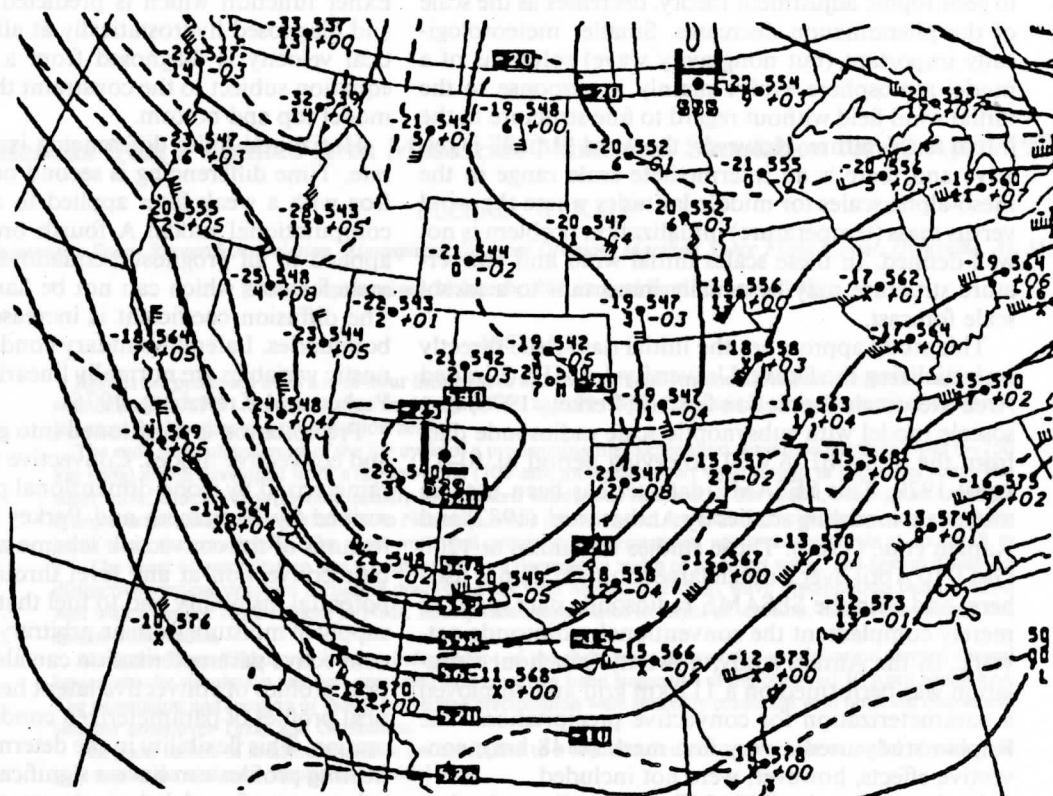
FIG. 1. 500 mb NMC height analysis for 0000 GMT 11 April 1979.

GMT provided most of Texas with an abundant supply of warm air and moisture at low levels. Southerly 850 mb winds pumped additional moisture into Oklahoma.

The first tornado occurred at 2100 GMT at Cornwell, Texas near the Texas/Oklahoma border to begin an outbreak in which at least one tornado was on the ground at any given time during the following five hours. A second outbreak in central Texas from 0300 to 0600 GMT 11 April was associated with a squall line which began to form around 0100 GMT (see Fig. 2). All tornadic activity subsided after 0600 GMT, but during the night general convective precipitation spread from Oklahoma into Missouri, Illinois, Iowa and Nebraska. The following day the surface low, just to the north of the Texas Panhandle, began to occlude producing widespread precipitation over much of the Midwest. A more detailed analysis of the synoptic events for this case can be found in Moore and Fuelberg (1981).

This modeling study focuses only on the period of most intense severe weather from 2100 to 0600 GMT 10–11 April.

4. Data analysis and initialization

As part of the SESAME-AVE I experiment, radiosondes with 250 km average station separation were

released every three hours from 1200 GMT 10 April to 1200 GMT 11 April 1979 over a regional scale domain (Barnes, 1981) similar to that shown in Fig. 3. At any one time, about 35–40 soundings were available that each reported geopotential heights, wind information, temperatures and dew points every 25 mb.

Only mandatory level data were used in this study. No vertical smoothing of the radiosonde profiles was performed and no attempt was made to compensate for downwind balloon drift. However, height corrections were required for several radiosondes to account for miscalibrated barometers. Radiosonde winds were not used in the study reported here; instead (and except for low-level winds), nondivergent winds were obtained at mandatory pressure levels using the nonlinear balance equation. In areas where the balance equation was nonelliptic, the winds were constrained to have zero absolute vorticity. This was considered preferable to insuring ellipticity by altering the height fields (as is frequently done) for reasons which will become clear momentarily.

The rationale for some of the procedures just described is best understood in the context that the SESAME data-based simulation constitutes the control for a larger set of experiments designed to explore the relative performances of high density satellite temperature data versus high density (SESAME-AVE) radiosonde
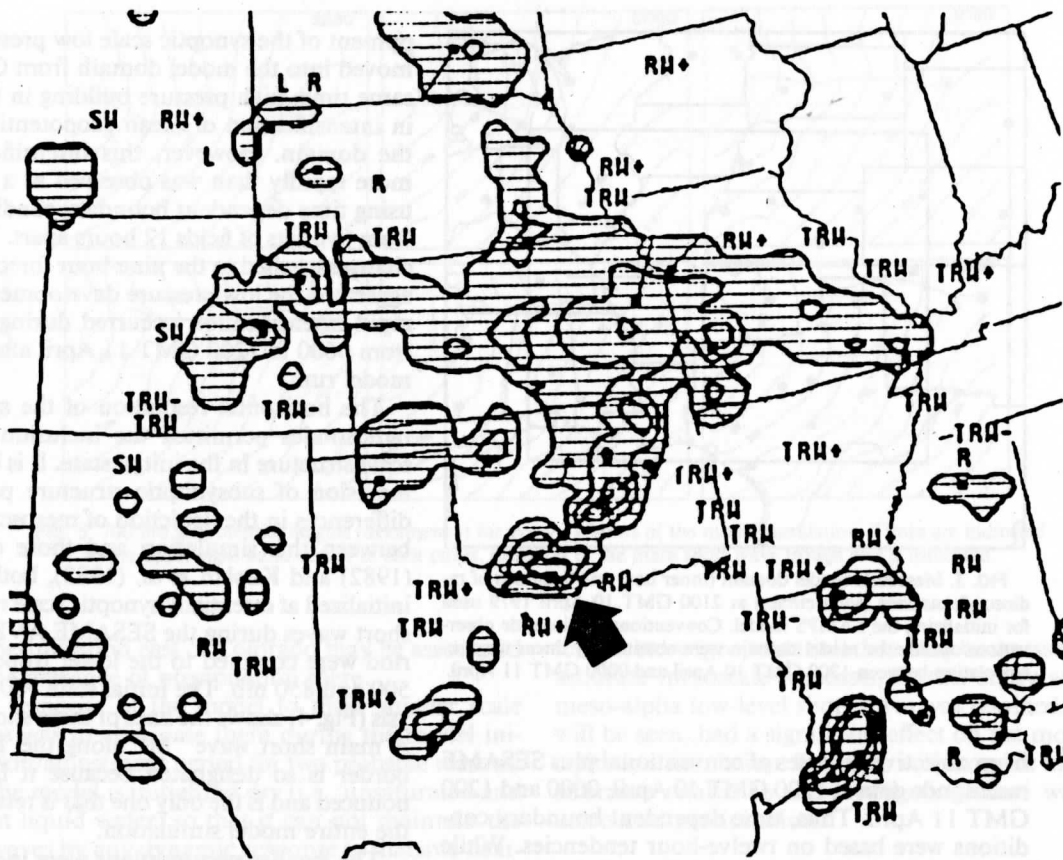
FIG. 2. NMC radar summary for 0135 GMT 11 April 1979. The large cell on the Texas/Oklahoma border indicated by the heavy arrow covers the area of the Wichita Falls tornado outbreak. Contours represent intensity levels 1, 3 and 5 corresponding to convective rainfall rates 0–28, 28–113 and 113+ mm h^{-1}, respectively.

temperature data in a mesoscale model. The use of mandatory level data was to give radiosonde-based observations the same vertical resolution as satellite temperature profiles, which is not a serious limitation since those levels are consistent with the vertical resolution of the LAMPS model above 850 mb. The balanced winds play the role of gravity wave noise control in the initialization and of ensuring that the initial wind fields depend only on temperature structure. This necessity to control the temperature-mass structure for the set of model experiments explains why geopotential heights were not modified to guarantee ellipticity of the balance equation.

Each radiosonde profile of u, v, T and q was linearly interpolated to the fifteen model "sigma-height" surfaces upon which a Barnes objective analysis (Barnes, 1973) was performed to transfer station point data to the horizontal model grid mesh.

A surface wind analysis based on hourly Service A network observations was used to construct a low-level divergent wind field influencing a layer up to model level 5 ($\approx$1250 m). The winds from model levels 6–15 were thus based on the balance equation, while

winds at levels 2–5 were obtained by linear interpolation of u and v components between the surface and level 6, resulting in an Ekman-like turning of the low-level winds with height.

If vertical motion is not zero at the model top initially, large amplitude external gravity waves can be excited which greatly modify the forecast mass fields. To insure initially small model top vertical velocities, a "wind adjustment" scheme similar to that of Washington and Baumhefner (1975) was employed to remove net vertically integrated mass divergence in all columns.

During this process, winds have their divergent components altered according to a preselected vertical weighting function. The initial divergent components in this case result from the specified low-level winds plus any small divergence induced during vertical interpolation of the balanced winds.

The initialization was entirely static. Noise level statistics (not shown here) indicated a period of about 1½ h for the model to achieve internal balance. Time dependent boundaries were not derived from a larger scale model run as is the usual procedure, but were computed
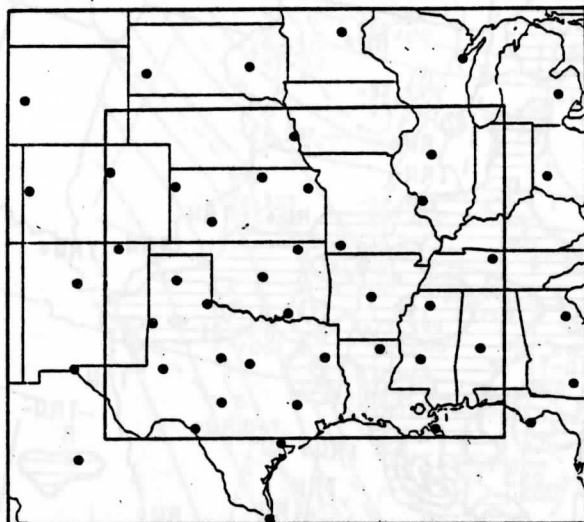
FIG. 3. Mesoscale model domain (inner box) and locations of radiosonde stations (solid circles) at 2100 GMT 10 April 1979 used for initializing the LAMPS model. Conventional radiosonde observations outside the model domain were obtained by linear time interpolation between 1200 GMT 10 April and 0000 GMT 11 April.

from objective analyses of conventional plus SESAME radiosonde data at 1200 GMT 10 April, 0000 and 1200 GMT 11 April. Thus, time dependent boundary conditions were based on twelve-hour tendencies. While boundary tendencies generated from three-hour SESAME radiosondes were possible, and would have been more consistent with the simulation of mesoscale processes, 12-hour tendencies were chosen to be consistent with those that might be obtained from LFM or global model forecast fields. Also, coarse time and space resolution for boundary tendencies were used to diminish arguments that for the small domain used here the results may be unduly influenced by the observed mesoscale boundary conditions relative to processes occurring on the interior of the mesoscale domain.

The geographical limits of the model domain were 105.0–86.13°W, 29.0–42.375°N. These boundaries plus a grid spacing of 0.3125 and 0.385° in the north–south and east–west directions, respectively, define a 44 by 50 grid with average 35 km resolution. The time step was 40 s for the entire nine-hour simulation from 2100 GMT 10 April to 0600 GMT 11 April.

5. Forecast mass fields

Geopotential height fields for the model forecast show the development of both large-scale (domain size or larger) and mesoscale features. The model provided a reasonable simulation of the broad scale evolution. The panels of Figs. 4 and 5 show 700 mb heights at the initial time and for each subsequent hour and a half of the forecast. The main feature was the devel-

opment of the synoptic scale low pressure system as it moved into the model domain from Colorado. At the same time, high pressure building in the east resulted in intensification of mean geopotential gradient over the domain. However, this intensification occurred more rapidly than was observed as a consequence of using time dependent boundary conditions computed from two sets of fields 12 hours apart. These boundary changes applied to the nine-hour forecast naturally exaggerated the low pressure development since its most rapid intensification occurred during the nine hours from 0600 to 1200 GMT 11 April after the end of the model run.

The horizontal resolution of the special SESAME radiosondes permitted the inclusion of subsynoptic scale structure in the initial state. It is believed that the inclusion of subsynoptic structure partially explains differences in the depiction of mesoscale precipitation between this simulation and those of Anthes et al. (1982) and Kaplan et al. (1982), both of which were initialized at essentially synoptic scale resolution. Major short waves during the SESAME AVE I observing period were confined to the lower troposphere between 500 and 850 mb. The initial state 700 mb height analysis (Fig. 4) shows the axes of three short wave troughs. A main short wave "M" along the Texas/Oklahoma border is so designated because it is the most pronounced and is the only one that is retained throughout the entire model simulation.

The smaller perturbations were included in the objective analysis since they appear to be real features related to observed precipitation. The wave in eastern Oklahoma is seen to coincide with the position of an observed precipitation band at 2100 GMT (see radar data, Fig. 8). A similar relationship between a mesoscale precipitation band and short wave will also be seen later in the context of the numerical model results. The
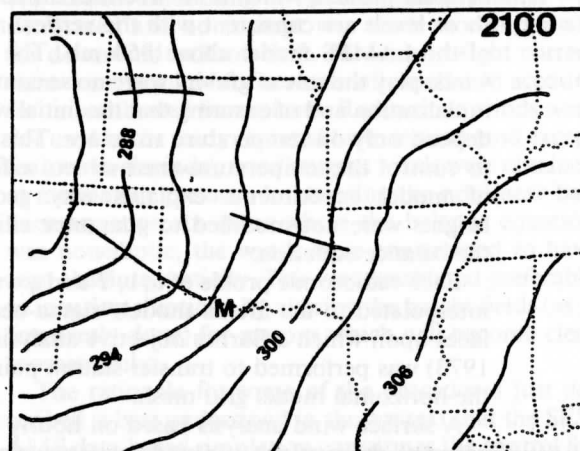

FIG. 4. Initial 700 mb geopotential height analysis (dekameters) at 2100 GMT. The location of the main short wave, "M", trough axis is indicated.
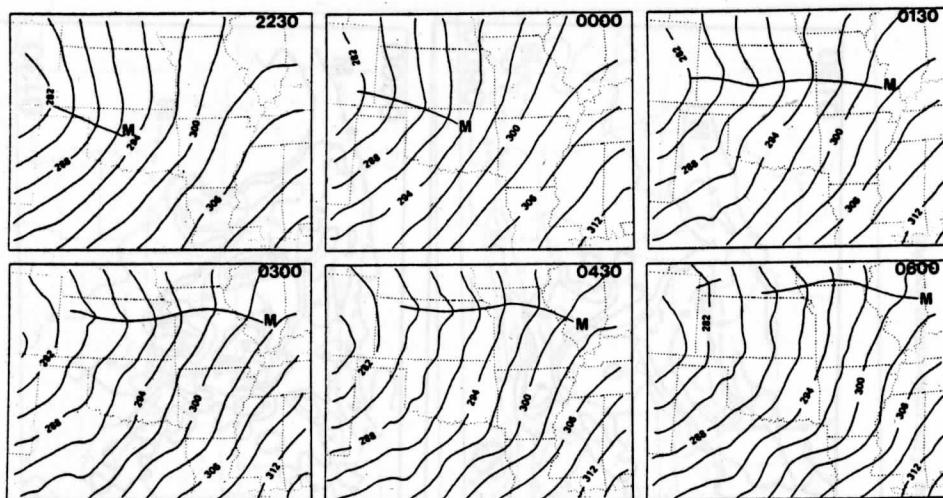
FIG. 5. 700 mb geopotential heights (dekameters) for every $1\frac{1}{2}$ hours of the model simulation. Times are indicated in the upper right-hand corner of each panel. Location of the main short wave trough axis is indicated.

small perturbation east of Colorado may be associated with the presence of precipitation there.

The response of the model to these smaller scale features was to eliminate them during the model initialization/adjustment period for two probable reasons. First, the model is initialized dry (i.e., unsaturated and without liquid water) so that it can not maintain the short waves by any dynamic response to diabatic heating related to the formation of clouds and precipitation (Wolcott and Warner, 1981). Second, observed winds at the initial time were highly ageostrophic and divergent, and the balance relationship being based on assumptions of large scale (synoptic scale) and nondivergence is unable to include vertical motions. Thus, the balanced winds do not represent the very small scales, especially for areas in which the mere existence of precipitation implies significant vertical motions.

The main short wave was maintained in the model and is seen in Fig. 5 propagating around the synoptic scale trough into northern Oklahoma by 0000 GMT. Continuity of this propagation is verifiable from model height fields between 2100 and 0000 GMT. Steady northward movement of the short wave is evident after 0000 GMT. When it reached southern Kansas, the length of the wave front increased and its transverse width decreased.

A noticeable loss of amplitude for the main short wave during the first three hours probably derives from the same inconsistency in using balanced winds as described above. Balanced winds could not include large divergence and vertical motion associated with the main short wave at 2100 GMT (see analyses of Moore and Fuelberg, 1981). Yet, by virtue of its larger scale, the inconsistency is less than for the smaller wave features and short wave "M" is assimilated into the model.

Despite arguments that initialization with mesoscale

temperature (geopotential) data may be unessential for accurate mesoscale forecasts, in this study an initial meso-alpha low-level short wave was retained, and, as will be seen, had a significant effect on the model precipitation simulation. Section 6 will examine mesoscale structure related to the propagating short wave and associated precipitation.

6. Mesoscale precipitation and short wave structure

The association of the 700 mb model short wave with a mesoscale precipitation band is illustrated in Figs. 6 and 7 where convective and grid scale precipitation rates are shown every 1.5 h from 2230 GMT. Superposition of the main short wave trough axis indicates that model precipitation developed initially in response to the short wave as it propagated around the large-scale trough and that convective precipitation was initiated at least 1.5 h earlier than the stable.

Examination of SESAME-AVE radiosonde data and hourly radar summaries from 10–11 April 1979 reveal the existence of a real-world counterpart to the model short wave precipitation band. The existence of a low-level propagating short wave (most prominent at 700 mb) has been discussed by Wilson (1982) who noted the correlation with a precipitation band. Hourly radar summaries (Fig. 8) and satellite IR images (not shown) clearly document the northward movement of a precipitation band from Oklahoma to Nebraska from about 2100 to 0600 GMT, as in the model simulation. The radar and model precipitation bands have very similar locations, rates of movement and spatial dimensions. Note the correspondence in the areal extents of observed and modeled precipitation bands at 0300 GMT 11 April.
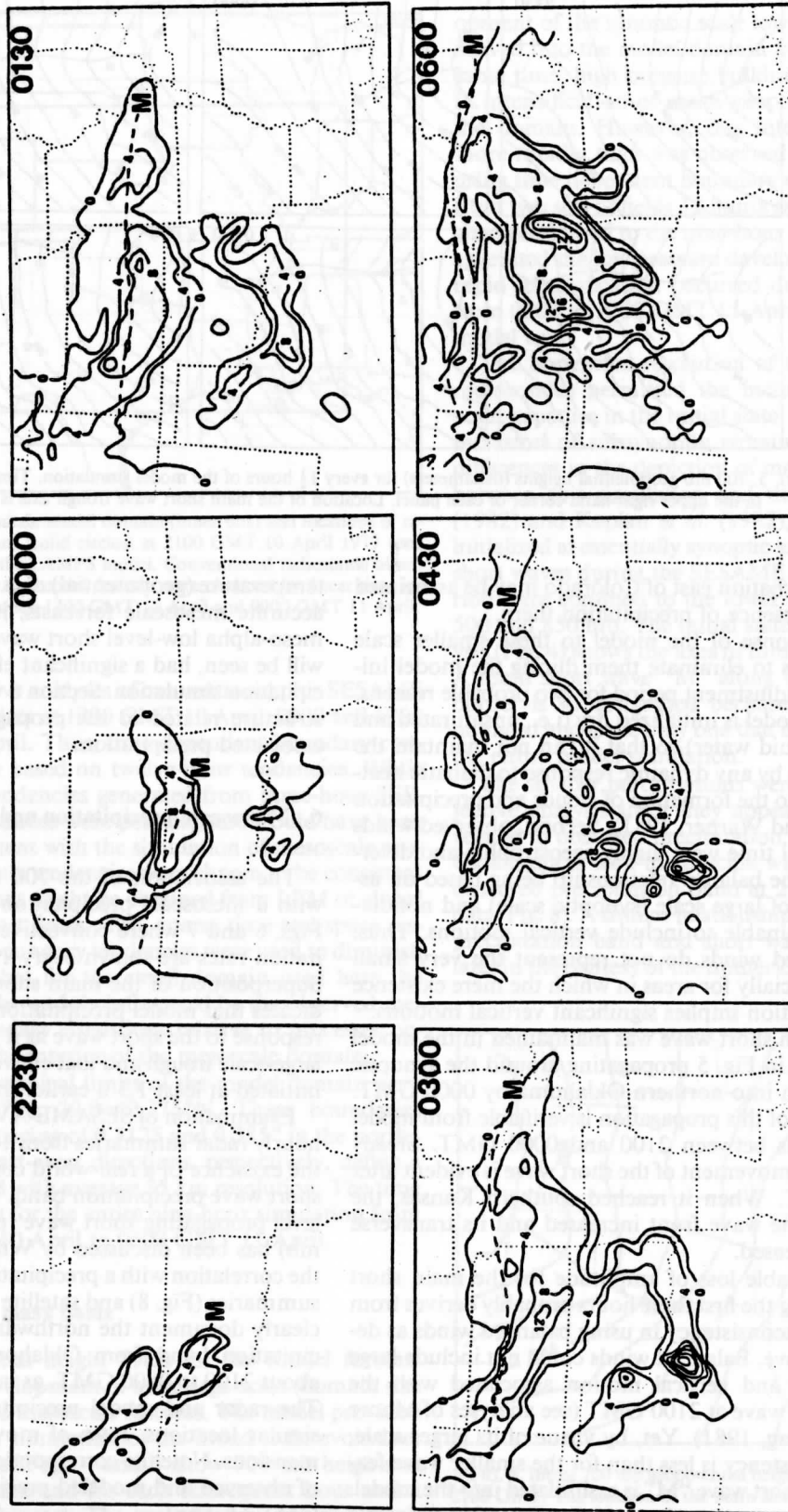
FIG. 6. Convective precipitation rates (10^{-4} mm s^{-1}) for every 1½ hours of the model simulation. Times correspond to those in Fig. 5. Location of the main short wave trough axis is indicated with a dashed line.
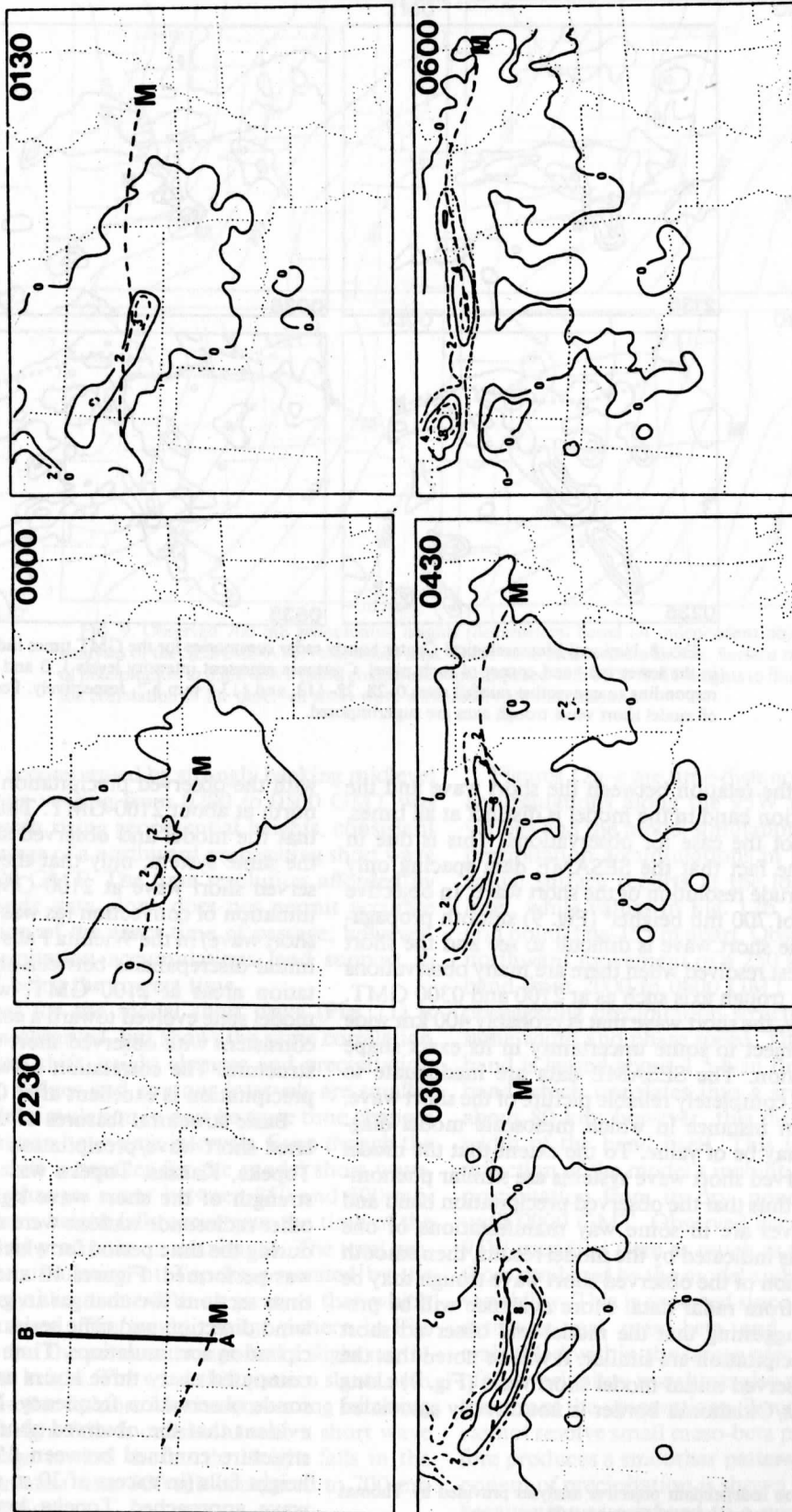
FIG. 7. As in Fig. 6 except for grid scale precipitation rates. The panel for 2230 GMT also shows the position of the cross-section line AB.
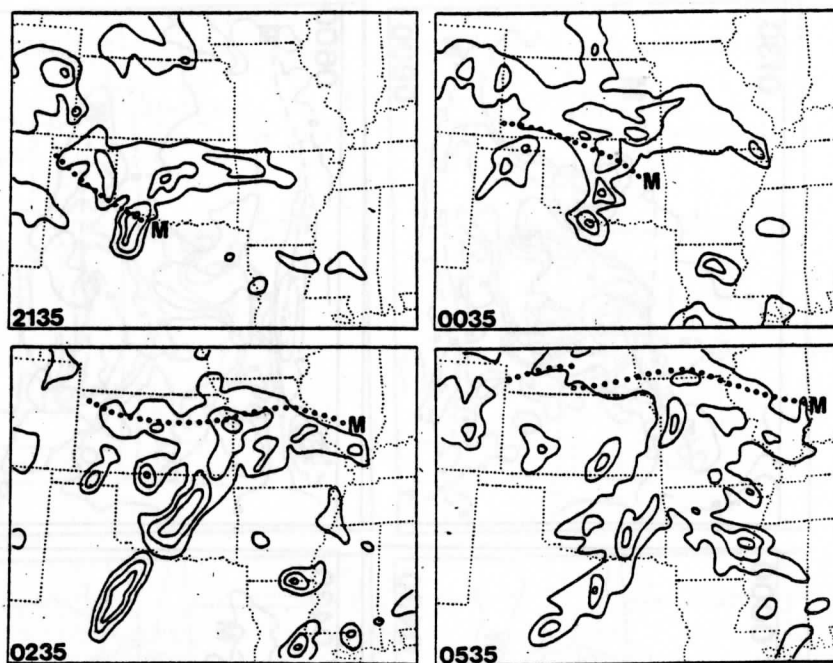
FIG. 8. National Meteorological Center hourly radar summaries for the GMT times indicated in the lower left-hand corner of each panel. Contours represent intensity levels 1, 3 and 5 corresponding to convective rainfall rates 0–28, 28–113, and 113+ mm h^{-1}, respectively. Positions of model short wave trough axes are superimposed.

While the relation between the short wave and the precipitation band in the model is distinct at all times, such is not the case for observations. This is due in part to the fact that the SESAME data spacing only permits crude resolution of the short wave. In objective analyses of 700 mb heights[1] (Fig. 9) smooth propagation of the short wave is difficult to see and the short wave is best resolved when there are many observations along the trough axis such as at 2100 and 0300 GMT. Obviously, the short wave that is probably 400 km wide is still subject to some uncertainty in its exact shape and location. The SESAME data are inadequate to provide a completely reliable picture of the short wave. This is an instance in which mesoscale model diagnostics may be of value. To the extent that the model and observed short wave systems are similar phenomena, and thus that the observed precipitation band and short waves are in some way manifestations of one another as indicated by the model results, then smooth propagation of the observed short wave trough may be inferred from radar data. More evidence will be presented suggesting that the model and observed short wave precipitation are similar. It will be noted that the main observed initial model short wave (Fig. 9) along the Texas/Oklahoma border is not directly associated

with the observed precipitation band which is farther north at about 2100 GMT. Thus it can not be argued that the model and observed short wave systems are the same system, only that they are similar. The observed short wave at 2100 GMT has been linked to initiation of convection (as was the case for the model short wave) in the Wichita Falls outbreak area. Despite initial discrepancies between short wave and precipitation areas at 2100 GMT, within three hours the model state evolved toward a configuration remarkably consistent with observed short wave and precipitation structure. The correlation between real and modeled precipitation is excellent after 0000 GMT.

Basic structural features of the observed and simulated short wave/precipitation band are compared at Topeka, Kansas. Topeka was chosen because of the strength of the short wave signal there and because other radiosonde stations were affected by missing data during the time period for which the model simulation was performed. Figures 10 and 11 consist of vertical time sections for changes in geopotential height and wind direction and time series for hourly surface precipitation accumulations. Time changes in Fig. 10 were computed every three hours as necessitated by radiosonde observation frequency. From these figures it is evident that the observed short wave was a midlevel structure confined between 850 and 500 mb. Large height falls (in excess of 30 m at 700 mb) as the short wave approached Topeka between 2300 and 0200

---

[1] Based on independent objective analyses provided by Thomas Q. Carney, personal communication, 1981.
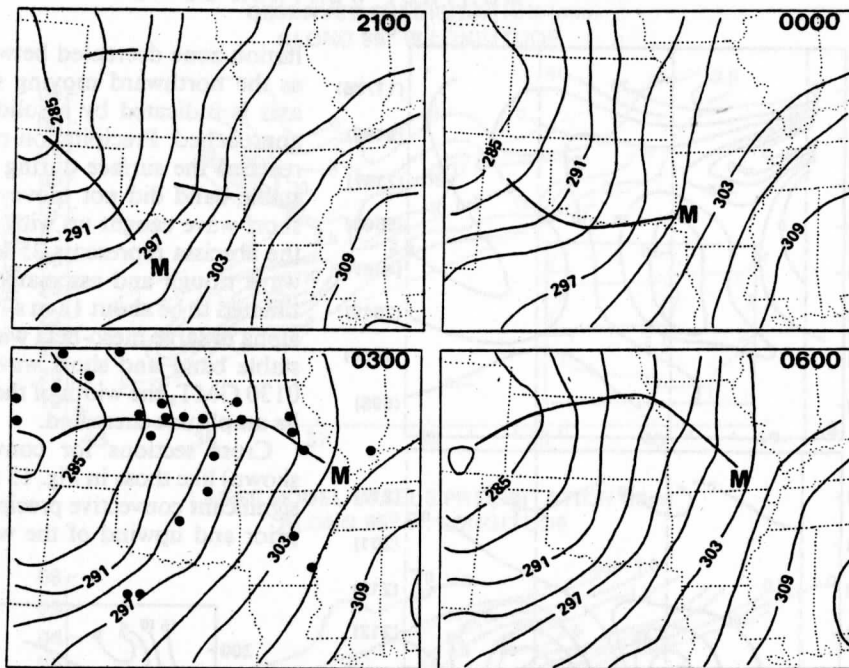
FIG. 9. Observed 700 mb geopotential heights (dekameters) based on independent objective
analyses of the SESAME-AVE radiosonde data. Short wave locations are shown. Surface reports
of precipitation at 0300 GMT (solid circles) are superimposed with 0300 GMT heights to illustrate
the correlation of the observed short wave with observed precipitation.

GMT were accompanied by strongly backing midlevel
winds. Strong veering from 0200 to 0500 GMT was
associated with rising geopotential heights, consistent
with the passage of a northward propagating short wave
around 0200 GMT. The time resolution afforded by
the radiosonde data alone does not permit accurate
determination of the exact time of passage; however,
hourly precipitation accumulations lend support to
0200 GMT being the correct time.

The signal for the model short wave (Fig. 11) is
weaker than observed, but shows the same correlation
between wind shift, height changes and precipitation
occurrence. Values and contour intervals are smaller
for the model simulation in part because time changes
are based on one-hour time intervals. Even though the
total wind shift is smaller for the model short wave,
the greatest changes occur between 850 and 500 mb.
The maximum height falls occur near the time of the
wind shift and precipitation maximum. The total pre-
cipitation accumulation at Topeka generated by the
model is only about one-fifth as great as that which
actually occurred. The height change pattern in Fig.
11 suggests that the pressure trough had a slight north-
ward tilt with height. The wind shift pattern slants with
height in a similar fashion. Maximum veering following
maximum height falls is consistent with a short wave
trough passage toward the north. Height falls in the
model are greatest near 900 mb compared to 700 mb
from observations.

Figures 12a–c are time-distance plots of precipitation
accumulations along the 95W meridian from obser-
vations and the model simulation, respectively. Hourly
precipitation accumulations in Fig. 12a are based on
actual surface reports at the locations shown in the
inset, while values in Fig. 12b, c are based on model
grid point data 35 km apart. Observations clearly show
northward movement of a 250 km wide precipitation
band from 2000 to 0600 GMT. The model reveals a
propagating precipitation structure having nearly the
same width and phase speed. The model precipitation
band is lagged about 1.5 h in time from the observed
band which translates into a spatial displacement of
about 80 km; however, this distance is less than the
width of the band itself. This time lag is partially a
reflection of the model's inability to quickly "spin up"
precipitation from its dry, nondivergent initial state
until 0000 GMT. Observed accumulations along the
95W meridian were as much as ten times greater than
those produced by the model and showed greater spatial
variability. This is expected since the observations were
detecting real meso-beta and meso-gamma events
embedded within the larger precipitation band. Some
of this variability may have also resulted from unequal
spacing of the observations. By comparison, the model
cannot resolve small meso-beta phenomena and there-
fore produces a smoother pattern. The grid scale com-
ponent of precipitation is shown separately in Fig. 12b
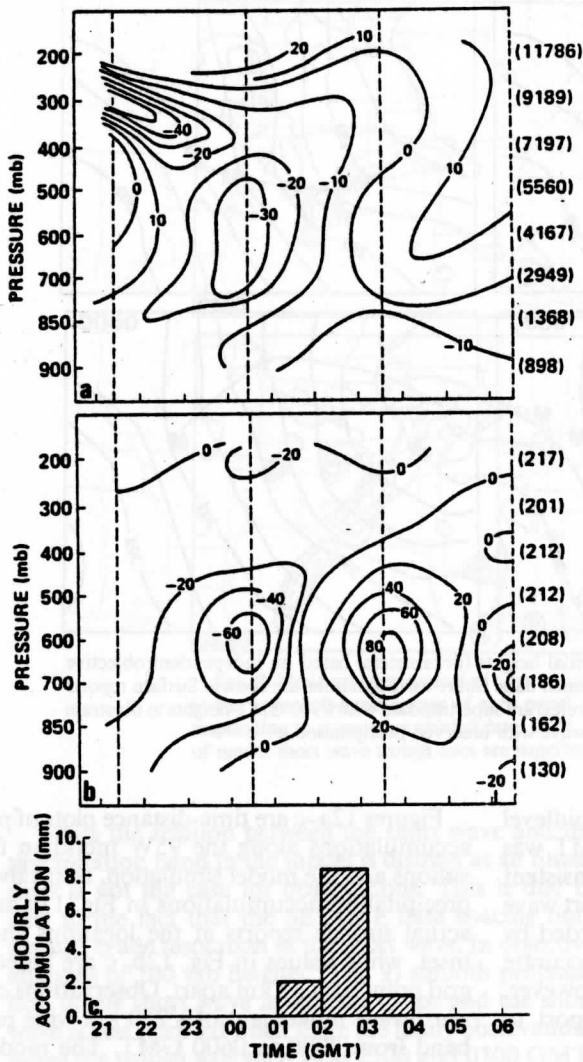because it was confined to a narrower band than the

FIG. 10. Time–height sections at Topeka, Kansas for (a) change in geopotential height (meters), (b) change in wind azimuth (degrees) and (c) observed hourly precipitation accumulations. Values in parentheses to the right of (a) and (b) are average values of geopotential height and azimuths, respectively. Vertical dashed lines correspond to the times for which time centered changes could be computed.

itation zone decreased between 0000 and 0130 GMT as the northward moving short wave (whose trough axis is indicated by a solid square along the x-axis) approached. Precipitation rates increased and rainfall reached the surface during this interval of time. The stable band did not move until after 0130 when the short wave caught up with it. Since each tic mark on the abscissa represents 35 km, the speed of this short wave trough and associated precipitation band is estimated to be about 18 m s^{-1} and to have a small meso-alpha or large meso-beta width around 250 km. As the stable band and short wave became aligned around 0130 GMT, the width of the short wave decreased and its amplitude increased.

Cross sections for convective precipitation (not shown) like those in Fig. 13 revealed that at 0000 GMT significant convective precipitation had already formed prior and upwind of the weaker stable precipitation.
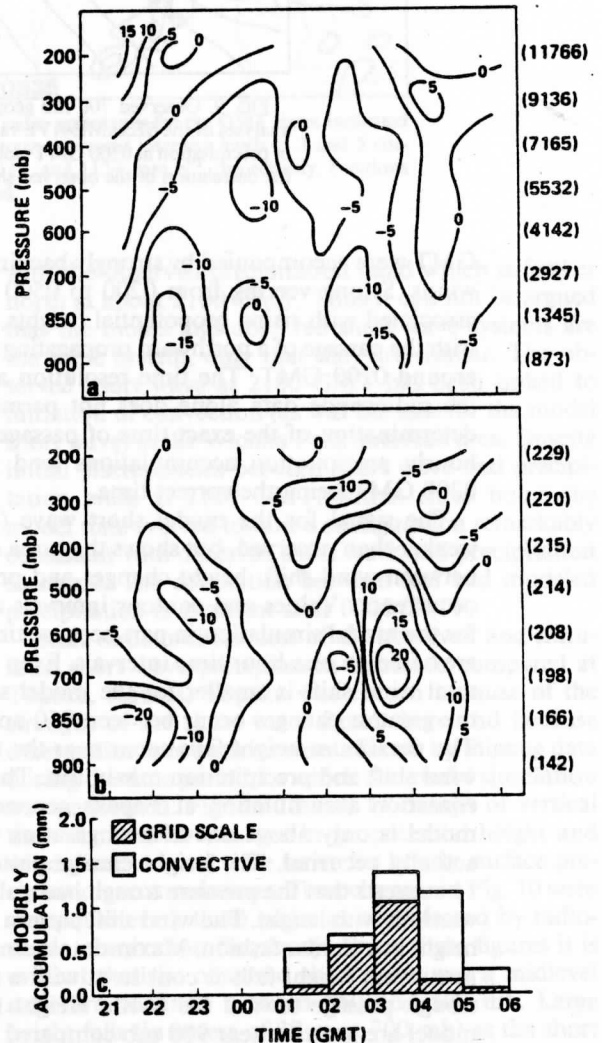

FIG. 11. As in Fig. 10 except all values are computed and displayed hourly from mesoscale model output.

convective precipitation and better defined the short wave trough axis. The convective precipitation accumulations (Fig. 12c) were up to twice as large as for the stable component.

Attention is now turned to internal structure of the model short wave which would not be discernible from conventional observations. In Fig. 13, a time sequence of vertical cross sections along line AB (see Fig. 7) illustrates the evolution of the stable precipitation band. Contours represent half-hourly accumulations of grid scale precipitation at the times and levels indicated on each cross section. The initial generation of rain occurred around 0000 GMT over a fairly broad area between 400 and 600 mb. The width of the main precip-

OBSERVED PRECIPITATION (mm)
ALONG 95° W LONGITUDE

LAMPS MODEL STABLE PRECIPITATION (mm)
ALONG 95° W. LONGITUDE

LAMPS MODEL CONVECTIVE PRECIPITATION (mm)
ALONG 95°W. LONGITUDE

LATITUDE °N

FIG. 12. Time–distance plots of precipitation accumulations from 2100 GMT 10 April to 0600 GMT 11 April along the 95°W long. Top inset shows stations from which 12a display was constructed. Panel 12b is based on a model output and shows only the grid scale component of precipitation and Panel 12c shows the model convective component of precipitation.

This is also evident from comparison of Figs. 6 and 7 and suggests that moistening of the grid scale environment via detrainment of vapor and cloud water in the convective parameterization was responsible in part for initiating the stable precipitation in midtroposphere. The overhanging precipitation area in Fig. 13 resulted

0000

0130

0300

PRESSURE (mb)

0430

0600

A B
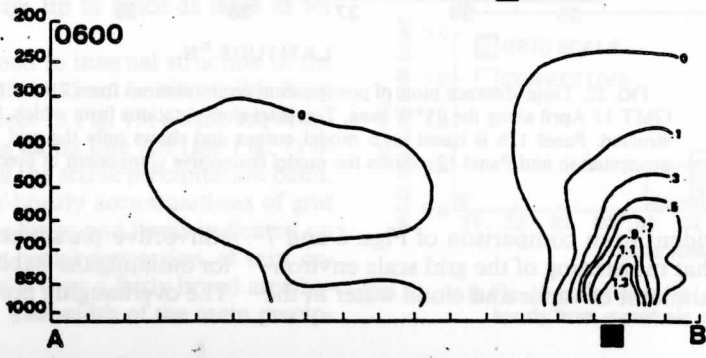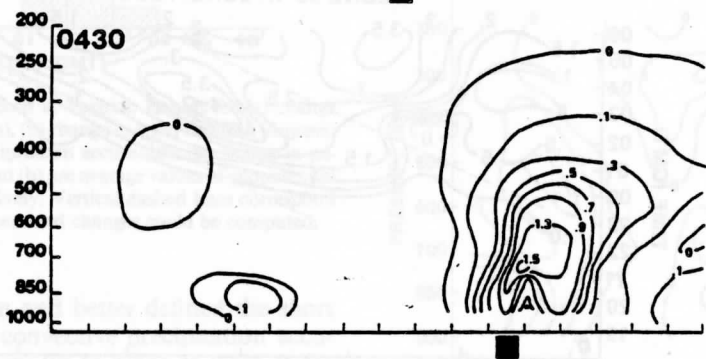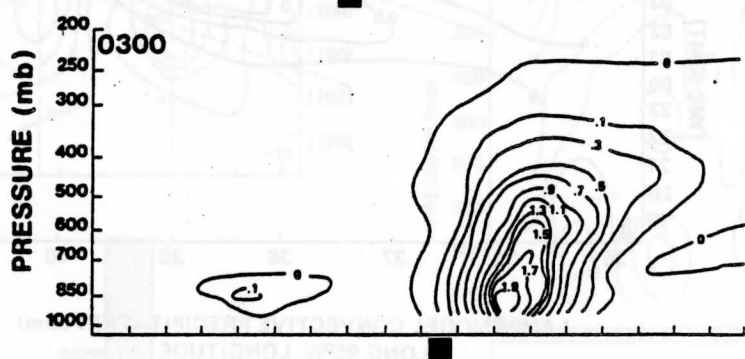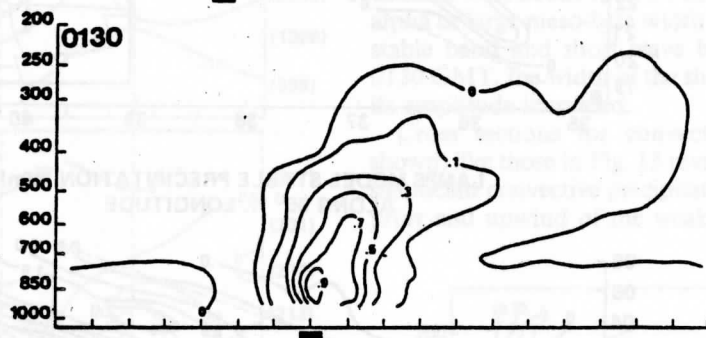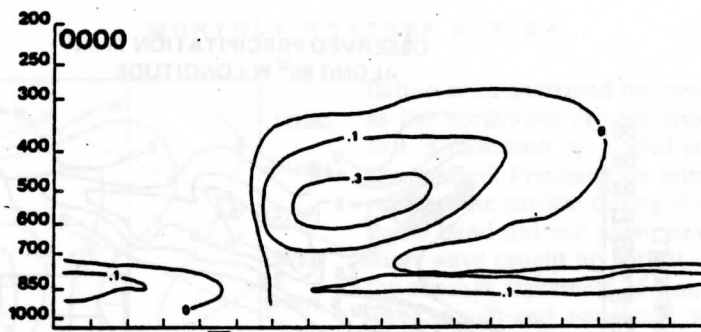
from lifting and condensation of moisture advected along inclined isentropic surfaces. A convective component of the total precipitation propagated northward just to the rear of the stable band along cross section AB for the entire simulation.

Direct correspondence of the 700 mb trough axis with low-level mesoscale bands of convergence, upward motion and cyclonic relative vorticity is seen in Fig. 14 along with a map of rain water at 700 mb. In Fig. 15, a time sequence of vertical cross sections for vertical velocity, potential temperature and divergence along the line AB (shown in Fig. 7) helps to highlight vertical structure. The first manifestation of the short wave in this sequence appears at 0000 GMT as a narrow band of upward motion with a maximum positive value of about 16 cm s^{-1} near 500 mb. Subsequent frames show the northward propagation and intensification of vertical velocities in the short wave. The maximum value in the short wave increased to 35 cm s^{-1} after 0000 GMT as precipitation rates were increasing.

Vertical motion in the short wave is supported by a well-developed divergence pattern consisting of a vertically sloping convergence band which precedes the short wave trough, and a divergence band which follows it. The two are parallel and tilt downwind with height in the direction of the propagation (see Fig. 16) over a horizontal distance of about 300 km. This tilt corroborates that inferred earlier from Fig. 11 and gives low-level convergence overlain by upper level divergence at the trough axis. The entire system extends to the tropopause near 10 km.

While strong midlevel diabatic heating within the precipitation band is confirmed directly by Fig. 17 (compare with Fig. 11), the effects of this heating are seen in Fig. 15 from diverging isentropic surfaces at the mature short wave axis. The 310 K surface dips downward sharply at the vertical velocity maximum (center of the short wave). Farther aloft where adiabatic cooling exceeds latent heating, the 320 K surface is forced upwards. Net heating caused by latent heat release in precipitating columns forces vertical expansion of isobaric surfaces to induce locally high pressure and horizontal mass divergence in the upper troposphere. The resultant net evacuation of mass from the column causes pressure heights to fall at the lower levels, providing the mechanism by which the onset of precipitation apparently forces an intensification of the model 700 mb short wave. Eventually, midlevel heating stabilizes the lower troposphere, reducing low-level upward motion and convergence (as seen in Fig. 15), and thus the upward transport of moisture whose condensation helps drive the vertical circulation in the short wave. Ultimately the short wave/precipitation system begins to decay after 0300 GMT as is seen in the height and precipitation fields.

This paper has focused on documenting structural features of the model short wave. Before concluding, however, it is appropriate to briefly mention other aspects of the precipitation simulation. In addition to the propagating precipitation band, the model provided a good simulation of convective precipitation in central Oklahoma and along the Texas/Oklahoma border. At 2100 GMT a squall line was seen to develop southwest of the Wichita Falls tornado outbreak area and increase in length by building progressively northeastward through Oklahoma as the short wave precipitation band propagated northward (refer to radar, Fig. 8). Eastward translation of the observed squall line was only about 100 km during the following nine hours. Significant precipitation in the model was not forecast on the Texas/Oklahoma border until 0000 GMT (refer to Fig. 6) when in reality heavy convection had been existent there since 1800 GMT. It is noteworthy that the model precipitation that did form was almost entirely convective and was confined to a narrow band at 0130 and 0300 GMT suggestive of the observed 10 April squall line. However, its orientation was about 30° clockwise from the observed squall line. Areal expansion of the model convective precipitation over Oklahoma, Kansas, Arkansas and Missouri after 0300 is consistent with radar summaries after 0235 GMT. The southwest–northeast orientation of this growing precipitation area is as observed in the radar data.

While the model was unable to simulate development of this "squall line" farther into central Texas after 0000 GMT, there is evidence that the forecast was tending in that direction. The 700 mb relative humidity analysis at 0600 GMT (Fig. 18) shows a tongue of relatively moist air extending down into Texas very close to the observed squall line position; saturation, however, was never achieved. This moist tongue was associated with low-level convergence and upward transport of moisture along the modeled surface cold front which was moving slowly into central Texas from the west as observed (compare 0300 GMT observed surface frontal positions and 700 mb vertical motion in Fig. 14).

7. Summary and conclusions

Results were presented from a limited area 35 km mesh mesoscale model simulation initialized with SESAME-AVE I radiosonde data for 10 April 1979. The model was statically initialized using balanced winds at 2100 GMT 10 April and was terminated at 0600 GMT 11 April to encompass a nine-hour period

FIG. 13. Time sequence of vertical cross sections (AB) for half-hourly stable precipitation accumulations (mm). Times are indicated on each cross section. The location of the short wave trough axis (vertical velocity maximum) is shown by solid squares.

VOR

M

DIV

RAIN WATER

(observed surface fronts)

VERTICAL VELOCITY
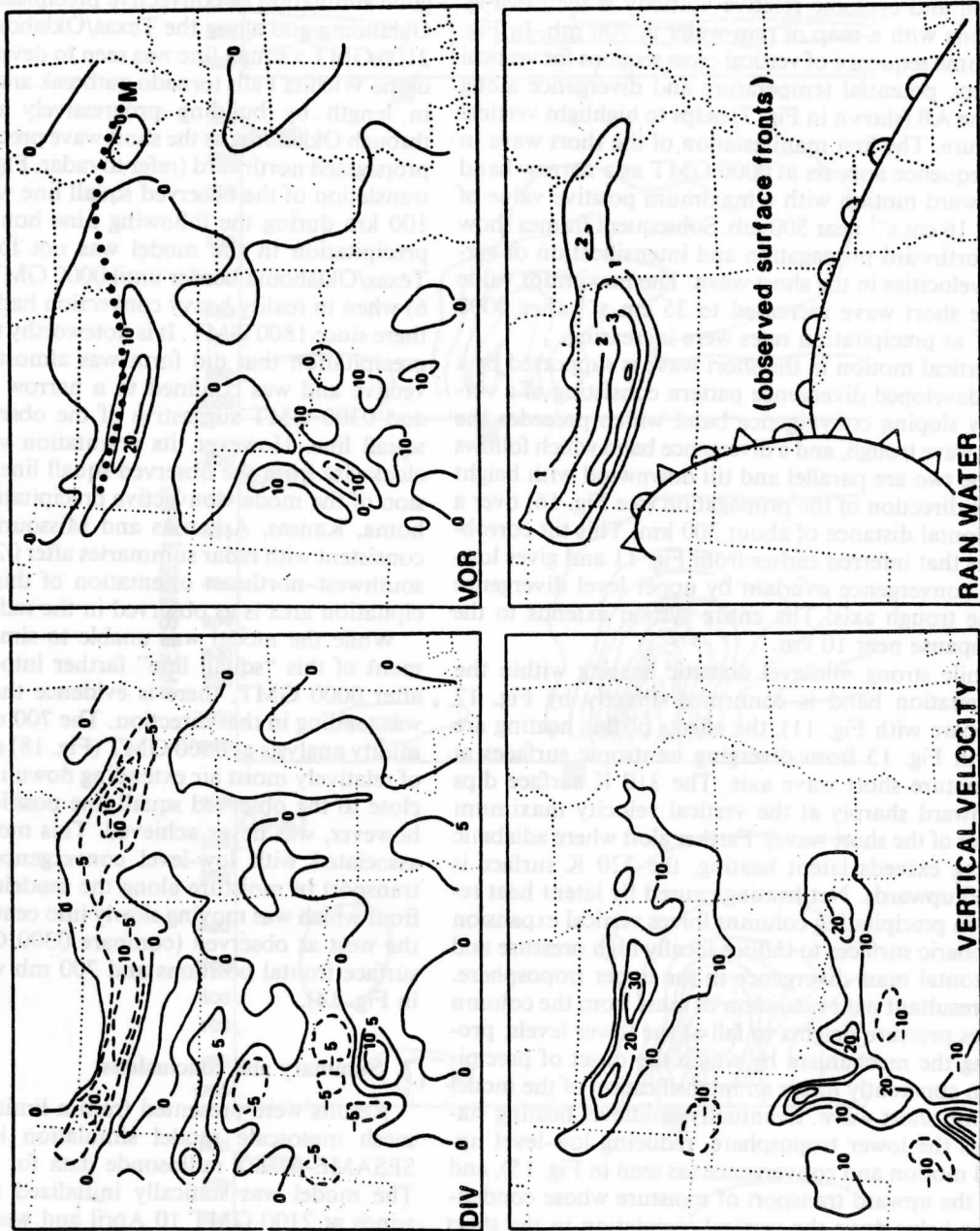
FIG. 14. Maps at 0300 GMT showing the correspondence of 700 mb divergence (10^{-5} s^{-1}), 700 mb cyclonic relative vorticity (10^{-5} s^{-1}), 700 mb upward motion (cm s^{-1}) and rain water (g kg^{-1}) with the 700 mb short wave trough axis (upper right panel, dotted line). Observed NMC surface frontal positions are shown in the lower right panel for comparison with model vertical velocity patterns at the same time.
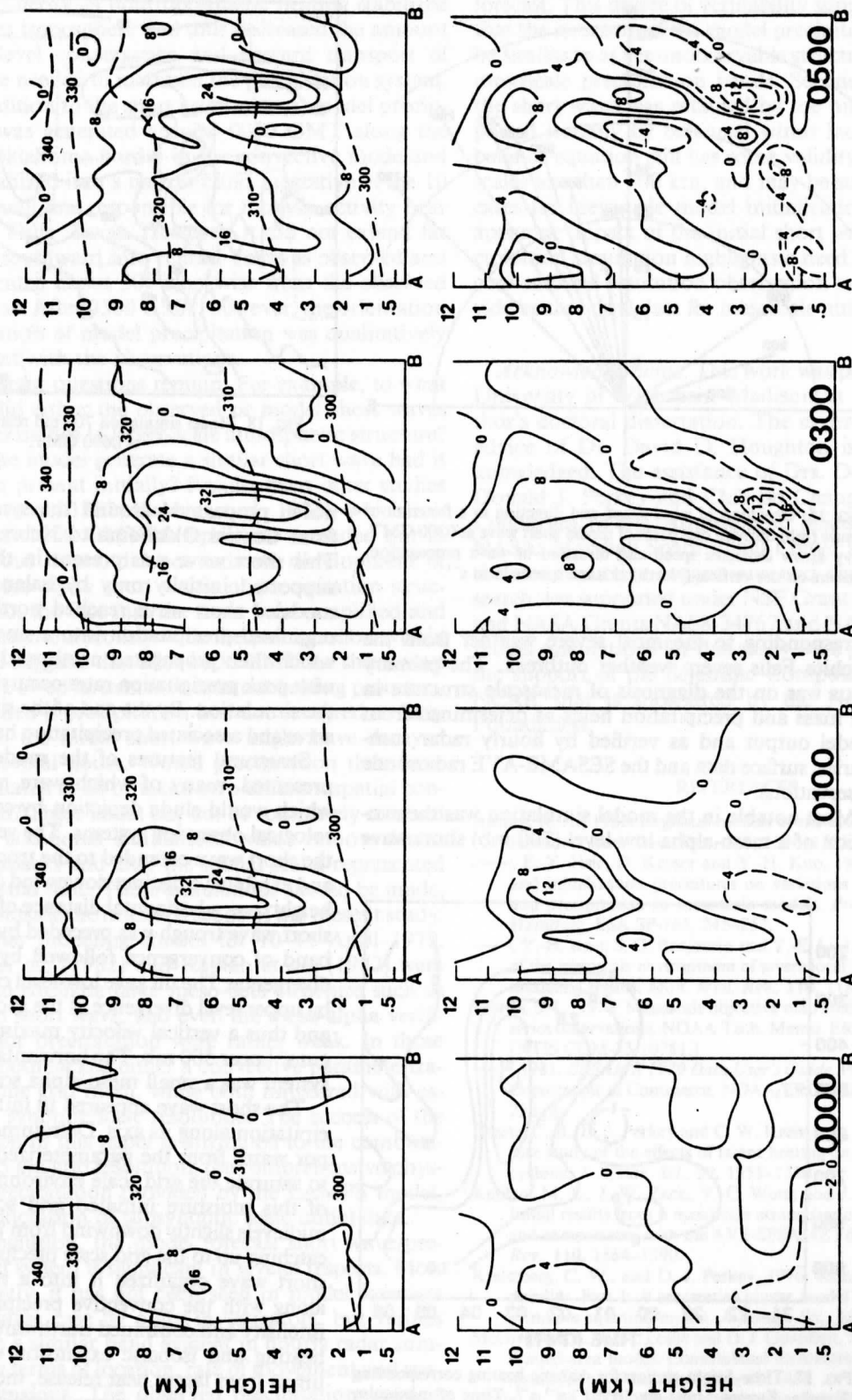
FIG. 15. Vertical cross sections (AB) for vertical velocity (upper panels, cm s⁻¹) and divergence (lower panels, 10⁻⁵ s⁻¹) at 0000, 0100, 0300 and 0500 GMT. Dashed lines in the upper panels are isentropes in Kelvin.
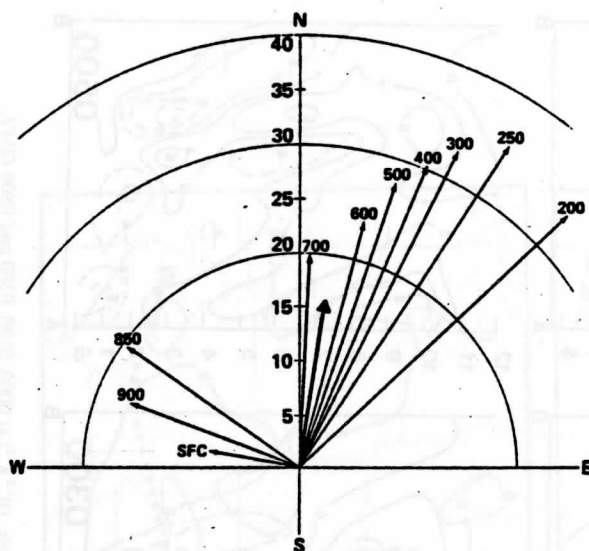
FIG. 16. Depiction of wind speed and direction as a function of pressure (mb) through one point of model short wave at 0300 GMT. Heavy arrow indicates speed and direction of wave propagation. Numbers on the vertical (North) axis are speeds in m s^{-1}.

FIG. 18. Model simulation 700 mb relative humidity (%) at 0600 GMT.

corresponding to the most severe weather from the Wichita Falls severe weather outbreak. The primary focus was on the diagnosis of mesoscale structure in the mass and precipitation fields as determined from model output and as verified by hourly radar summaries, surface data and the SESAME-AVE radiosonde observations.

Most notable in the model simulation was the evolution of a meso-alpha low-level (700 mb) short wave
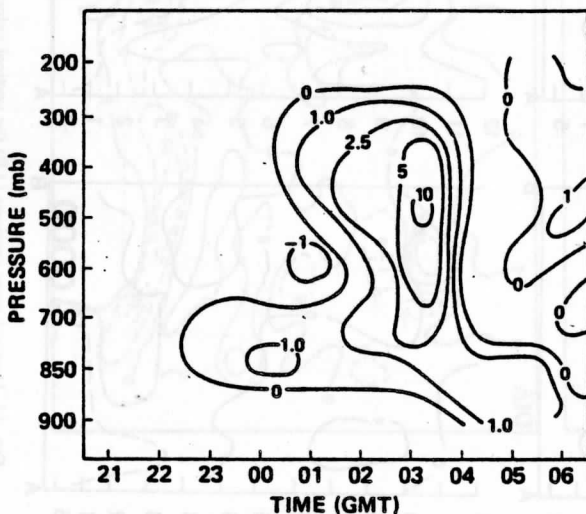
which propagated around the synoptic scale trough from Central Oklahoma to Nebraska in nine hours. This short wave was present in the initial state and supported initially only by balanced winds. As the modeled short wave reached northern Oklahoma, it organized precipitation into a single mesoscale band which then propagated northward at about 18 m s^{-1} with peak precipitation rates occurring at six hours into the simulation. By the end of the simulation, the short wave and associated precipitation had nearly dissipated.

Structural features of the model short wave were presented, many of which were manifested at scales which would elude depiction by conventional meteorological observing systems. The vertical circulation in the short wave extended to the tropopause near 10 km and exhibited a distinct downwind (northward) tilt with height over a horizontal distance of about 300 km. The short wave trough was preceded by a vertically sloping band of convergence followed by a parallel band of divergence. The tilt gave low-level convergence overlain by upper level divergence at the short wave trough axis, and thus a vertical velocity maximum in excess of 35 cm s^{-1} near 500 mb. The horizontal width of the entire system was a small meso-alpha scale 200–300 km.

The short wave appeared to initiate convective precipitation along its axis. Detrainment of cloud and vapor water from the parameterized convection helped to saturate the grid scale environment, and advection of this moisture initiated grid scale precipitation at midlevels slightly downwind from the convection. After catching up to the grid scale precipitation, the traveling short wave organized it into a narrow band which, along with the convective precipitation, increased in intensity and continued northward with the wave. Net heating and isobaric expansion of precipitating columns from latent heat release, induced the horizontal mass divergence at upper levels, to explain a sudden intensification of the short wave trough with the onset

FIG. 17. Time–height section for diabatic heating corresponding to Topeka, Kansas. Units are 10^{-4} J kg^{-1} s^{-1}. Time of maximum heating rates corresponds to passage of short wave precipitation band as depicted in Fig. 11.
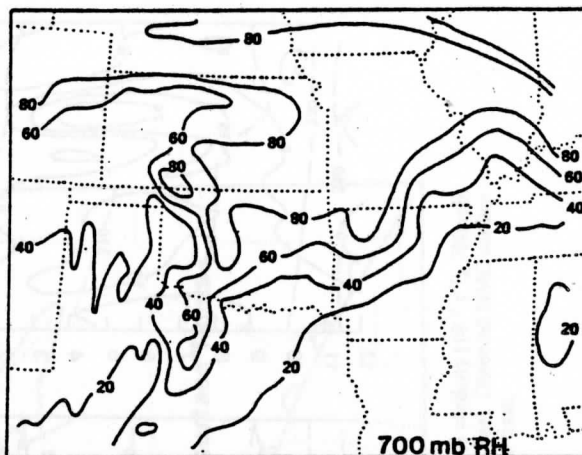
of precipitation. The short wave and precipitation band began to decay as midtropospheric heating stabilized the lower troposphere and thus decreased the amount of low-level convergence and upward transport of moisture needed to maintain the precipitation system.

In addition to the short wave system, model precipitation was generated around 0000 GMT along the Texas/Oklahoma border in the convective mode and was organized into a narrow band suggestive of the 10 April squall line responsible for tornado activity near Wichita Falls, Texas. However, it did not extend far enough southward into central Texas as observed and was oriented about 30° clockwise from the observed squall line. After 0300 GMT, however, the orientation and location of model precipitation was qualitatively consistent with the observations.

Important questions remain. For example, to what degree did either the observed or model short waves owe its existence to larger-scale atmospheric structure? Could the model generate a similar short wave had it not been present initially? Results from other studies (Anthes et al., 1982; Kaplan et al., 1982), which initialized at 1200 GMT 10 April and extended out to twenty-four hours, did not indicate development of small meso-alpha short waves or precipitation structure. Also, the fact that the short wave amplified and decayed simultaneously with the precipitation within the band suggests that after 0000 GMT the short wave may have owed its existence to latent heating processes. If true, then if precipitation had not occurred as early as it did, the initial short wave might have decayed within several hours. Would precipitation then have been initiated at all or taken on a different spatial configuration? These issues can not be completely resolved without additional simulations which remove latent heat feedbacks and alter the spatial scales represented in the initial state. These simulations should be made, but fall outside the intended scope of the present study.

In other modeling studies for 10–11 April 1979, Anthes et al., (1982) and Kaplan et al., (1982) were unable to simulate large meso-beta structure such as the main short wave, and even the meso-alpha verifications for precipitation were rather weak. In those studies, both lacked either a convective parameterization or fine grid mesh, while both initialized with essentially synoptic scale resolution. The success of the simulation in this paper is attributed to the combination of 35 km grid resolution, the comprehensive physics for precipitation provided by the LAMPS model, and the inclusion of subsynoptic scale initial data.

In conclusion, the model forecast short wave/precipitation system is significant in several respects. Most importantly, it has not been seen in model forecasts for the same case by other investigators, but verifies well with a similar band evident in hourly radar summaries in terms of location, rate of movement and spatial dimensions. The observed precipitation band is seen to be associated with a 700 mb short wave in SESAME-AVE height analyses, just as in the model forecast. This degree of verifiability supports the notion that the structure of the model precipitation band may be similar to as yet unobservable structure in some real mesoscale precipitation bands. Second, the fact that the short wave was retained by the model while supported initially by balanced winds indicates that the balance equation still has some validity at meso-alpha scales less than 500 km, and may be suitable in many cases for mesoscale model initialization. Finally, the apparent impact of the initial short wave on the precipitation simulation highlights a need for higher than conventional resolution observation networks to provide better initial data for mesoscale numerical models.

REFERENCES

Anthes, R. A., 1983: Regional models of the atmosphere in middle latitudes. *Mon. Wea. Rev.*, **111**, 1306–1335.

——, E.-Y. Hsie, D. Keyser and Y.-H. Kuo, 1981: Impact of data and initialization procedures on variations of vertical motion and precipitation in mesoscale models. *Proc. IAMAP Symp.*, Hamburg, ESA SP-165, 245–257.

——, Y.-H. Kuo, S. G. Benjamin and Y.-F. Li, 1982: The evolution of the mesoscale environment of severe local storms; preliminary modeling results. *Mon. Wea. Rev.*, **110**, 1187–1213.

Barnes, S. L., 1973: Mesoscale objective map analysis using weighted series observations. NOAA Tech. Memo. ERL-NSSL-62, 60 pp. [NTIS COM-73-10781.]

——, 1981: *SESAME 1979 Data User's Guide.* Project Sesame, U.S. Department of Commerce, NOAA/ERL Building, Boulder, CO, 236 pp.

Chang, C.-B., D. J. Perkey and C. W. Kreitzberg, 1982: A numerical case study of the effects of latent heating on a developing wave cyclone. *J. Atmos. Sci.*, **39**, 1555–1570.

Kaplan, M. L., J. W. Zack, V. C. Wong and J. J. Tuccillo, 1982: Initial results from a mesoscale atmospheric circulation system and comparisons with the AVE-SESAME I data set. *Mon. Wea. Rev.*, **110**, 1564–1590.

Kreitzberg, C. W., and D. J. Perkey, 1976: Release of potential instability. Part I: A sequential plume model with a hydrostatic primitive equation model. *J. Atmos. Sci.*, **33**, 456–475.

McGregor, J. L., L. M. Leslie and D. J. Guantlett, 1978: The ANMRC limited-area model: Consolidated formulation and operational results. *Mon. Wea. Rev.*, **106**, 427–438.

Moller, A. R., 1980: Mesoscale surface analysis of the April 10, 1979 tornadoes in Texas and Oklahoma. *Preprints, Eighth Conf. on*

Weather Forecasting and Analysis, Denver, Amer. Meteor. Soc., 36–43.

Moore, J. T., and H. E. Fuelberg, 1981: A synoptic analysis of the first AVE-SESAME '79 period. *Bull. Amer. Meteor. Soc.*, 62, 1577–1590.

Orlanski, I., 1975: A rational subdivision of scales for atmospheric processes. *Bull. Amer. Meteor. Soc.*, 56, 527–530.

Perkey, D. J., 1976: A description and preliminary results from a fine mesh model for forecasting quantitative precipitation. *Mon. Wea. Rev.*, 104, 1513–1526.

——, 1980: Impact of moisture on regional scale numerical model simulations. *Atmospheric Water Vapor*, A. Depak, T. D. Wilkerson and L. H. Ruhnke, Eds., Academic Press, 513–526.

——, and C. W. Kreitzberg, 1976: A time dependent lateral boundary scheme for limited area primitive equation models. *Mon. Wea. Rev.*, 104, 744–755.

Robertson, F. R., and P. J. Smith, 1983: The impact of model moist processes on the energetics of extratropical cyclones. *Mon. Wea. Rev.*, 111, 723–744.

Ross, R. B., and I. Orlanski, 1982: The evolution of an observed cold front. Part I: Numerical simulation. *J. Atmos. Sci.*, 39, 296–327.

Washington, W. M., and D. P. Baumhefner, 1975: A method of removing lamb waves from initial data for a primitive equation model. *J. Appl. Meteor.*, 14, 114–119.

Wilson, G. S., 1982: The structure and dynamics of mesoscale systems influencing severe thunderstorm development during AVE/SESAME I. *Preprints, 12th Conf. on Severe Local Storms*, San Antonio, Amer. Meteor. Soc., 192–196.

Wolcott, S., and T. T. Warner, 1981: A moisture analysis procedure utilizing surface and satellite data. *Mon. Wea. Rev.*, 109, 1989–1998.

A Quantitative Study of Satellite Winds for Mesoscale Meteorology

DONG KYOU LEE AND DAVID D. HOUGHTON

A Quantitative Study of Satellite Winds for Mesoscale Meteorology

DONG KYOU LEE[1] AND DAVID D. HOUGHTON

Department of Meteorology, University of Wisconsin, Madison, WI 53706

(Manuscript received 13 October 1982, in final form 30 January 1984)

ABSTRACT

Quantitative characteristics and utility of mesoscale satellite winds are investigated for a low-level high spatial resolution data set obtained from a sequence of 6 min interval synchronous meteorological satellite images of the central region of the United States on 20 May 1977. Attention is focused on the quantitative errors introduced by height assignment in the presence of vertical wind shear and by the objective analysis of such irregularly spaced data to a regular grid point array.

It is shown that assignment of the wind vectors to a single level introduces a local variability and systematic horizontal shears due to the vertical wind-shear effect giving a variability comparable to that expected in natural mesoscale phenomena with 100 km length scale. The random component of the local variability can be reduced by appropriate averaging which is possible because of the data density.

The error introduced by the objective analysis procedure is estimated by examining the differences between various analysis methods. This sensitivity test is made both for grid spacing and for objective analysis method and includes the use of an analytical function field. Although there is a large variation in the results, it is estimated for the more reasonable cases that the variations in most areas are not greater than those expected from other error sources.

1. Introduction

Using geosynchronous satellite imagery, numerous attempts have been made to develop and improve the generation, processing and utilization of the displacement vectors of cloud motion for both research and operational purposes during the last decade. The development of highly automated data-handling facilities, such as McIDAS (Man–computer Interactive Data Analysis System at the University of Wisconsin) and AOIPS (Atmospheric Oceanographic Information Processing System at Goddard Space Flight Center) has made it possible to obtain large numbers of displacement vectors rapidly in a precise manner. Displacement vectors determined in this way hereafter are termed "satellite wind vectors."

Characteristics of large-scale satellite wind vectors have been discussed in many types of study. Hubert and Whitney (1971) and Hubert and Timchalk (1972) showed that in the tropical regions synoptic-scale low-level satellite wind vectors (at the cumulus cloud level) corresponded closely to rawinsonde winds. Fujita *et al.* (1975) showed the flow patterns of tropical circulations from the satellite wind vectors and Vieze *et al.* (1972) found that the patterns of divergence and vorticity fields computed from satellite wind vectors were consistent with development, location and movement

of extratropical cyclone disturbances. Bauer (1976) and Suchman and Martin (1976) concluded that satellite wind vectors could represent atmospheric motion within the accuracy of the conventional data for the synoptic scale. The National Weather Service (NWS) is operationally incorporating synoptic-scale satellite wind vectors into daily weather analyses.

The usefulness of mesoscale satellite wind information has been a subject of discussion and research. Recently there have been numerous studies concerning the characteristics and utility of mesoscale satellite wind vectors. Tecson *et al.* (1977) characterized tracking methods for different types of configurations of clouds for revealing mesoscale disturbances using rapid-scan images for severe storm cases. Johnson and Suchman (1980) examined the effect of variation in the time and space resolution of satellite images on satellite wind vectors over the south central United States. They recommended that short-interval (6–10 min) sequences be used to track low-level clouds associated with mesoscale features. Maddox and Vonder Haar (1979) computed statistical structure and correlation functions from mesoscale satellite wind fields for nine individual satellite data sets over the central United States. They found that the correlation function often differed significantly for the u and v components and that the mesoscale wind fields were highly anisotropic with greatest structure gradients occurring approximately normal to the mean flow. Wilson and Houghton (1979) deduced horizontal divergence fields and vertical mo-

[1] Present affiliation: Department of Meteorology, Seoul National University, Seoul 151, Korea.

tion and Peslen (1980) calculated divergence fields at the cumulus cloud level from horizontal satellite wind vectors for severe storm cases. Both studies concluded that the divergence fields were consistent with developing mesoscale features of severe weather.

It is well known that satellite wind vectors include several sources of both systematic and random errors. Among them cloud-top height determination is considered an important error source. Many studies have estimated the errors of the satellite wind data sets over ocean and land areas showing the errors to range within the accuracy of the conventional wind (see Hubert and Timchalk, 1972; Suchman and Martin, 1976; Bauer, 1976; Hasler et al., 1977; Wilson and Houghton, 1979; and Peslen, 1980). Generally, these studies did not delineate quantitatively the contribution of cloud-top height uncertainty to the error.

A significant source of error that has not been examined so carefully for satellite wind information is horizontal interpolation. In most cases the utilization of velocity information requires that it first be interpolated to a regular grid-point array. This applies to numerical model initialization and to analysis for field parameters such as divergence and vorticity. The strongly nonhomogeneous spatial coverage of the raw wind-vector data and the lack of basic information about mesoscale structure make objective analysis itself an important research topic.

The ultimate goal for satellite wind studies is to identify just how this information can be used to define the overall three-dimensional mesoscale horizontal wind field. It is clear that satellite wind data are not sufficient of themselves due to, first of all, limited horizontal and vertical coverage and poor vertical resolution. The horizontal gradient information would appear to be one of the unique contributions of these data. Gradient magnitudes may have a relatively large vertical scaling for divergence and vorticity, thus offsetting vertical resolution limitation of the raw data. The utility of satellite wind information for combination with other conventional data, use in numerical models, determination of gradient quantities such as divergence and vorticity, and general quality control is fully realized only after it has been interpolated to a regular grid-point data set.

The purpose of this paper is to examine quantitative characteristics of satellite wind information relevant to its usefulness to depict mesoscale flow and gradients for a middle latitude situation. The study extends previous work by considering more detail about vertical wind-shear effects, focusing on a middle latitude environment instead of a tropical or subtropical one, and including a determination of sensitivity to objective analysis procedures. Special rawinsonde observations taken within one hour of the time when satellite winds were computed permit a detailed intercomparison including an analysis of vertical shear effects to be made.

The investigation is based on a case study of observations obtained for 20 May 1977 over the central region of the United States.

2. Basic data

a. Description

The satellite wind data used in this case study are 18 min averaged vectors obtained from SMS images of 6 min interval from 1742 to 1800 GMT 20 May 1977 in the Kansas, western Missouri and Oklahoma area. Fig. 1 shows the high resolution SMS visible image for 1742 GMT. Special rawinsonde soundings at 1800 GMT show low-level southerly wind extending into Texas, Oklahoma and Kansas in the eastern portion of a developing trough. At the middle and upper levels, there is a general diffluent southwesterly wind flow associated with a jet. The spatial horizontal resolution of the images is 2 km for the visible channel and 16 km in the infrared. The satellite wind vectors were produced by tracking low-level cumulus clouds on McIDAS (Suomi, 1975) at the University of Wisconsin. The mean diameter of these low-level cumulus clouds ranged from 1 to 10 km. The mean life span of these clouds was over 20 min and individual clouds displayed considerably uniform movement. The target clouds had top heights ranging from 900 to 700 mb.

The three individual wind vectors computed from four images by following a target cloud were tested under quality control before being averaged into a single vector. The individual wind vectors have errors due to navigation, image resolution, height determination uncertainty, nonrepresentative motions and operator subjectivity as discussed in the previously referenced studies. Such errors can cause large variations
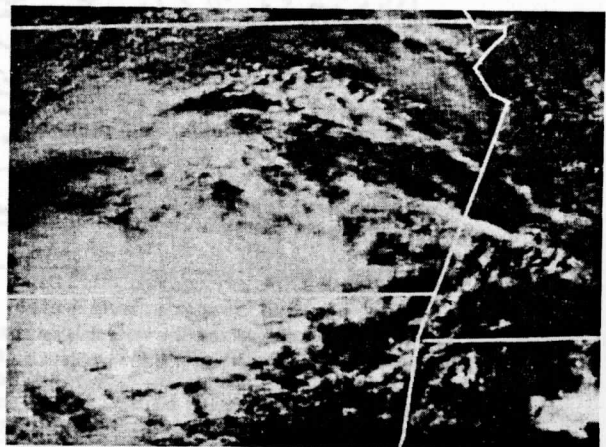

FIG. 1. High resolution visible SMS image for 1742 GMT 20 May over most of Kansas and partial regions of Missouri, Nebraska, Oklahoma and Arkansas. State boundaries are shown by white lines.

between any two consecutive vectors tracked from the images for a single cloud. In order to reduce the effects of such large variations, the three-vector series was deleted if between any two consecutive vectors either the magnitude difference of the u or v component was larger than 5 m s^{-1} or the height difference exceeded 60 mb (more than 3 K, the temperature difference at cloud-top height). This quality control eliminated many wind vectors (over 20% of the total number). Similar criteria for quality were used by Wilson and Houghton (1979) and Peslen (1980). The final 18 min averaged wind data set contained 180 vectors as shown in Fig. 2. The vectors were dense enough with respect to a 35 km grid that significant averaging occurred in the objective analysis process reducing the random error in the vector field.

b. RMS and mean differences between satellite and rawinsonde winds

Direct equivalence of satellite wind with rawinsonde wind data is not expected due to the difference of measurement character and the incompatibility in horizontal and vertical resolution as well as time-scale difference. There have been, however, a number of studies to determine the relationship of satellite wind to conventional wind data and actual atmospheric motion. Such comparisons are useful to judge aspects of the quality of the satellite wind data.

The rms vector differences between raw satellite winds and layer-averaged rawinsonde winds in the 900–700 mb layer were computed using satellite winds

within prescribed distances of the rawinsonde stations. These circular regions had radii ranging from 0.25° to 2° of latitude. The difference between the mean value of satellite winds within each circle and the center point rawinsonde wind value was also determined. For these low level data the rawinsonde balloon location is very close to the station position. The rms values and the mean differences were computed at Topeka and Monett.

The results at the two stations are shown in Fig. 3. Increasing the number of satellite winds around rawinsonde stations by enlarging the area from which satellite winds are taken tends to improve somewhat the correspondence of the satellite and rawinsonde wind information at Topeka although the rms differences increase with area for radii greater than 1° latitude. The results at Monnet were not as favorable, reflecting larger vector direction variations in the vicinity as seen in Fig. 2. Overall, there was no clear improvement in the correspondence of the two data forms with the averaging of satellite winds in data-dense areas.

Generally, the rms values and the mean differences found here range from 1 to 5 m s^{-1} for each component and are compatible to those reported in other studies. Suchman and Martin (1976) reported that the mean of the absolute value of vector difference between satellite and ship sounding winds was under 3 m s^{-1} in the area of the 1974 GARP Atlantic Tropical Experiment. Bauer (1976) also found from the synoptic-scale data over northern America that mean absolute vector differences between a satellite wind and the interpolated wind at the satellite wind position of three surrounding radiosonde winds within the 660 km radius were 4.4 m s^{-1} for the u component and 4.6 m s^{-1} for the v component while those between a given radiosonde station and the interpolated wind at the given radiosonde station of three surrounding rawinsonde stations within the same radius were 4.2 and 5.1 m s^{-1} for the u and v components, respectively. Hasler et al. (1979) showed from the results of an in situ aircraft verification experiment that trade wind regime cumulus clouds moved within 1.3, 3.5, and 7.0 m s^{-1} of the winds at cloud base, mid-cloud and cloud top, respectively. Wilson and Houghton (1979) showed that standard deviation of the error in satellite wind vectors was about 4.7 m s^{-1} and Peslen (1980) estimated that the error to be less than or equal to 3 m s^{-1} plus an undetermined error for nonrepresentative cloud motion.
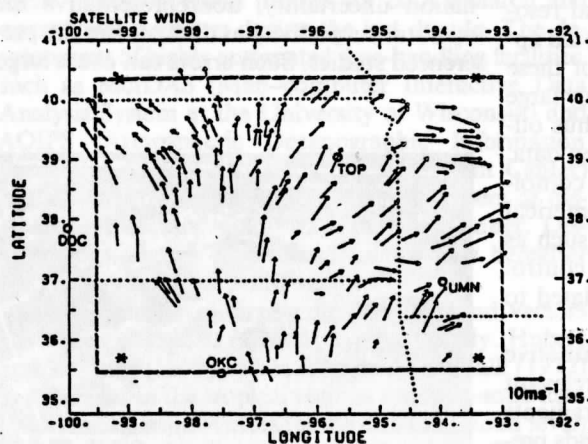

FIG. 2. Original low-level satellite wind data set obtained for the study area from 1742 to 1800 GMT SMS images. State boundaries are shown by dotted lines. The hatched rectangle and the star symbols near the corner shows the nearly identical analysis domain for the satellite data and for the analytical function study, respectively. The length of the vectors is proportional to wind speed. The scale for speed is given by the reference labeled 10 m s^{-1} vector in the lower right hand corner.

c. Variability introduced by height differences

The height of the satellite wind vectors in the present study ranged from 900 to 700 mb determined by finding the pressure corresponding to temperature of cloud-top height using 1800 GMT soundings at Topeka,
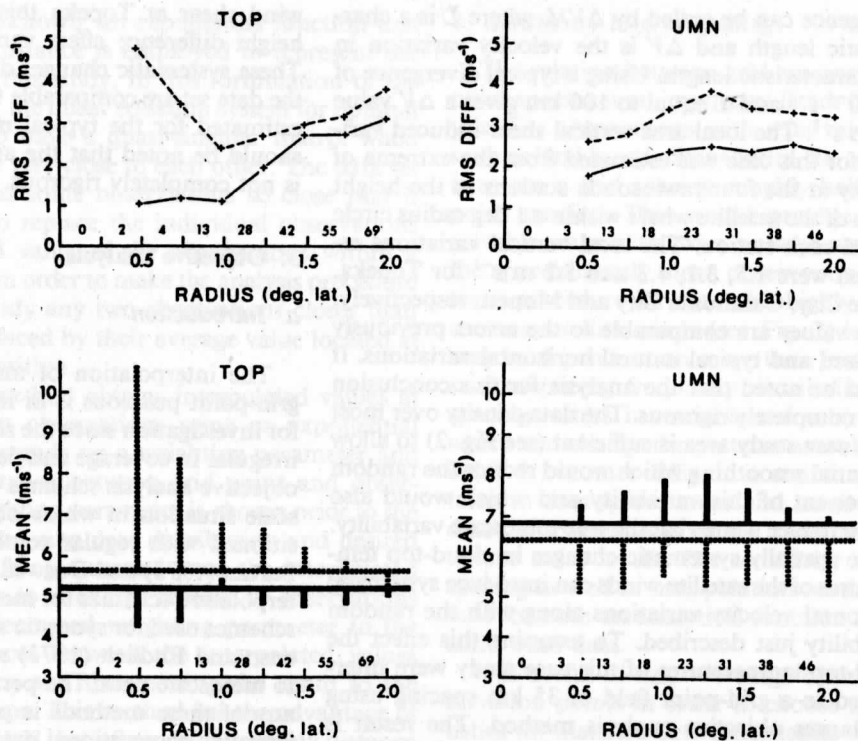
FIG. 3. Comparison of rms and mean vector differences between satellite wind and rawinsonde wind. Solid and dashed lines denote u-component and v-component values, respectively. The number of individual satellite wind vectors within the given circles are shown above the abscissa axis and just to the left of the respective radius indicator. For the mean differences the horizontal lines indicate layer-averaged rawinsonde wind and vertical lines represent the difference between the mean of satellite winds within the given circles and the rawinsonde wind.

Dodge City, Monett and Oklahoma City (see Fig. 2). This 900–700 mb layer was considered to represent the wind field at a single level in order to obtain sufficient horizontal resolution for analysis. However, this single level wind field contains an added error due to height differences in the raw data because of vertical wind shear. This effect was examined by analyzing the satellite wind vectors in relationship to vertical wind profiles at the four rawinsonde stations.

Figure 4 shows the vertical wind profiles in the layer from the surface to 500 mb at the four stations. The height range of satellite wind vectors for the entire area is indicated for each station. In the 700–900 mb layer, directional wind changes were about 30° for all stations while speed changes with height were 2 m s^{-1} for Topeka and Oklahoma City, and less than 7 m s^{-1} for Monett and Dodge City. Because of these generally weak vertical wind shears it was considered reasonable to represent the 900–700 mb layer as a single level for this study.

For this single-layer satellite wind data set, the velocity variations due to local area height differences in the layer were examined. The smaller these variations are compared to the systematic horizontal variations,

the more acceptable would be the satellite winds. The natural horizontal variations were estimated from the typical divergence value and horizontal characteristic length for mesoscale features describable by the data.
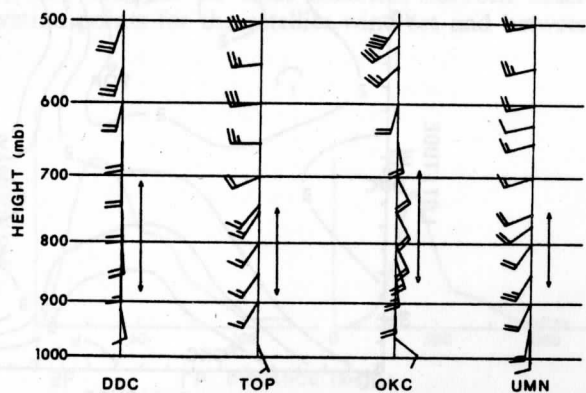

FIG. 4. The 1800 GMT wind profiles at the SESAME rawinsonde stations. The double ended arrows show the height range for the cloud-top temperatures (278 K–290 K) of the entire satellite wind data set.

Divergence can be scaled by $\Delta V/L$ where L is a characteristic length and ΔV is the velocity variation in the characteristic length. Using a typical divergence of 5×10^{-5} s^{-1} and L equal to 100 km gives a ΔV value of 5 m s^{-1}. The local area vertical shear-induced variation for this case was estimated from the extrema of velocity at the four rawinsonde stations in the height ranges of the satellite winds within a 1 deg radius circle around each station. The local vertical variations estimated were 1.5, 3.1, 4.3 and 5.2 m s^{-1} for Topeka, Dodge City, Oklahoma City and Monett, respectively. These values are comparable to the errors previously discussed and typical natural horizontal variations. It should be noted that the analysis for this conclusion is not completely rigorous. The data density over most of the case study area is sufficient (see Fig. 2) to allow for spatial smoothing which would reduce the random component of this variability and which would also tend to reduce somewhat the true mesoscale variability.

The spatially systematic changes in cloud-top temperatures of the satellite winds can introduce systematic horizontal velocity variations along with the random variability just described. To examine this effect the cloud-top temperatures of this case study were interpolated to a grid-point field of 35 km spacing using the Barnes objective analysis method. The result is shown in Fig. 5. In order to examine the velocity variation due to such systematic changes, the mean wind difference (due to height difference) between any two stations was evaluated by multiplying the mean (rawinsonde) wind shear of each station by half of the height difference and adding the results. The variations among all the stations were less than 3.5 m s^{-1}, being less than 1 m s^{-1} between Topeka and the other three stations. As shown in Fig. 5 a large temperature gradient exists to the east of Topeka. With the mean vertical

wind shear at Topeka this gradient would imply a height difference effect variation of only 1.3 m s^{-1}. These systematic changes due to height differences in the data set are comparable to the horizontal variations estimated for the typical mesoscale features. Also it should be noted that the analysis for this conclusion is not completely rigorous.

3. Objective analysis

a. Introduction

The interpolation of mesoscale satellite winds to grid-point positions is in itself an important element for investigation since the satellite wind data set is very irregular in coverage and density. There are numerous objective analysis schemes developed for the synoptic scale situation in which observation stations are positioned with regular resolution over the continent. Barnes (1973) and Doswell (1977) have developed interpolation schemes for mesoscale observations. Some schemes used for synoptic scale data, such as the Mancuso and Endlich (1973) scheme, have been applied to mesoscale data. The performance characteristics of any of these methods is poorly understood for very irregular observational data such as satellite winds. It is important to document the relative importance of interpolation errors in comparison to all the other errors mentioned above to understand the ultimate value to be anticipated from satellite wind data.

The objective analysis schemes cannot be evaluated in absolute terms for the satellite data since there is no independent verification information for mesoscale velocity fields. However, some measure of the expected interpolation error can be found by intercomparing results of analysis schemes, all starting with the same input data including analytical functions. This type of sensitivity study is the basic purpose of the section. Attention was focused on the velocity and the gradient quantities, divergence and vorticity.

b. Description of methods

Five objective analysis methods were tested on a known analytical function field and the satellite wind data set of this study. These are referred to as the Gandin (1963), Barnes (1973), Mancuso and Endlich (1973), MACC (1978) and Wahba and Wendelberger (1980) methods. Only a brief description of each method is presented.

The Gandin method incorporates a minimization procedure for root mean square error in the determination of grid-point values from observation values. In this method, the covariances characterize the statistical relation in terms of distance between observations. Since the mesoscale characteristics of the co-
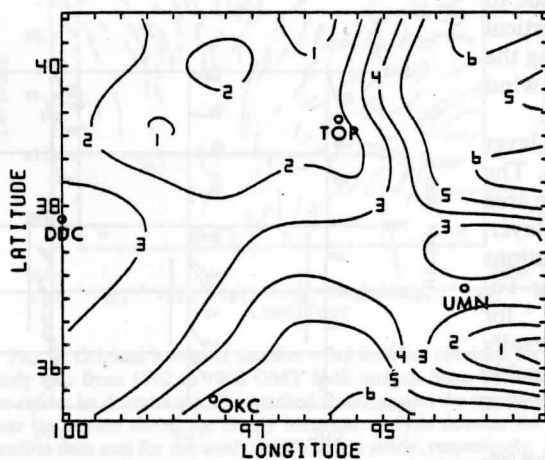

FIG. 5. Temperature contours at cloud-top heights. Value shown is amount (in K) in excess of 280 K.

variances are unknown, an exponential function that decreases with distance is employed to represent the covariances for this study. In this formulation of the Gandin method, the linear equation system for optimal weights tends to have a quasi-singular matrix when observations are very close to each other. The data set in this study has some observations so close that it was necessary to replace the individual observations by the averaged value of the observations within a certain distance in order to make the analysis procedure work. In this study any two observations closer than 35 km were replaced by their average value located at the midpoint position.

The Barnes method obtains interpolated values at grid points from observations using an exponential function that depends on a weighting parameter and the squared distance between grid point and observation. The weighting parameter is chosen prior to the analysis by considering data distribution and desired pattern scales. Using a second pass, the interpolated values are made to converge rapidly to observations by applying a decreased weighting parameter to the residual differences between the interpolated values and observations, and then adding the result to the interpolated values. This method has the advantage of being able to extend the influence of data any distance without changing the weighting function and yet still suppressing noise levels adequately.

The Mancuso and Endlich method uses a least-squares fitting of a first-degree polynomial to the nearby observations. The number of the observations is usually chosen depending on the data density and distribution. In the least-squares fitting, the observations are weighted by a decreasing function of distance between the grid point and observations giving parameter weighting to along-stream than to cross-stream data.

The MACC method is a general mathematical approximation procedure that uses a least-squares fitting of a quadratic polynomial to observations. This method includes a 25-point digital smoother to reduce noise in the interpolated grid values.

The Wahba and Wendelberger method is a variational objective analysis scheme using generalized spline fitting and a generalized cross-validation method (Wahba and Wendelberger, 1979). The method is related to Sasaki's variational approach (Sasaki, 1971) that is based on the calculus of variation in which differences between the objectively analyzed and observed values are minimized in a least-squares sense subject to meteorological dynamic constraints. Wahba and Wendelberger developed a mathematical formulation for minimizing the mean square errors between analyzed and true fields by estimating smoothing parameters from the data to be analyzed. Discretization is done at the last step rather than the first in the procedure, so this source of error does not propagate through the analysis.

c. Sensitivity to grid spacing

The relation between grid spacing and observation point spacing is an important factor for objective analysis. For observations with relatively regular spacing such as land based rawinsondes, the normal procedure is to use a grid spacing roughly half the observation point spacing. This would provide a minimum resolvable wave with twice as large wavelength scale as the approximately mean observation spacing. The optimal procedure for data with highly irregular spacing such as satellite winds (see Fig. 2) is not known and may be dependent on more than just the mean of the station-spacing frequency distribution. The variable spacing results in variable smoothing characteristics which can change the patterns as well as amplitude of fields. It becomes difficult to maintain reasonable patterns in data-sparse areas and small-scale features in data-dense areas and at the same time to uniformly reduce noise levels. The sensitivity of results to grid spacing as well as interpolation method is considered here for both an analytical function field and the satellite wind data.

It is useful to know average distance between observation points in order to choose grid spacing. Statistics for distance between satellite wind observation points in this case study were obtained as follows; the observation point nearest to a reference observation point from which distance to other observations was considered was selected from each of the four angular quadrants ($0°$–$90°$, $90°$–$180°$, $180°$–$270°$ and $270°$–$360°$) in the space about the reference point and then the distance between the each point and the reference point was computed. By considering each observation point in turn to be the reference point yielded four distances for each interior observation point. Infinite distances at the edge were not included. A similar computation was made for 78 rawinsonde stations over the continental United States. Fig. 6 shows the frequency diagram for these distances between observation points for the satellite wind set and between
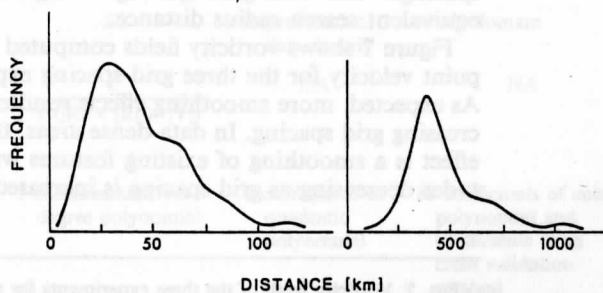

DISTANCE [km]

FIG. 6. Relative frequency distribution for distance between observation points for the satellite data set (left) and the rawinsonde stations (right) over the continental United States, except for the northern part of Maine and the southern part of Texas and Florida.

TABLE 1. Statistics for the frequency distributions of the distances between observation points for the satellite and the rawinsonde winds.

	Satellite wind	Rawinsonde wind
Observation points	180	78
Total number of data	684	285
Mode (km)	29	389
Mean (km)	44	484
Standard deviation (km)	26	257
Skewness	0.62	0.37

the rawinsonde stations. The statistics for both sample sets are shown in Table 1. It is noted that there exists much more skewness for the satellite wind than for the rawinsonde wind network.

Sensitivity of the data set to grid spacing can be examined by varying a number of parameters such as grid spacing, search distance radius and the distance weighting function from a grid point. As grid spacing increases with a fixed search distance there will eventually be a loss of information between grids (aliasing effects). If the search distance is increased with a fixed grid spacing the independence of information for each grid point diminishes reflected in increased smoothing of fields. These two effects are interrelated so the overall sensitivity can be examined by varying only one, namely grid spacing, keeping the same search distance radius and distance weighting function characteristics (relative to the grid spacing).

Based on the frequency distribution of distance between observations (see Fig. 6), it was decided to examine three different grid spacings using the Barnes analysis scheme. The 25 km grid spacing which is less than the mode and mean, 35 km grid spacing which is greater than the mode and less than the mean, and 50 km grid spacing which is larger than both the mode and mean. Since the Barnes scheme employs an exponential function for the weighting, the search distance radius is actually infinite. For all three experiments the weighting factor reaches a value half of its maximum at a distance of two grid spacings and is one percent of its maximum at a distance of four grid spacings. The four-grid spacing is regarded as an equivalent search radius distance.

Figure 7 shows vorticity fields computed from grid point velocity for the three grid-spacing experiments. As expected, more smoothing effects resulted with increasing grid spacing. In data-dense areas, the general effect is a smoothing of existing features with amplitudes decreasing as grid spacing is increased. In data-
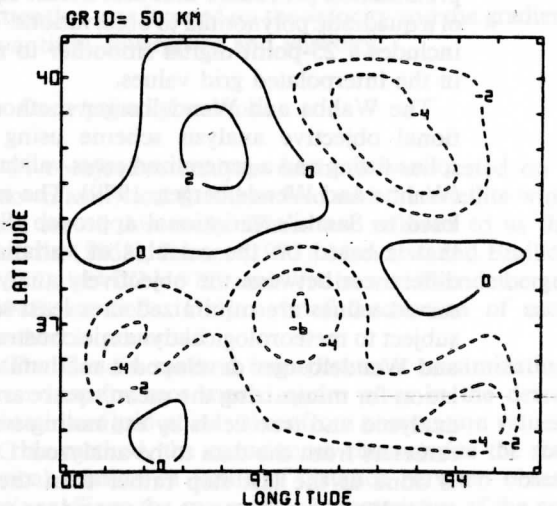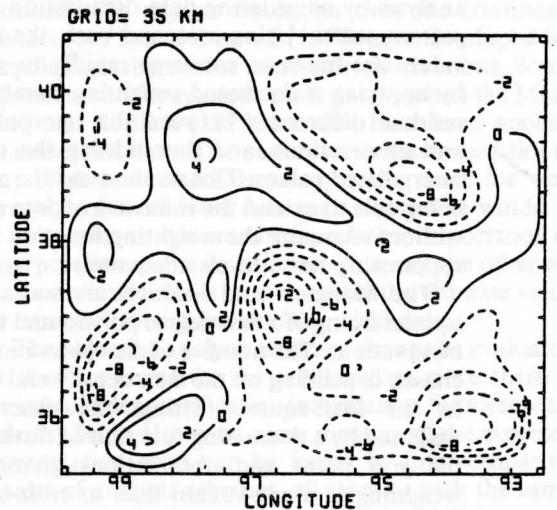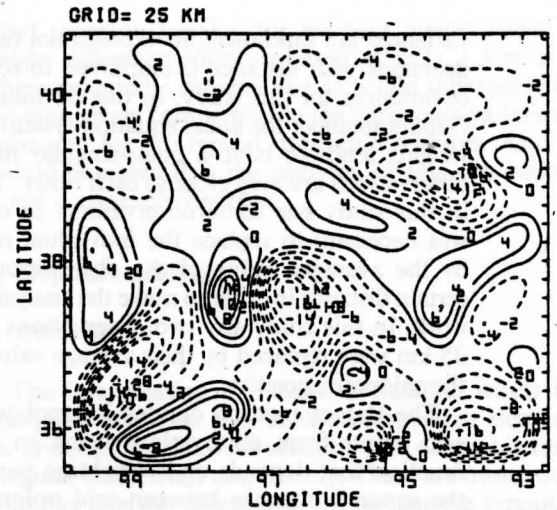

FIG. 7. Vorticity fields of the three experiments for sensitivity to grid spacing. The top, middle and lower panels show the result for the 25, 35 and 50 km grids respectively. Dashed lines are negative contours. The units are 10^{-5} s^{-1}.

sparse areas, there are more spurious effects such as rapidly increased amplitudes and the appearance of new centers as the grid spacing is decreased. Note for example the areas of 97.5°W and 37.5°N, and 95.5°W and 36.5°N. The rms magnitude of velocity difference between 25 km grid and 50 km grid was 1.5 m s^{-1}. However, locally some effects resulting from the objective analysis scheme may be greater than those due to measurement error sources. For instance, the change in vorticity values of the more extreme spurious features such as at 97.5°N and 37.5°W between the 25 km and 50 km grids for features of 100 km scale imply velocity variations up to 10 m s^{-1} which would be larger than expected from natural variability.

d. Sensitivity to objective analysis method

The five objective analysis methods were tested on a known topological form so that quantitative error characteristics of the analysis methods could be determined. A simple two-dimensional trigonometric function was defined and the functional values at the observation points of the satellite wind data were computed from the function. Then the functional values at observation points were interpolated to grid points using each objective analysis scheme. These gridded values were then compared to the original analytical values at the given grid points. Basic characteristics and parameter specification of the methods used are summarized in Table 2.

The analytical function used is

$$f(x, y) = \sum_i a_i \cos(m_i x) \cos(n_i y) \qquad (1)$$

where a_i is an amplitude, x east–west coordinate, y north–south coordinate, m_i a wavenumber in the direction of x and n_i a wavenumber in the direction of y. To simplify this function, we set $m_i = n_i$ and limit it to the first 4 harmonics ($i = 1, 2, 3$ and 4). Thus, the function $f(x, y)$ has only symmetric (circular, isometric) 16, 8, 4 and 2Δ waves for a 17 × 17 grid domain (see Fig. 2) of 35 km grid spacing (Δ), which corresponds closely to the area outlined by the dashed line in Fig. 2. The amplitudes, a_i, were 1.0, 0.3, 0.1, and 0.05 for the 16, 8, 4 and 2Δ wave lengths, respectively.

Figure 8 shows the analytical field, the results of the five methods, and the difference fields between the analytical function field and the objective analysis results. All methods resolved well the basic wave (16Δ) and clearly showed the filtering of 2Δ waves. The methods did not pick up the local extrema at the three corners missing observation points. The Gandin, Barnes, and Wahba and Wendelberger methods picked up more than 85% of the local extreme magnitude in the center of the domain. The difference fields show additional details about the objective analysis errors. The rms differences between the analytical values and the grid values analysed by the Gandin, Barnes, Mancuso and Endlich, MACC, and Wahba and Wendelberger methods were 0.16, 0.13, 0.14, 0.16 and 0.15, respectively. Because of highly spurious results, all boundary grid points and four interior grid points in the southwest corner of the domain were excluded in the computation of all the rms differences.

Objective analysis schemes normally produce spurious patterns as well as amptitude changes if obser-

TABLE 2. Comparisons of basic characteristics and parameter specifications of objective analysis methods used in this study. Symbols are defined as follows: Δ is the grid spacing, **R** is a normalized distance between grid point and data point, and C_1, C_2, and C_3 are nondimensional coefficients, and **V** is nondimensional velocity.

	Gandin	Barnes	Mancuso and Endlich	MACC	Wahba and Wendelberger
Number of observations for one grid value	8	dependent on data density	up to 8	8	all
Search radius from a grid point	dependent on data density	≈4Δ	2Δ	dependent on data density	whole domain
Distance weighting factor	$\exp(-C_1\|\mathbf{R}\|^2)$	$\exp(-C_2\|\mathbf{R}\|^2)$ for 1st pass $\exp(-0.3C_3\|\mathbf{R}\|^2)$ for 2nd pass	$\dfrac{1}{1 + (\|\mathbf{R}\| + \|\mathbf{R}\| \times \|\mathbf{V}\|)^2}$	NA	NA
Mathematical basis	weighted average	weighted average	3 coefficients of 1st-degree polynomial	6 coefficients of quadratic polynomial	10 coefficients of cubic polynomial and coefficients from cross validation method
Additional smoothing	averaging for close data points within 1Δ	no	no	25-point digital filter	no

ANALYTICAL FUNCTION FIELD   GANDIN   BARNES

MANCUSO AND ENDLICH   MACC   WAHBA AND WENDELBERGER

DIFFERENCE FIELD

A   B

C   D   E
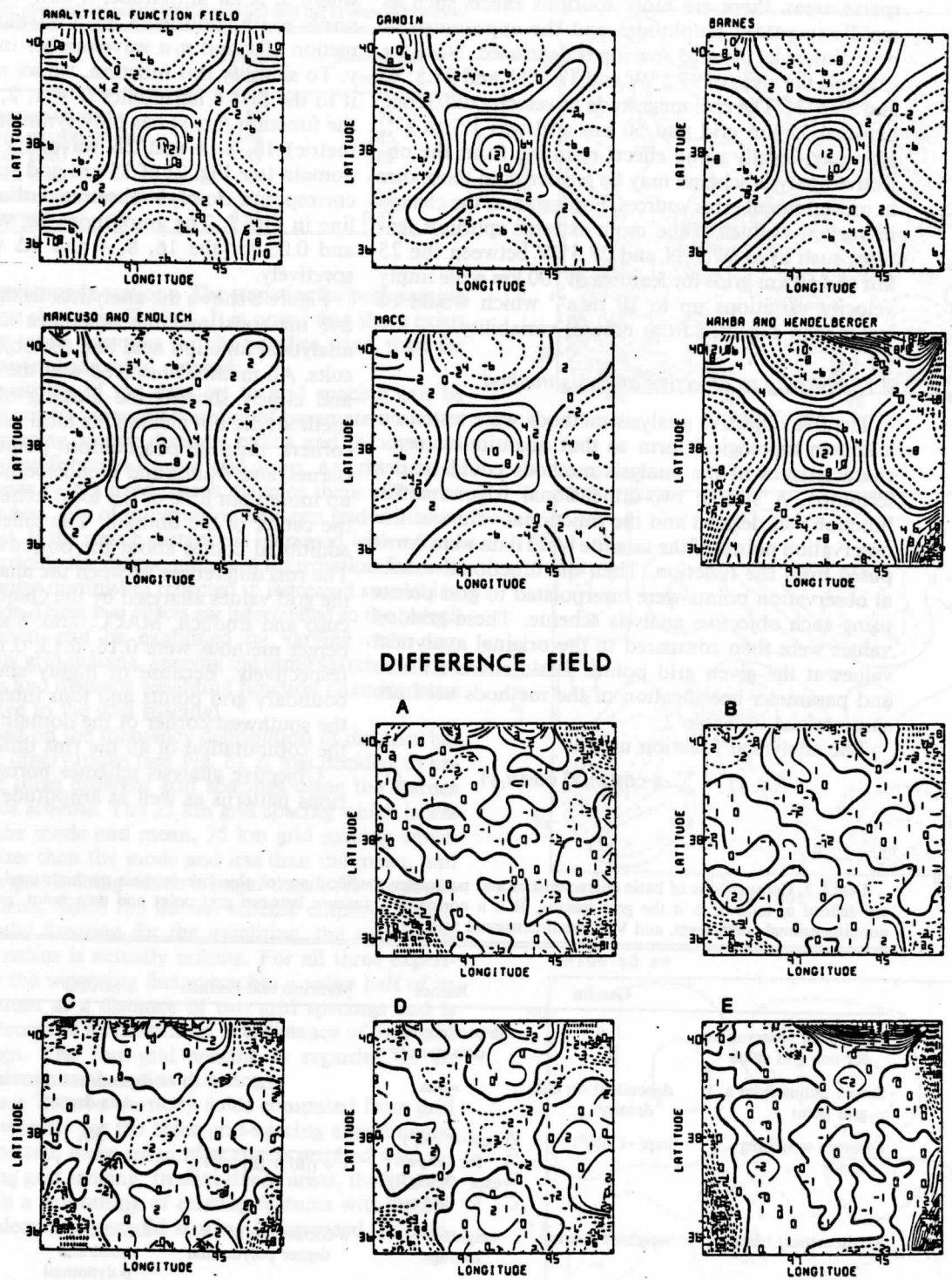
FIG. 8. The analytical function field and the results determined by the five objective analyses methods. The fields are shown in the upper half. The difference fields between the analytical function field and the Gandin, the Barnes, the Mancuso and Endlich, the MACC and the Wahba and Wendelberger method results are shown in panels A, B, C, D and E respectively. All units are nondimensional.

vation points are irregularly scattered. These effects can be examined by applying harmonic analysis to the grid fields and comparing harmonic amplitudes to those of the analytical function. Table 3 shows the selected harmonic amplitudes for the double Fourier cosine series. The objective analysis schemes produced asymmetric wave components ($m_i \neq n_i$) that were not included in the analytical form. All methods resolved more than 70% of the basic wave (16Δ), especially 96% in the Wahba and Wendelberger method and 85% in the Barnes method, while only the Gandin and Wahba and Wendelberger methods resolved more than 70% of 8Δ wave (in fact over 100% in the Wahba and Wendelberger method). The high percentage in the Wahba and Wendelberger method and the low percentage in the Mancuso and Endlich method reflect the spurious effect in the edge of the domain. In all methods, asymmetric waves with minimum dimensions of 4Δ and 2Δ showed greater amplitudes (with only one exception) than those of the corresponding symmetric wave with dimensions of 4Δ and 2Δ while for 16Δ and 8Δ the symmetric wave amplitudes were

greater than the corresponding asymmetric wave amplitudes. This type of aliasing arises mainly from the irregular data point spacing.

The five objective analysis methods were tested on the satellite wind data set to determine grid point winds on the 35 km grid mesh in the domain outlined by the dashed line in Fig. 2. Parameter specifications of the methods were the same as used for the analytical function test.

Figure 9 and 10 show velocity fields analyzed by the methods and difference fields, respectively. In each difference field, the Barnes method result has been subtracted from the other methods. General gradient patterns were similar among the methods but there were various details in small-scale patterns. In particular, in the data-sparse area around 37.5°N, 97.5°W, there were spurious features in u component for the Mancuso and Endlich, and Wahba and Wendelberger methods. In the v component for the Gandin methods, there were many detail patterns whose amplitudes were not larger than those of other methods, while in the Wahba and Wendelberger method there were large-scale patterns whose amplitudes were larger than those of other methods. All methods showed large differences in the southern half of the domain in association with data-sparse areas and nonuniform data regions. Except near the edges, difference magnitudes for both the u and v components range from 0 to 5 m s^{-1} (Fig. 9). The rms differences of velocity between the Barnes results and the Gandin, the Mancuso and Endlich, the MACC, and the Wahba and Wendelberger results were 1.22, 1.13, 1.04, and 1.31 m s^{-1} for u component, respectively, and 1.75, 1.31, 1.33 and 1.90 m s^{-1} for v component, respectively. These values, computed in the area excluding boundary area grid points where edge effects were large, are comparable to the typical horizontal velocity variations of 100 km scale previously discussed.

The gradient fields of the grid-point winds produced by the methods, vorticity and divergence, were computed. All methods showed generally similar phase relationships of both parameters. Typical amplitudes were 5×10^{-5} s^{-1} with the rms amplitudes ranging from 3.65 to 5.58 ($\times 10^{-5}$) s^{-1} for both parameters. At the synoptic scale, vorticity is an order of magnitude greater than divergence. In these mesoscale wind data, both parameters are the same order of magnitude which is typical of the mesoscale. In the Barnes, Mancuso and Endlich, MACC and Wahba and Wendelberger methods, 200 to 300 km (6Δ to 8Δ) wavelengths were dominant, while in the Gandin method 150 km (4Δ) wavelengths seemed to be more dominant where Δ is the grid spacing of 35 km. All methods yielded strong signal in the mesoscale range.

There existed many similar characteristics between divergence and vorticity results for each method and thus a detailed discussion of the sensitivity results is

TABLE 3. Harmonic component amplitudes of a two-dimensional scalar field for the prescribed analytical function and results from five objective analysis methods. The x and y wavelengths of the components are identified by labels for the columns and blocks of rows respectively.

| Analytical function	$16\Delta x$	$8\Delta x$	$4\Delta x$	$2\Delta x$
$16\Delta y$	1.0	0	0	0
Gandin	0.7710	0.1587	0.0379	0.0059
Barnes	0.8642	0.0945	0.0219	0.0077
Mancuso and Endlich	0.7328	0.1074	0.0426	0.0120
MACC	0.7327	0.0949	0.0198	0.0084
Wahba and Wendelberger	0.9691	0.0977	0.0804	0.0256
$8\Delta y$	0	0.3	0	0
Gandin	0.1550	0.2291	0.0377	0.0131
Barnes	0.0746	0.1944	0.0198	0.0086
Mancuso and Endlich	0.0948	0.1601	0.0325	0.0131
MACC	0.0743	0.1534	0.0219	0.0083
Wahba and Wendelberger	0.1003	0.3088	0.0760	0.0400
$4\Delta y$	0	0	0.1	0
Gandin	0.0323	0.0384	0.0193	0.0081
Barnes	0.0239	0.0223	0.0167	0.0017
Mancuso and Endlich	0.0397	0.0403	0.0170	0.0187
MACC	0.0175	0.0261	0.0124	0.0083
Wahba and Wendelberger	0.0765	0.0215	0.0638	0.0185
$2\Delta y$	0	0	0	0.05
Gandin	0.0161	0.0119	0.0086	0.0017
Barnes	0.0030	0.0023	0.0012	0.0003
Mancuso and Endlich	0.0364	0.0090	0.0116	0.0063
MACC	0.0097	0.0053	0.0060	0.0001
Wahba and Wendelberger	0.0232	0.0117	0.0018	0.0033
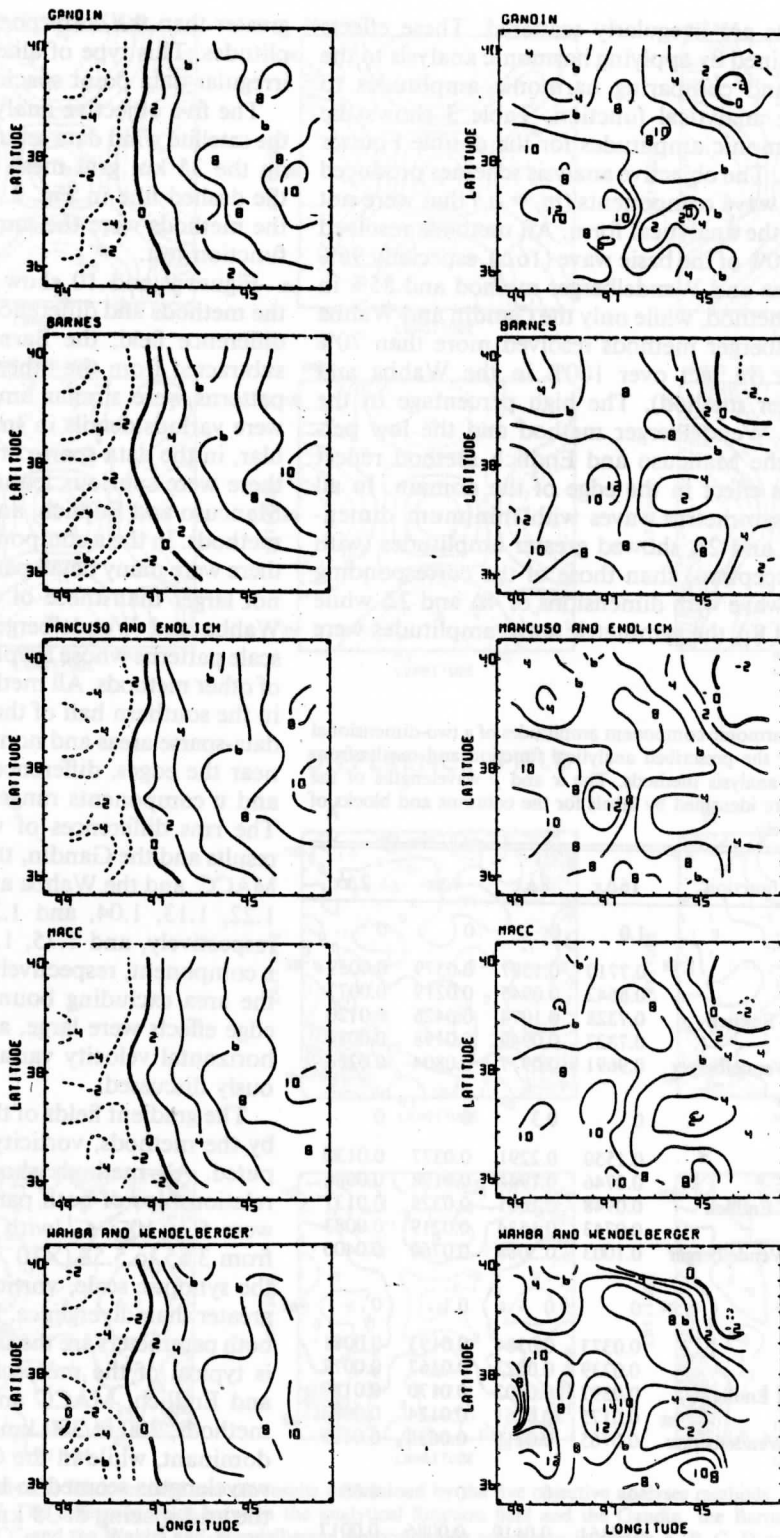
FIG. 9. Velocity components determined by the Gandin, Barnes, Mancuso and Endlich, MACC and Wahba and Wendelberger methods as labeled. The units are m s^{-1}. Contours are omitted in the area of the exceptionally spurious effects.
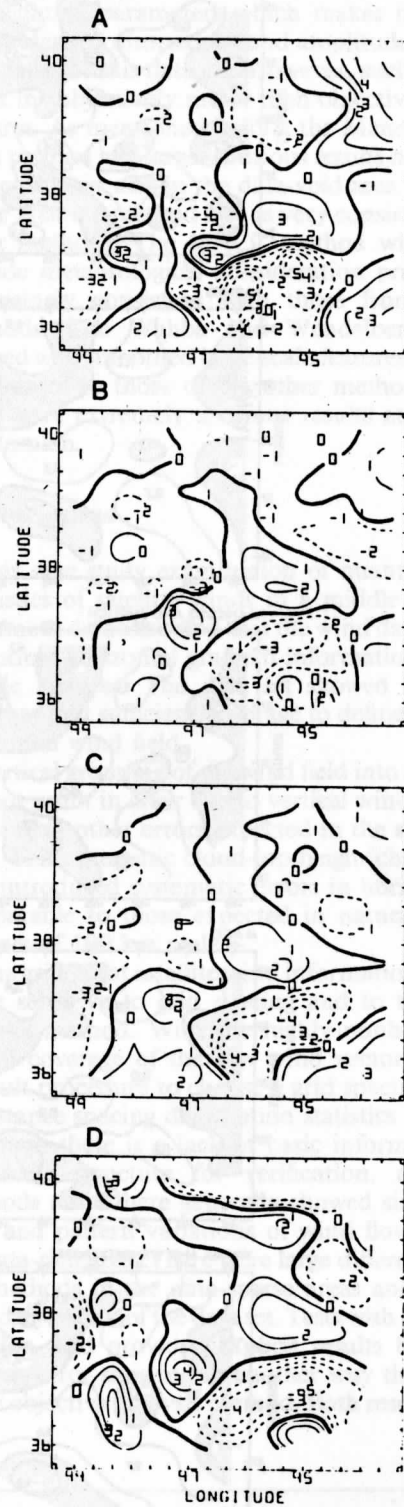
U COMPONENT
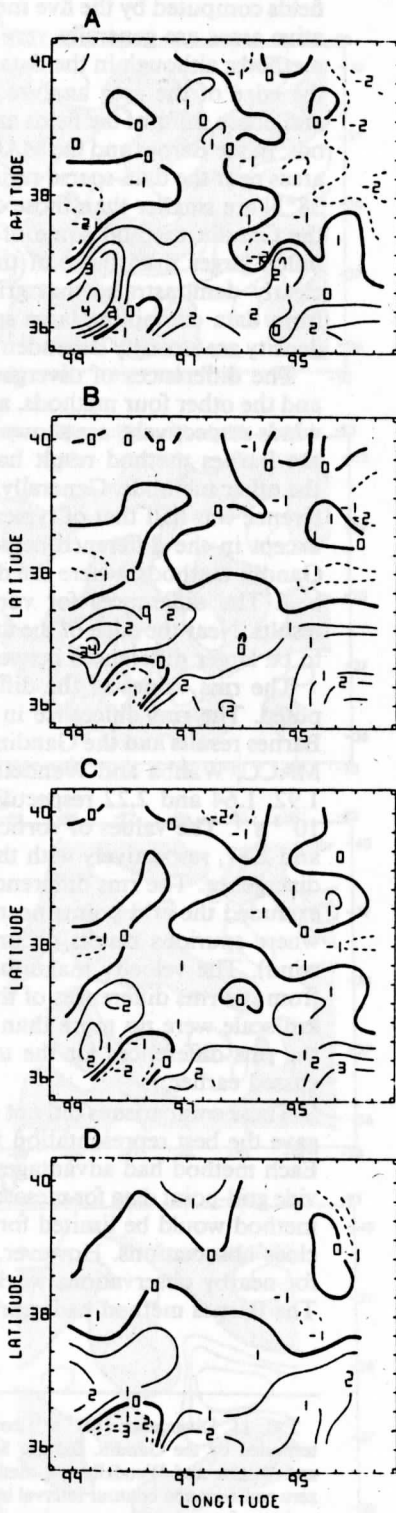
V COMPONENT

FIG. 10. Difference fields in velocity components between the Barnes method results and the Gandin, the Mancuso and Endlich, the MACC, and the Wahba and Wendelberger method results in panels A, B, C and D respectively. In each case the Barnes values are subtracted from the other values. The units are m s⁻¹. Contours are omitted in the area of exceptionally spurious effects.
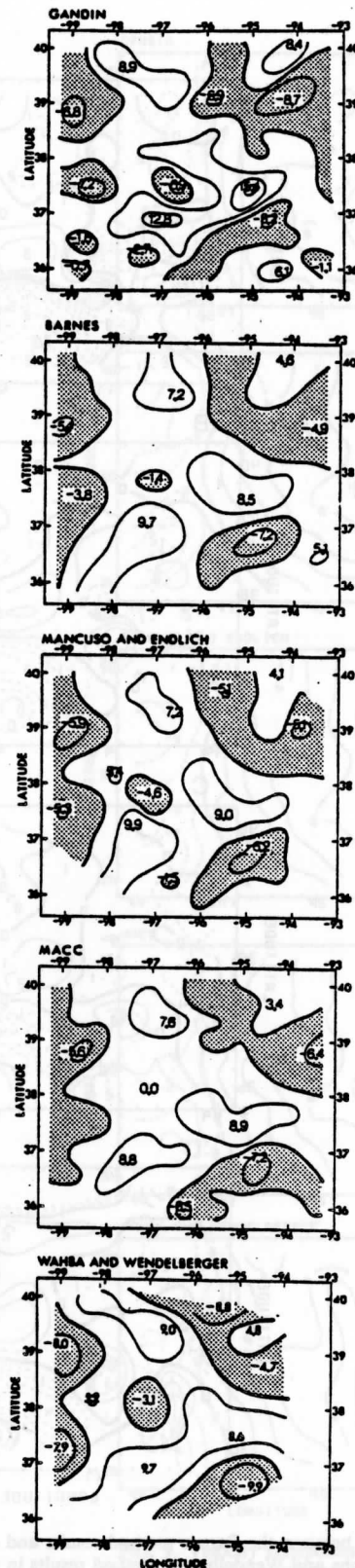
given only for divergence. Fig. 11 shows divergence fields computed by the five methods. Positive and negative areas are generally very comparable among the methods; although in the data-sparse regions and near the edge of the area analyzed, amplitude differences and phase shifts of the fields existed between the methods. In the Barnes and the MACC methods the negative areas near the data-sparse region at roughly 97°W and 38°N are smaller than those of the other methods. In the Gandin method some of the local extrema were much larger than those of the others methods. This clearly demonstrates that grid point fields obtained from data containing large spatial variations in data density are strongly dependent upon the method used.

The differences of divergence between the Barnes and the other four methods, as done for the grid-point winds respectively, are shown in Fig. 12. In each case, the Barnes method result has been subtracted from the other methods. Generally, the typical value of difference was half that of typical divergence magnitude except in the difference between the Barnes and the Gandin methods, where the difference was more than half. The differences for vorticity showed the same results. Near the edge of the analysis area there tended to be larger differences between the results.

The rms values of the difference fields were computed. The rms difference in divergence between the Barnes results and the Gandin, Mancuso and Endlich, MACC, Wahba and Wendelberger results were 2.87, 1.92, 1.64 and 2.22 respectively, where the units are 10^{-5} s^{-1}. The values of vorticity were 2.97, 1.79, 1.83 and 2.87, respectively with the same units as those of divergence. The rms difference values for all methods excluded the grid points near the edge of the domain where spurious results occurred (same points as for wind). The velocity magnitude differences estimated from the rms differences of the divergence for the 100 km scale were no more than 3 m s^{-1} consistent with the rms differences for the u and v components discussed earlier.

These comparisons did not determine which method gave the best representation for the observation data. Each method had advantages and weaknesses to provide grid-point data for mesoscale features. The Gandin method would be limited for mesoscale analysis with close observations. However, an averaging technique for nearby observations worked out for this method. The Barnes method had more flexibility in the choice

FIG. 11. Divergence (10^{-5} s^{-1}) computed from gridded data determined by the Gandin, Barnes, Mancuso and Endlich, MACC, and Wahba and Wendelberger methods. The thick solid lines are zero contours and contour interval is 5×10^{-5} s^{-1}. Shading indicates regions of negative divergence (convergence). The numbers indicate the position and value of local extrema. Contours are omitted in the area of the exceptionally spurious effects.
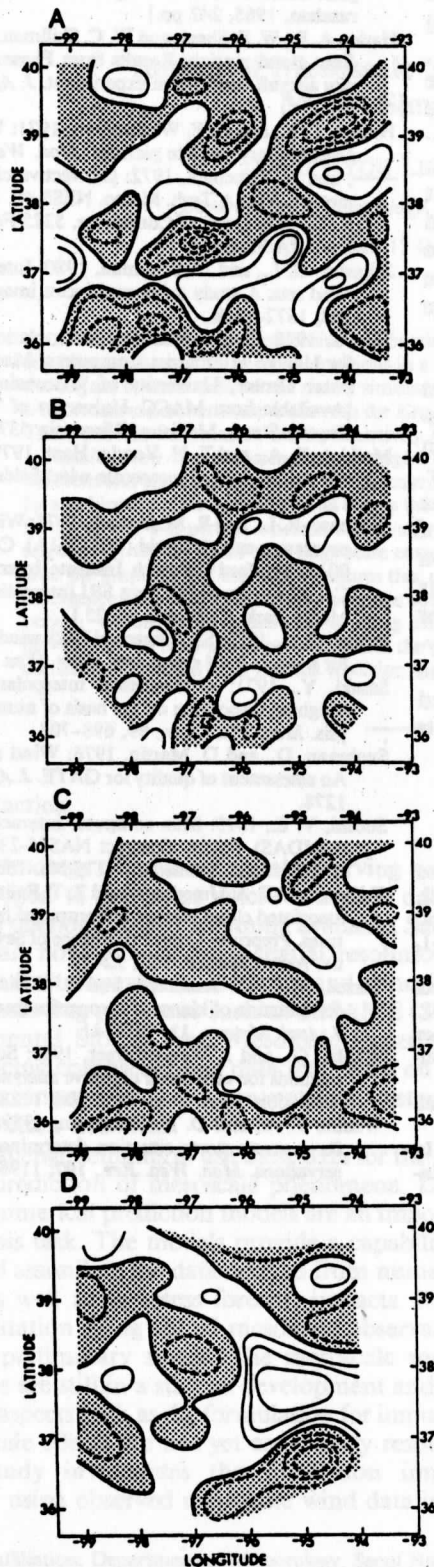
of weighting parameters which makes it possible to obtain desired dimensions and amplitudes of features especially for this data set. However, such ability may result in subjectively rather than objectively analyzed features. As mentioned before, the Mancuso and Endlich method had larger spurious results near the edges of the domain and in the data-void area. In the data-dense area the method also is very consistent with the other methods. The MACC method which did not include meteorological consideration provided fields surprisingly consistent with those from the other methods. The Wahba and Wendelberger method showed well smoothed large-scale features with similar amplitudes to those of the other methods, although there were extremely spurious results at the edge of the domain.

4. Conclusions

This case study examination of quantitative characteristics of satellite winds in a middle latitude environment demonstrated that the wind data could provide some horizontal gradient information in the mesoscale features. The data set showed considerable accuracy and sufficient coverage to define a mesoscale horizontal wind field.

Vertical grouping of the wind field into a single level did not result in error due to vertical wind-shear effect larger than other errors expected in the satellite wind data. The systematic cloud-top height changes in this case introduced systematic errors in horizontal shear comparable to those expected in natural mesoscale features of 100 km scale.

The grid point satellite wind information was shown to be sensitive to grid spacing and to the objective analysis method. With the highly nonhomogeneous spatial coverage of the raw wind vector data it is a difficult procedure to choose a grid spacing according to distance spacing distribution statistics for the data. Although there is a lack of basic information about mesoscale structure for verification, all objective methods tested here generally showed similar amplitude and pattern variations of wind flow features in the data-rich area. There were large differences among the methods in the data-sparse areas and the lateral boundary region of the data set. Tests with an analytical function field provided explicit results for objective analysis error showing in another way the sensitivity to the objective analysis method. Both resolution error

panels A, B, C and D respectively. In each case the Barnes values are subtracted from the other values. The thick solid lines are zero contours; the thin solid lines are positive value contours; and the thin dashed lines are negative value contours. Shading indicates regions of negative value. Contour interval is 2.5×10^{-5} s^{-1}. Contours are omitted in the area of exceptionally spurious edge effects.

FIG. 12. Difference fields in divergence (10^{-5} s^{-1}) between the Barnes method results and the Gandin, the Mancuso and Endlich, the MACC and the Wahba and Wendelberger method results in

and errors between the methods due to objective analysis effects are comparable to those expected in natural mesoscale features of 100 km scale.

Further case studies are necessary to identify more general characteristics of midlatitude satellite winds and, in addition, to specify objective analysis procedures for the combination of independent data types. Of critical importance is obtaining an independent verification from observations for the satellite wind mesoscale fields. The rawinsonde data used here were too few and far between to make any estimates of the actual signal-to-noise ratio or systematic error of the mesoscale cloud wind vectors.

REFERENCES

Barnes, S. L., 1973: Mesoscale objective map analysis using weighted time-series observations. NOAA Tech. Memo. ERL NSSL-62, Norman, Oklahoma, 60 pp. [Available from NTIS, U.S. Dept. of Commerce, 5285 Fort Royal Rd., Springfield, VA 22161, Identification No. COM-73-10781.]

Bauer, K. G., 1976: A comparison of cloud motion winds with coinciding radiosonde winds. *Mon. Wea. Rev.*, 104, 922–931.

Doswell, C. A., 1977: Obtaining meteorologically significant surface divergence fields through the filtering property of objective analysis. *Mon. Wea. Rev.*, 105, 885–892.

Fujita, T. T., E. W. Pearl and W. E. Shenk, 1975: Satellite-tracked cumulus velocities. *J. Appl. Meteor.*, 14, 407–413.

Gandin, L. S., 1963: *Objective Analysis of Meteorological Fields.* In Russian, Gidrometeorol. Izdatelstvo (GIMIZ), Leningrad. [English translation, Israel Program for Scientific Translations, Jerusalem, 1965, 242 pp.]

Hasler, A. E., W. E. Shenk and W. C. Skillman, 1977: Wind estimates from cloud motion: Results from Phases I, II and III of an *in situ* aircraft verification experiment. *J. Appl. Meteor.*, 16, 812–815.

Hubert, L. F., and L. F. Whitney, Jr., 1971: Wind estimation from geostationary satellite pictures. *Mon. Wea. Rev.*, 99, 665–672.

——, and A. Timchalk, 1972: Convective clouds as tracers of air motion. NOAA Tech. Memo. NESS-40, 12 pp. [Available from NTIS, U.S. Dept. of Commerce, 5285 Fort Royal Rd., Springfield, VA 22161.]

Johnson, G. L., and D. Schuman, 1980: Intercomparisons of SMS wind sets: A study using rapid-scan imagery. *Mon. Wea. Rev.*, 108, 1672–1688.

MACC, 1978: Two-dimensional interpolation. Reference Manual for Univac 1100 Series Computers. Madison Academic Computer Center, University of Wisconsin, Madison, 5–11 pp. [Available from MACC, University of Wisconsin, 1210 West Dayton Street, Madison, Wisconsin 53706.]

Maddox, R. A., and T. H. Vonder Haar, 1979: Covariance analyses of satellite-derived mesoscale wind fields. *J. Appl. Meteor.*, 18, 1327–1334.

Mancuso, R. L., and R. M. Endlich, 1973: Wind editing and analysis program—spherical grid (WEAP-1A). Contract Dahc 04-71-C-0013, Stanford Research Institute International, Menlo Park, CA, 59 pp. [Available from SRI International, 333 Ravenswood, Menlo Park, California 94025.]

Peslen, C. A., 1980: Short-interval SMS wind vector determinations for a severe local storm area. *Mon. Wea. Rev.*, 108, 1407–1418.

Sasaki, Y., 1971: A theoretical interpolation of anisotropically weighted smoothing on the basis of numerical variational analysis. *Mon. Wea. Rev.*, 99, 698–708.

Suchman, D., and D. Martin, 1976: Wind sets from SMS images: An assessment of quality for GATE. *J. Appl. Meteor.*, 15, 1265–1278.

Suomi, V. E., 1975: Man computer interactive data access system (McIDAS). NASA Contract NAS55-23296, SSEC, University of Wisconsin, Madison, [NTIS No. 75N28733].

Tecson, J. J., T. A. Umenhofer and T. T. Fujita, 1977: Thunderstorm-associated cloud motion as computed from 5-minute SMS pictures. Preprints Tenth Conference of Severe Local Storms, Seattle, Amer. Meteor. Soc., 22–29.

Viezee, W., S. M. Serebreney and R. L. Mancuso, 1972: A sample computation of kinematic properties from cloud motion vectors. *J. Appl. Meteor.*, 11, 731–741.

Wahba, G., and J. Wendelberger, 1980: Some new mathematical methods for variational objective analysis using splines and cross validation. *Mon. Wea. Rev.*, 108, 1122–1143.

Wilson, T. A., and D. D. Houghton, 1979: Mesoscale wind fields for a severe storm situation determined from SMS cloud observations. *Mon. Wea. Rev.*, 107, 1198–1209.

Impact of Mesoscale Satellite Wind Data on Numerical Model Simulations: A Case Study

DONG KYOU LEE[1] AND DAVID D. HOUGHTON

Department of Meteorology, University of Wisconsin, Madison, WI 53706

(Manuscript received 13 October 1982, in final form 30 January 1984)

ABSTRACT

Initialization of a comprehensive mesoscale numerical prediction model is investigated using actual low-level mesoscale satellite wind observations in a case study. Attention is focused on describing and understanding the impact of these data on the model simulation with basic dynamical variables as well as precipitation. Three 6-h forecast experiments are made with the Kreitzberg–Perkey mesoscale model with 35 km horizontal resolution. These provide information on the sensitivity of the results to the method of data insertion.

Results show that the mesoscale divergence and vorticity fields in the satellite wind information remain coherent and identifiable well into the forecast period. Examination of the fields for specific scale ranges obtained by an objective scale decomposition shows that both the small- and large-scale components for vorticity persist for the entire 6 h period, whereas the divergence patterns of the inserted data are dissipated by 0.5 and 3 h respectively for the small- and large-scale components. After 3 h the primary impact of the inserted data is to alter the amplitude of mesoscale features that develop in the control experiment particularly for the horizontal divergence field. The satellite data produce some noticeable changes in the precipitation forecast in the 1–3 h period. Variations in results due to using different insertion procedures are small compared to differences between all the insertion experiments and the control except for a rather large amplitude external gravity wave oscillation produced by a gradual insertion technique.

1. Introduction

The technology of meteorological observing systems has developed to the point where extensive data for mesoscale phenomena are becoming available. Satellite sensing can now provide high spatial resolution information for temperature, moisture and wind fields. Special observing programs such as SESAME (Severe Environmental Storms And Mesoscale Experiment) are producing comprehensive data sets based on both remote sensing systems and conventional systems in high resolution networks.

The challenge remains to use these data for the analysis and prediction of mesoscale phenomena. Deterministic numerical prediction models are an important tool for this task. The models provide a capability to merge and assimilate the data derived from numerous sources as well as to assess forecast impacts. Model experimentation using actual mesoscale observations is in the preliminary stages. The mesoscale models themselves are still in a state of development and fundamental aspects such as the formulation for important subgrid scale effects are not yet completely resolved.

This study investigates the simulation impacts caused by using observed mesoscale wind data in the

initialization of a comprehensive mesoscale numerical model. The analysis goes beyond previous studies (e.g., Tarbell *et al.*, 1981; Anthes *et al.*, 1981) by considering a broader range of diagnostics. Important dynamical variables such as pressure, divergence, and vorticity are examined as well as precipitation. A comparative set of model simulations plus the use of fields filtered according to a horizontal scale clarifies basic adjustment processes resulting from the initialization. Sensitivity to the initialization procedure is evaluated by comparing two different initialization methods.

Mesoscale model initialization embodies problems associated with both the observations themselves and the dynamics for this scale of motion. Interpolation of data information to the grid-point positions in the model is a critical and nontrivial task for the data sets which are frequently limited and nonhomogeneous in coverage. The insertion of the actual data can cause undesirable solutions due to erroneous data and lack of compatibility between different variables. It is important to consider appropriate initial adjustments relevant to the dynamics of the numerical model employed.

For large-scale numerical models initial adjustments are often made to suppress the imbalance between mass and wind fields which produces large amplitude gravity-inertial wave oscillations. A number of studies have achieved a satisfactory balanced state between

---

[1] Present affiliation: Department of Meteorology, Seoul National University, Seoul 151, Korea.

the mass and motion fields in the initial condition for large-scale primitive equation models (Bengtsson, 1975; Haltiner and Williams 1980). For mesoscale numerical models it is not appropriate to remove all small-scale and/or fast-moving systems such as gravity wave modes in the procedure of initialization. Geostrophic imbalance contained in the initial data should be appropriately incorporated into the mesoscale numerical models since the dynamics of real atmospheric small-scale features may be significantly unbalanced. In recent years several initialization experiments have been performed with actual mesoscale data for small-scale numerical prediction models. In many cases the initialization techniques were similar to methods of dynamical initialization developed for large-scale phenomena (Rao and Fishman, 1975; McFarland and Sasaki 1977). Rao and Fishman used mesoscale information observed in the National Severe Storm Laboratory (NSSL) network to test a dynamical initialization technique in a mesoscale primitive equation model but did not consider a broad range of diagnostics for the model simulations. A new technique of dynamical initialization known as the "nudging method" has been developed by Hoke and Anthes (1976, 1977) for mesoscale numerical prediction models. They studied mesoscale assimilation of conventional synoptic observations in a mesoscale numerical model using this dynamical technique.

Up to now, sophisticated initialization methods have not been tried on general mesoscale data fields. The level, characteristics and acceptability of noise that will be generated remains an important topic of research. A first step to developing acceptable initialization methods for this situation is to understand the impact of real mesoscale observations on the model simulation in the absence of elaborate assimilation procedures. At this point, controlling the vertically integrated mass divergence of initial wind fields is considered to be the minimal preforecast adjustment. The study does include tests with more sophisticated approaches, but the emphasis remains on examining the data impact rather than the initialization method or improvement in forecast.

This study focuses on the wind data derivable from satellite observations. Subsynoptic fields for moisture and temperature have also been derived from satellite observations, but there are vastly different problems associated with each of these variables which could complicate understanding a general impact study without preliminary impact studies with each variable individually. The wind data available from cloud displacement analysis offer basic mesoscale dynamic information for numerical models and captures phenomena with smaller scales than either satellite moisture or temperature data. Nevertheless, satellite wind data are generally incomplete in coverage and subject to large error so that for comprehensive mesoscale initialization they will serve only in a supplementary role. Furthermore, adjustment theory suggests that for the smaller scales, the wind data should be an important (or dominant) contributor to the resulting simulation; although, strictly speaking, this has been shown only for the quasi-steady or quasi-geostrophic flow component.

The data used for this study are low-level mesoscale satellite wind vectors with average spacing of 30 km, obtained from high resolution SMS images, and hourly surface winds. Many such mesoscale satellite wind data sets have recently become available along with some assessment for quality (Suchman and Martin, 1976; Hasler et al., 1977; Wilson and Houghton, 1979; Peslen, 1980). Additional judgements on quality await further compatibility tests that numerical model experimentation will provide. The investigation here is limited to a single case study.

2. Synoptic situation and mesoscale data for the case study

The atmospheric situation in the south central region of the United States from 1800 GMT 20 May to 0000 GMT 21 May 1977 was the basis for this case study. Fig. 1 shows the surface fronts, isobars and precipitation at the beginning and end of the period. During this time numerous convective systems existed in the eastern portion of a developing trough moving into the area. At 1800 GMT low-level southerly wind extended into Texas, Oklahoma and Kansas. A broad area of moisture had already been drawn in by these southerly winds below 700 mb. At the middle and upper levels, there was a general diffluent southwesterly wind flow associated with a jet approaching from the southwest. A major band of thunderstorms was already developing in the northwestern part of Texas. By 0000 GMT 21 May the low-level southerly flow had increased in speed and the moist layer had deepened. The jet core was now centered in the area studied and a trough was developing at middle tropospheric levels. Bands of active convective thunderstorms existed in the Oklahoma and northern Texas area.

The mesoscale wind data for this case were 18 min averaged low-level wind vectors for the period from 1742 to 1800 GMT on 20 May obtained in the Kansas, Oklahoma, western Missouri and north central Texas area using 6 min interval data. Fig. 2 shows the high resolution SMS visible image at 1742 GMT and the region where wind vectors were processed. The data set (Fig. 3) was produced on the McIDAS (Man-computer Interactive Data Analysis System) developed by the Space Science and Engineering Center at the University of Wisconsin (Suomi, 1975). The wind vectors were obtained from low-level cumulus clouds with diameters from 1 to 10 km and top heights ranging from 700 to 900 mb. Poor coverage of data over some areas resulted from the lack of cloud elements or from extensive high anvil cirrus cover.

18 GMT 20 MAY 1977
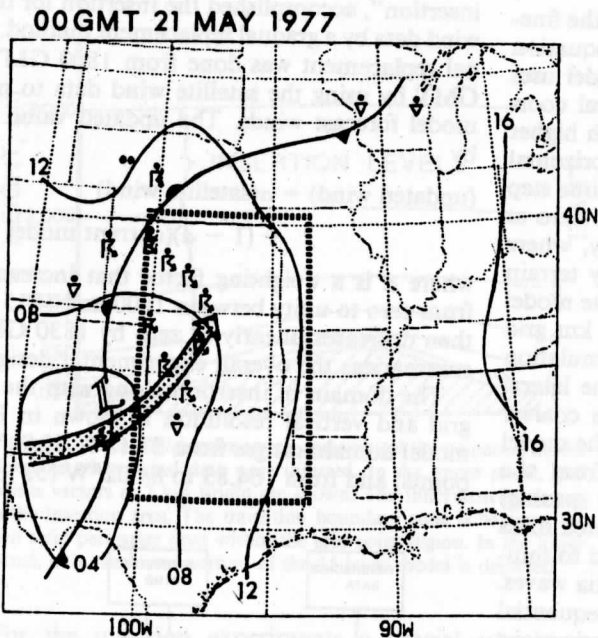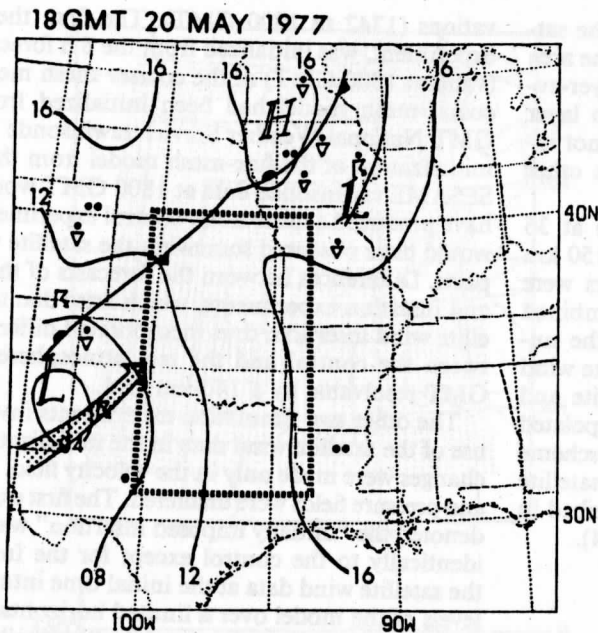

00 GMT 21 MAY 1977

FIG. 1. Surface fronts, isobars, positions of the 500 mb jet (shaded arrows), and precipitation reports for the initial and final times of the case study. The dashed lines indicate the area within which the satellite wind data were obtained.

Special upper air sounding data from the "regional scale" domain of SESAME were available at 17 stations with average horizontal resolution of about 350 km for 1800 GMT 20 May over the south central United States which allowed for some general quality assessment of the satellite wind vectors. The "storm-scale" domain of SESAME over central Oklahoma was west
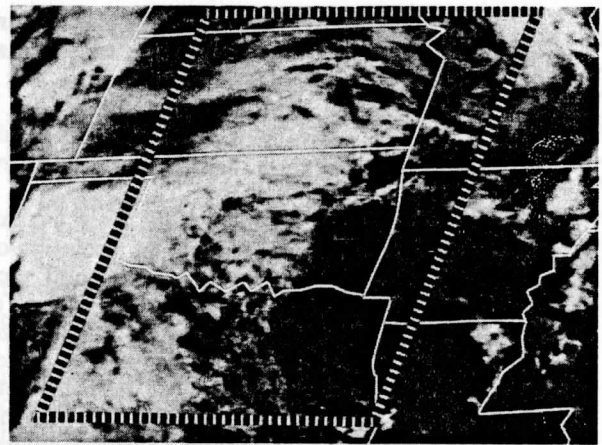

FIG. 2. High resolution visible SMS image for 1742 GMT 20 May 1977 over eastern Colorado, Kansas, Missouri, Oklahoma, Arkansas, northern Texas and Louisiana. The dashed lines indicate the area within which the satellite wind data were obtained.

of the area where satisfactory satellite wind data sets were obtained precluding a direct verification of the mesoscale features themselves. The low-level vertical wind shear was examined from the rawinsonde soundings at four stations (Topeka, Monett, Oklahoma City
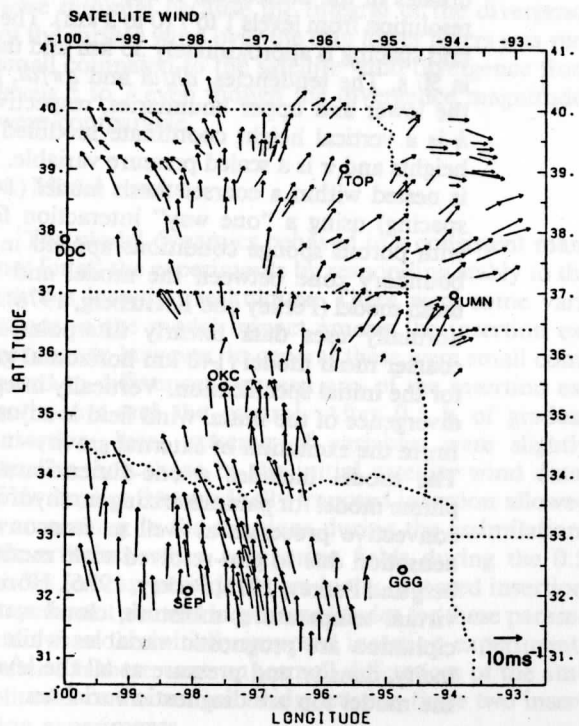

FIG. 3. Original low-level satellite wind data set obtained for the study area from 1742 to 1800 GMT SMS images. State boundaries are shown by dotted lines. The length of the vectors is proportional to wind speed. The scale for speed is given by the reference labeled 10 m s^{-1} vector in the lower right hand corner.

and Stephenville) which were located within the satellite wind-data domain. The vertical shear in the area studied was generally weak suggesting that layer-averaged satellite wind data in the 900–700 mb layer would be a meaningful parameter that would not introduce errors larger than those expected from other sources.

Hourly surface observations were available at 36 stations with average horizontal resolution of 150 km in the area in which the satellite wind vectors were obtained. This surface wind data set was combined with the satellite wind data set to initialize the numerical model. For simplicity the term "satellite wind data" will be used to refer to both the satellite and surface wind data. Satellite wind data were interpolated to model grid points using the objective analysis scheme developed by Barnes (1973). Details of the satellite data quality and interpolation effects are described in a companion paper, Lee and Houghton (1984).

3. Numerical model initialization

a. Mesoscale numerical model

The numerical model used for this study is the fine-mesh regional scale hydrostatic primitive equation model developed by Perkey (1976). The model uses height as the vertical coordinate and spherical coordinates in the horizontal. It has 15 levels with higher resolution from levels 1 to 7 (0 to 3 km). The horizontal grid spacing is approximately 35 km and the time step is 50 s. The tendencies, dh/dt and $d\pi/dt$, are zero at the lower and upper boundaries, respectively, where h is a vertical height coordinate modified by terrain heights and π is a scaled pressure variable. The model is nested within a coarser mesh model (140 km grid spacing) using a "one way" interaction formulation with porous sponge conditions applied in the lateral boundary zone between the model and the coarser mesh model (Perkey and Kreitzberg, 1976). The model normally uses data linearly interpolated from the coarser mesh model (140 km horizontal grid spacing) for the initial specification. Vertically integrated mass divergence of the initial wind field is adjusted to minimize the excitation of external gravity–inertia waves. The model includes a one-dimensional sequential plume model for parameterizing nonhydrostatic moist convective processes as well as nonconvective condensation due to grid-resolved scale motions (Kreitzberg and Perkey, 1976; Perkey, 1976). Horizontal wind, virtual temperature, moisture, cloud water and precipitation are prognostic variables while vertical velocity, density and pressure at all the levels except at the model top are diagnostic variables.

b. Experimental design

Three 6 h simulations were made starting from 1800 GMT to be close to the time for the satellite obser-

vations (1742 to 1800 GMT). The first, the control experiment, was initialized from the 6 h forecast fields (valid at 1800 GMT) of the coarser mesh model. The coarse-mesh model had been initialized from 1200 GMT National Weather Service rawinsonde data. An initialization of the fine-mesh model from the special SESAME rawinsonde data at 1800 GMT would likely have produced a more noisy control experiment which would have obscured somewhat the satellite wind impacts. Differences between the forecasts of the control and insertion experiments, which arise due to the satellite wind insertion, thus incorporated differences between the control and the real atmosphere at 1800 GMT resolvable by a 140 km grid.

The other two simulation experiments involved the use of the satellite wind data in the initialization. Here changes were made only in the velocity field. The mass and pressure fields were unaltered. The first experiment, denoted the "initially imposed insertion" was handled identically to the control except for the insertion of the satellite wind data at the initial time into the lower levels of the model over a limited horizontal domain. The second experiment, termed the "gradually imposed insertion", accomplished the insertion for the satellite wind data by a gradual replacement method. The gradual replacement was done from 1800 GMT to 1830 GMT by using the satellite wind data to modify the model forecast winds. The updated value was given by

$$(\text{updated wind}) = \alpha(\text{satellite wind})$$
$$+ (1 - \alpha)(\text{current model wind}), \quad (1)$$

where α is a weighting factor that increases linearly from zero to unity between 1800 and 1815 GMT and then decreases linearly to zero by 1830 GMT. Fig. 4 summarizes the overall experimental design.

The domain of insertion along with the horizontal grid and vertical resolution is shown in Fig. 5. The model domain ranges from 27.18 to 45.94°N (61 grid points) and from 104.83 to 84.02°W (52 grid points).
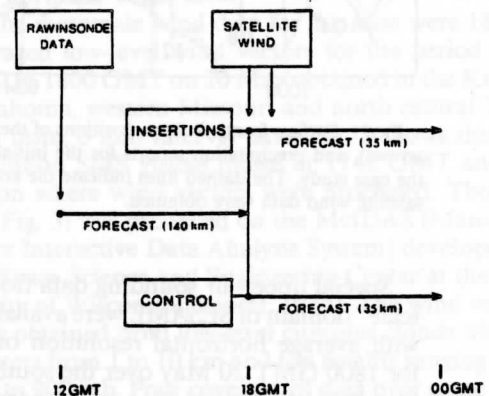

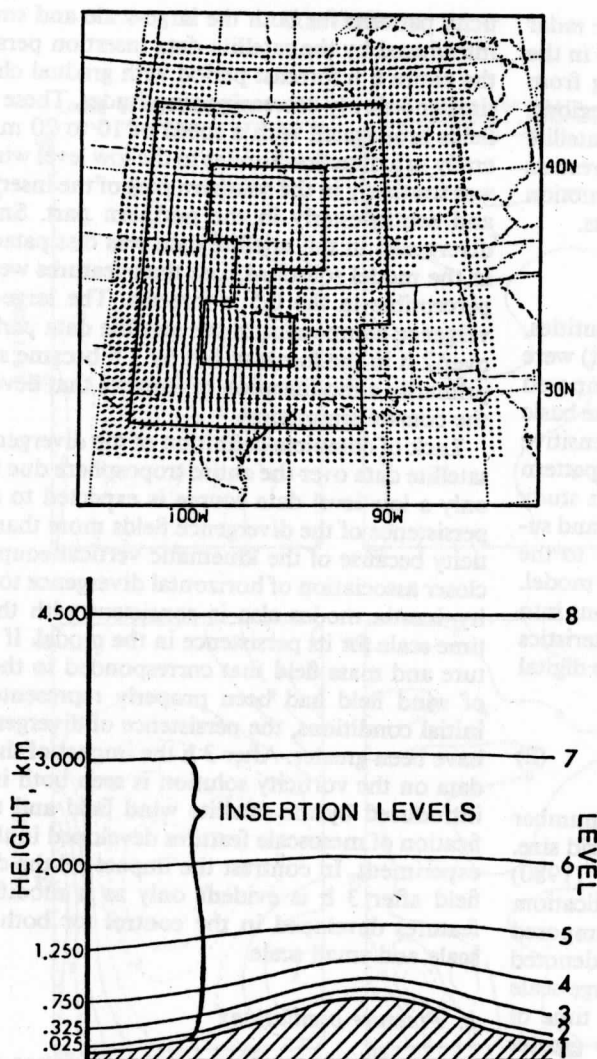
FIG. 4. Overall experimental design.

FIG. 5. Horizontal (upper panel) and vertical (lower panel) model domains where wind data were inserted. In the upper panel, grid points vectors at 2 km height are shown. The innermost enclosure is the insertion area. The transition boundary zone is between the two solid perimeter lines within the grid-point region. In the lower panel, only the lower portion of the 15-layer model is depicted.

For the insertion experiments a special transition boundary zone was used to reduce the horizontal discontinuities in the wind fields at the satellite data insertion boundary. It was a band of 9-grid-increments width surrounding the insertion area. The wind values in this transition boundary zone were computed by weighting the values of inserted satellite wind data by 1.0, 0.9, . . . , 0.2, 0.1 and model winds by 0.0, 0.1, . . . , 0.8, 0.9 respectively on rows progressing outward from the insertion boundaries for 9 grid spacings. Model data were replaced with inserted data from levels 1 to 7. Surface wind observations were used at level 1, satellite wind data were used at levels 5, 6 and 7, and averaged values of surface and satellite wind data

replaced the model winds at levels 2, 3 and 4 in the insertion area. Levels 5 to 7 (1.25 to 3 km) corresponded closely to the 900 to 700 mb layer originally assigned to the satellite wind vectors. Thus, the inserted data had no vertical shear between layers 5, 6 and 7, and between layers 2, 3 and 4, respectively, leading to layers where divergence is initially constant with height and vertical motion varies linearly with height.

After all initial data had been assembled in the model, an adjustment was made to suppress the initial excitation of spurious external gravity wave modes. This was done by an iterative procedure making corrections at all levels and was applied to the entire model domain including the region where inserted wind data had been added so that the vertical motion would be zero at the upper boundary. In the insertion and boundary transition regions, the adjustment procedure slightly suppressed the amplitude of divergence in the satellite wind data but it did not significantly affect the phase and pattern of the small-scale features. At the upper levels it resulted in adding divergence of sign opposite to that in the satellite wind data at the lower levels. However, the magnitude of contribution at the upper levels was considerably less than that in the satellite data levels because of the much larger thickness encompassed by the upper levels. Contributions to this adjustment from the surface wind data were minimal because the integral of the divergence of the surface wind over the thin lower layers was very small compared to the satellite wind divergence from levels 5 to 7 even though the divergence magnitudes were comparable.

4. Model results

The model dynamics behaved in a consistent manner for all the experiments by responding stably to the various insertion techniques. There were some variations in the model impact among the insertion experiments; however, in general these were small compared to differences between any of the insertion experiments and the control. After 0.5 h of gradual insertion, local extrema of variables were slightly smaller than those in the initial satellite wind data. This implies that gradually imposed insertion allowed a smoothing in the solutions during the assimilation. Nevertheless, when comparing fields during the 0.5 to 3 h forecast period, the gradually imposed insertion experiment showed larger amplitudes for these parameters than the initially imposed insertion experiment. After 3 h there were only small differences of the amplitudes in the motion fields between these two insertion experiments.

The primary effect of the inserted data in the insertion experiments after 3 h was to alter the amplitude of mesoscale features developed in the control. In general, both the control and the insertion experiments made realistic forecasts for the major convective ac-

tivity that developed in the area (in terms of the radar summary as shown in Fig. 9). Spurious patterns in the transition regions existed in the results arising from the initial nonuniformity of the data in these regions. These did not obscure other impacts of the satellite data. The remaining portion of this section presents in more detail the model impacts for horizontal motion fields, pressure fields and precipitation forecasts.

a. Horizontal motion fields

The horizontal motion field gradient quantities, vorticity and divergence, at level 6 (2 km height) were examined for the control and the initially imposed insertion experiment forecasts. Although not the basic inserted variable, these quantities provide a sensitive measure of motion field characteristics of phase, pattern and propagation. In the model solutions of this study there existed complicated interactions between and superposition of motions of different scales due to the insertion of the satellite wind data into the model. Thus, it was desirable to separate model solutions into component scales in order to clarify the characteristics of the simulation. The response function of the digital filter used for this purpose is

$$R^m(L) = \left[1 - \sin^4\left(\frac{\pi\Delta}{L}\right) \right]^{2m}, \qquad (2)$$

where R is response function, L wavelength, m number of applications of the filter and Δ horizontal grid size. Shapiro (1970) and Bettge and Baumhefner (1980) discussed this type of digital filter and its application.

Vorticity and divergence fields were decomposed into two scale ranges using this digital filter denoted large-scale and small-scale, respectively. The large-scale features, which were dominant at the initial time of the control, have half wavelengths primarily greater than 400 km (about 12Δ where Δ is 35 km). The small-scale features, which developed in the control case as well as being dominant in the satellite data, have half wavelengths ranging from 150 to 400 km (about 4Δ to 12Δ). Figs. 6 and 7 show the decomposition results for vorticity and divergence in the area within which the satellite wind data were obtained, respectively, in the control and initial insertion experiments.

For the control, the initial large-scale vorticity pattern was persistent for the entire time period while there were gradual changes in pattern and amplitude of large-scale divergence. Small-scale features developed from an initial state of primarily large-scale features. These developments of small-scale features (as evidenced by the increased amplitude of the small-scale component for the control case after the initial time as shown in Figs. 6 and 7) occurred at different times in the forecast for the rotational and divergent components, i.e., at about 2.5 h for the vorticity and at 0.5 h for the divergence.

For the initially imposed insertion experiment, vor-

ticity patterns for both the large-scale and small-scale introduced by the satellite data insertion persisted for the entire 6 h forecast period with gradual changes in time and slowly decreasing amplitudes. These vorticity fields propagated with a speed of 10 to 20 m s^{-1} generally in a direction similar to the low level wind which was southerly in the southern part of the insertion area and southwesterly in the northern part. Small-scale divergence in the satellite data was dissipated rapidly in the model solutions, i.e., their features were barely perceptible in the 0.5 h forecast. The large-scale divergence component in the satellite data persisted for over 2 h in the forecast, but by 3 h became small and primarily a modification of features that developed in the control simulation.

Lack of complete definition of the divergence in the satellite data over the entire troposphere due to having only a low-level data source is expected to affect the persistence of the divergence fields more than the vorticity because of the kinematic vertical coupling. The closer association of horizontal divergence to the gravity-inertia modes also is consistent with the shorter time scale for its persistence in the model. If the moisture and mass field that corresponded to those scales of wind field had been properly represented in the initial conditions, the persistence of divergence might have been greater. After 3 h the impact of the inserted data on the vorticity solution is seen both in features introduced by the satellite wind field and the modification of mesoscale features developed in the control experiment. In contrast the impact on the divergence field after 3 h is evident only as a modification of features developed in the control for both the large scale and small scale.

b. Pressure oscillations

Figure 8 shows the pressure difference fields at 2 km height between the initially imposed insertion and the control, and between the gradually imposed insertion and the control experiments. The time changes in these difference fields indicated the presence of both internal and external modes in the mesoscale features introduced from the satellite wind data insertion. The internal modes in both experiments propagated with speeds of 15–45 m s^{-1} observed by tracking local extrema of the difference fields. For the gradually imposed insertion experiment the external mode had additional large amplitude oscillations propagating outward with a speed of about 300 m s^{-1}. These oscillations disappeared after 2 h and thereafter the pressure had the same pattern and phase as in the initially imposed insertion experiment. The difference magnitude of the additional external mode at 2 km height was three to four times greater than that of the internal mode. However, these external mode pressure oscillations did not modify other aspects of the model solution.

Benwell and Bretherton (1968) and Anthes et al.

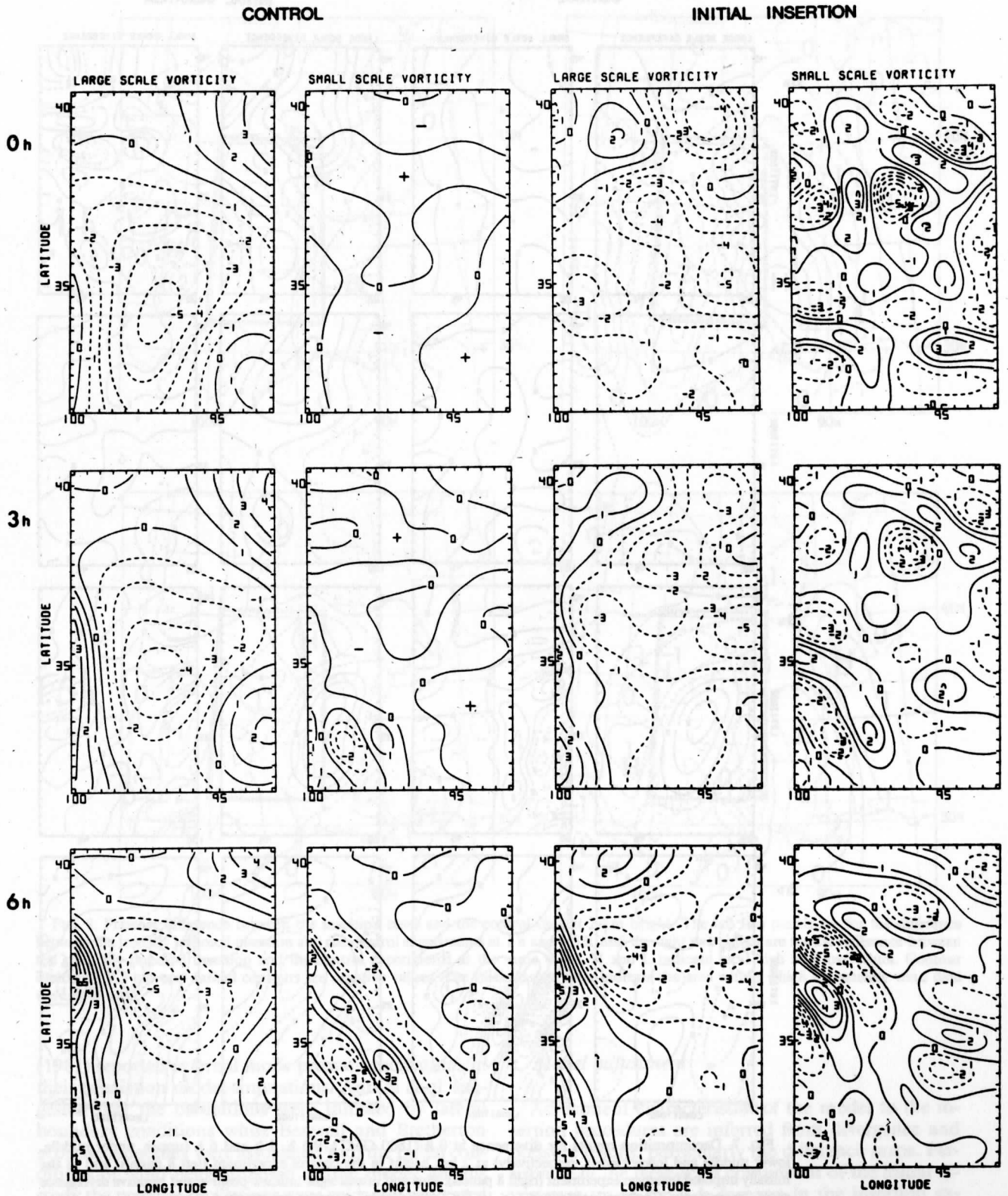**CONTROL**   **INITIAL INSERTION**

FIG. 6. Decomposition results for vorticity at 0 h (1800 GMT), 3 h and 6 h (upper, middle and lower panels respectively) at 2 km height in the control experiment (left 6 panels) and in the initially imposed insertion experiment (right 6 panels). Plus and minus signs indicate positive and negative vorticity areas, respectively. Contour interval is 1×10^{-5} s^{-1} and dashed contours are negative values.
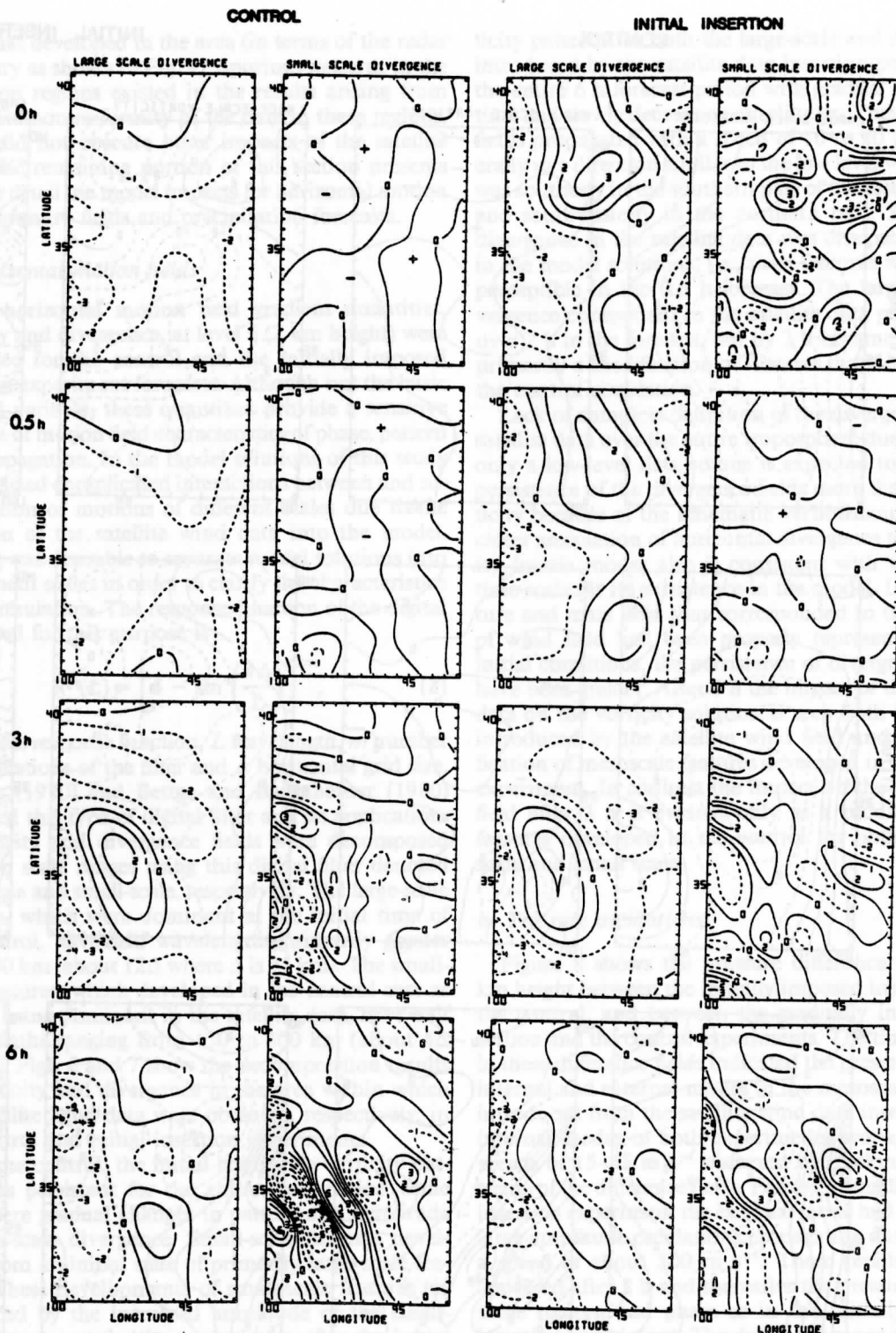
CONTROL

INITIAL INSERTION

FIG. 7. Decomposition results for divergence at 0 h (1800 GMT), 0.5 h, 3 h and 6 h (upper, upper middle, lower middle and lower panels, respectively) at 2 km height in the control experiment (left 8 panels) and in the initially imposed insertion experiment (right 8 panels). Plus and minus signs indicate positive and negative divergence areas, respectively. Contour intervals is 1×10^{-5} s^{-1} and dashed contours are negative values.
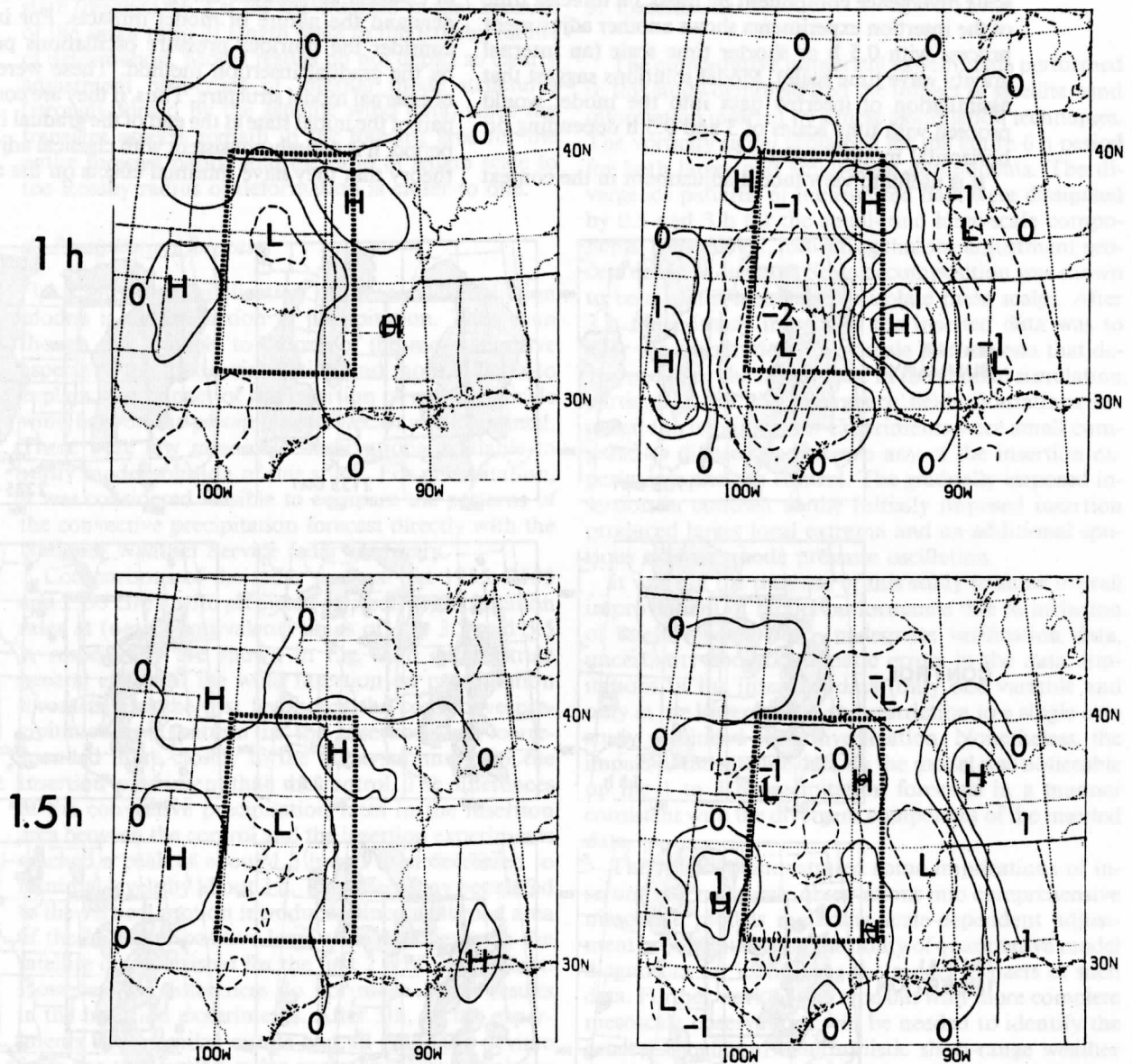
FIG. 8. Pressure difference between the insertion cases and the control case at 2 km height. The left two panels are for the difference between the initially imposed insertion and the control experiments at 1 h and 1.5 h, and the right two panels are for the difference between the gradually imposed insertion and the control experiments at the same times. H and L indicate local high and low values. Contour interval is 0.5 mb and dashed contours are negative values. The thick dashed lines indicate the area within which the satellite wind data were obtained.

(1981) reported external mode pressure oscillations in their prediction model simulations. Anthes *et al.* suggested that the oscillations were initiated by lateral boundary conditions while Benwell and Bretherton proposed that they were associated with the initial conditions of wind fields imposed on the model. In this study the pressure oscillations were evidently generated by the initial divergence field of the inserted wind data when imposed on the model over a finite length of time.

c. Model adjustment

Adjustment characteristics of the model to the insertion procedures are inferred from divergence and pressure results, particularly the difference maps. Persistence of the large-scale component of the initial divergence up to the 3 h forecast in the insertion experiments indicates an adjustment process with time scale 3 h (inertial motion time scale), i.e., $1/f$ where f is the Coriolis parameter. Dissipation of the small-

scale divergence component by the 0.5 h forecast time of the insertion experiments shows another adjustment process with 0.5 h or shorter time scale (an internal gravity wave time scale). Model solutions suggest that assimilation of inserted data into the model would proceed with time scales of 3 and 0.5 h depending on horizontal motion scales.

It is useful to view model adjustment in the context of classical adjustment theory (Blumen, 1972) to understand the nature of model impacts. For instance, consider the spurious pressure oscillations produced by the gradual insertion method. These were clearly of external model structure. Thus, if they are considered part of the initial state at the end of the gradual insertion period, it is entirely consistent with classical adjustment theory that they have minimal effects on the adjusted
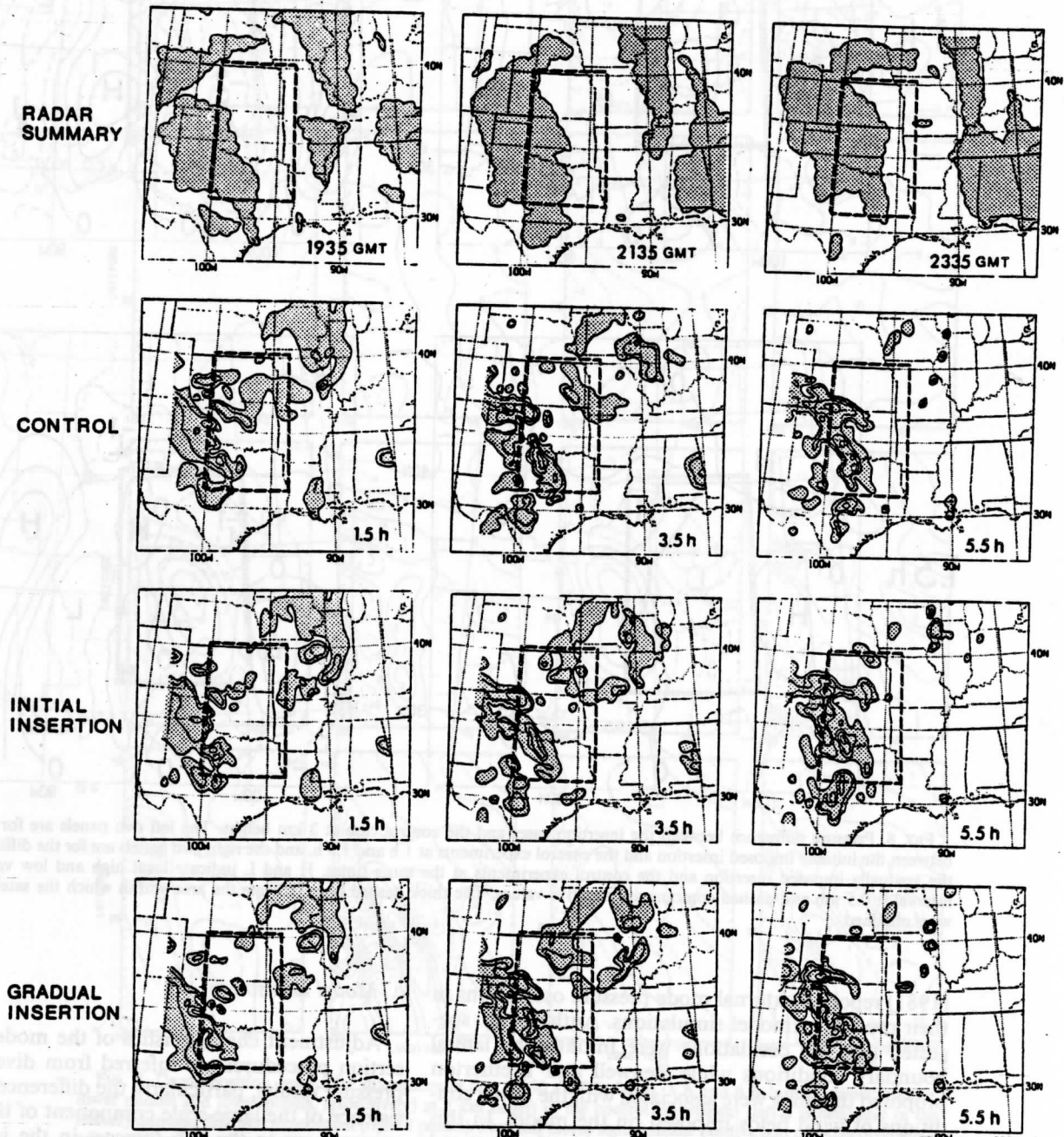

FIG. 9. Comparison of radar summary with convective precipitation forecasts for the control, the initially imposed insertion and the gradually imposed insertion experiments. The radar echo regions and forecast convective precipitation rates are shaded. The dashed lines indicate the area within which the satellite wind data were obtained. Contour interval of the forecast field is 4×10^{-4} mm s^{-1}.

state (reached by 2 h for the external mode) because of the small ratio of length scale to the Rossby radius of deformation. Model results do not depict so clearly adjustment properties of internal mode structures (strongly forced by the satellite wind data) since the transient aspects remain in the forecast area for the entire forecast period and the ratio of length scale to the Rossby radius of deformation is closer to one.

d. Precipitation forecasts

An important application of mesoscale prediction models is the prediction of precipitation. Thus even though this is likely to be one of the more sensitive aspects of the model simulation and more difficult to explain, the impact of the insertion of real mesoscale wind field on the precipitation forecast was examined. There were few mesoscale observations available to verify model solution of this study. For precipitation, it was considered feasible to compare the patterns of the convective precipitation forecast directly with the National Weather Service radar summary.

Comparisons of the radar summary at 1935, 2135 and 2335 GMT with predicted convective precipitation rates at (nearly equivalent) times of 1.5, 3.5 and 5.5 h, respectively are shown in Fig. 9 to demonstrate general effects of the wind insertion on precipitation forecasts. For the first few hours the convective precipitation rate pattern in the insertion area corresponded more closely to the radar summary for the insertion experiment than the control. The differences of the convective precipitation rates in the insertion area between the control and the insertion experiments reached a peak at about 1.5 h and then decreased to minimal levels by about 3 h. This effect may be related to the vertical motion introduced since the broad area of the low-level positive large-scale divergence in the satellite data persisted for the first 2 h of the forecast. However, the differences do not mean better results in the insertion experiments. After 3 h, all the experiments show similar results and all gradually deviate from the verification radar summary, especially over the Illinois and Wisconsin area. By 6 h there are reductions in intensity but at the same time improvement in coverage of the convective activity in the Kansas, Oklahoma and Texas area.

Tarbell et al. (1981) reported on an initialization experiment with a mesoscale numerical model where the use of diagnosed divergence derived from the omega equation, including a latent heating term, improved the first 3 h precipitation forecast but the unbalanced data with observed divergence did not improve the forecasts. There was no clear improvement in the overall precipitation forecast in the current case study but the precipitation forecast for the first few hours did show changes consistent with the divergence field of the inserted data. It should be noted that the scales of the divergence here are considerably smaller than those in the Tarbell et al. study.

5. Conclusions

The comparative numerical experiments performed in this study demonstrated the impact of satellite wind information inserted by simple assimilation techniques. The vorticity signal remained for the entire 6 h period for both large- and small-scale components. The divergence patterns of the inserted data were dissipated by 0.5 and 3 h for the small- and large-scale components, respectively, indicating that the adjustment process depends on scale. Scale decomposition was shown to be a useful technique to isolate these scales. After 3 h the primary impact of the inserted data was to alter the amplitude of mesoscale phenomena that developed after the initial time in the control simulation particularly for the divergence fields. Variations between the two insertion experiments were small compared to differences between any of the insertion experiments and the control. The gradually imposed insertion in contrast to the initially imposed insertion produced larger local extrema and an additional spurious external mode pressure oscillation.

It was not the purpose of this study to show overall improvement of model performance due to inclusion of satellite wind data. Inadequate verification data, uncertainty about systematic errors in the data, limitations in the insertion data (only one variable and only at the lower levels) and restriction to a single case study precluded such investigation. Nonetheless, the impact of the satellite data on the model was noticeable on the 1 to 3 h precipitation forecasts in a manner consistent with the divergent component of the inserted data.

The results demonstrated some implications of inserting real mesoscale observations into comprehensive mesoscale models including scale-dependent adjustment process times and the utility of quantitative model diagnostics for identifying the model impacts of such data. Further work of this type but with more complete mesoscale observations will be needed to identify the general benefits to deterministic short-range weather prediction that can be expected from proper definition of the initial mesoscale state.

REFERENCES

Anthes, R. A., E. Hsie, D. Keyser and Y. Kuo, 1981: Impact of data and initialization procedures on variations of vertical motion and precipitation in mesoscale models. IAMAP Third Scientific Assembly, Hamburg, 245–257. [Available from European Space Agency, c/o ESTEC, Noordwijk, Netherlands.]

Barnes, S. L., 1973: Mesoscale objective map analysis using weighted time-series observations. NOAA Tech. Memo. ERL NSSL-62, Norman, OK, 60 pp. [Available from NTIS, U.S. Dept. of Commerce, 5285 Fort Royal Rd., Springfield, VA 22161, Identification No. COM-73-10781.]

Bengtsson, L., 1975: 4-dimensional assimilation of Meteorological observations. GARP Publ. Ser. No. 15, GARP, WMO-ICSU, 76 pp. [Available from the World Meteorological Organization, Case postale No. 5, CH-1211 Geneva 20, Switzerland.]

Benwell, G. R. R., and F. P. Bretherton, 1968. A pressure oscillation in a 10 level atmospheric model. Quart. J. Roy. Meteor. Soc., 94, 123–131.

Bettge, R. W., and D. P. Baumhefner, 1980: A method to decompose the spatial characteristics of meteorological variables within a limited domain. Mon. Wea. Rev., 108, 843–854.

Blumen, W., 1972: Geostrophic adjustment. Rev. Geophys. Space Phys., 10, 485–528.

Haltiner, G. J., and R. T. Williams, 1980: Numerical Prediction and Dynamic Meteorology. Wiley and Sons, 477 pp.

Hasler, A. E., W. E. Shenk and W. C. Skillman, 1977: Wind estimates from cloud motion: Results from Phase I, II and III on an in situ aircraft verification experiment. J. Appl. Meteor., 16, 812–815.

Hoke, J. E., and R. A. Anthes, 1976: The initialization of numerical models by a dynamic initialization technique. Mon. Wea. Rev., 104, 1551–1556.

——, and ——, 1977: Dynamic initialization of a three-dimensional primitive-equation model of Hurricane Alma of 1962. Mon. Wea. Rev., 105, 1266–1280.

Kreitzberg, C. W., and D. J. Perkey, 1976: Release of potential instability: Part II: A sequential plume model within a hydrostatic primitive model. J. Atmos. Sci., 33, 456–475.

Lee, D. K., and D. D. Houghton, 1984: A quantitative study of satellite winds for mesoscale meteorology. Mon. Wea. Rev., 112, 990–1004.

MacFarland, M. J., and Y. K. Sasaki, 1977: Variational analysis of temperature and moisture advection in a severe storm environment. J. Meteor. Soc. of Japan, 55, 412–430.

Perkey, D. J., 1976: A description and preliminary results from a fine-mesh model for forecasting quantitative precipitation. Mon. Wea. Rev., 104, 1513–1526.

——, and C. W. Kreitzberg, 1976: A time-dependent lateral boundary scheme for limited-area primitive equation models. Mon. Wea. Rev., 104, 744–755.

Peslen, C. A., 1980: Short-interval SMS wind vector determination for a severe local storm area. Mon. Wea. Rev., 108, 1407–1418.

Rao, G. V., and J. Fishman, 1975: An iterative initialization scheme for mesoscale studies. Tellus, 27, 157–167.

Shapiro, R., 1970: Smoothing, filtering and boundary effects. Rev. Geophys. Space Phys., 8, 359–387.

Suchman, D., and D. Martin, 1976: Wind sets from SMS images. An assessment of quality for GATE. J. Appl. Meteor., 15, 1265–1278.

Suomi, V. E., 1975: Man computer interactive data access system (McIDAS). NASA Contract NAS 5-23296, SSEC, University of Wisconsin, Madison, [NTIS No. 75N28733].

Tarbell, T. C., T. T. Warner and R. A. Anthes, 1981: The initialization of the divergent component of the horizontal wind in mesoscale numerical weather prediction models and its effect on initial precipitation rates. Mon. Wea. Rev., 109, 77–95.

Wilson, T. A., and D. D. Houghton, 1979: Mesoscale wind fields for severe storm situation determined from SMS cloud observations. Mon. Wea. Rev., 107, 1198–1209.

UTILIZING SATELLITE WIND DATA IN A MESOSCALE NUMERICAL MODEL

by

Dong Kyou Lee and David D. Houghton
Department of Meteorology
University of Wisconsin
Madison, WI 53706

ABSTRACT

High resolution satellite and surface wind data
are incorporated into a mesoscale numerical pre-
diction model for a 20 May 1977 case study in the
south central region of the United States. Cor-
respondence of the satellite data to special 18
GMT rawinsonde observations is analyzed. Three
six-hour forecasts are made with a 35 km grid
numerical model with both initially and gradually
imposed insertion techniques. Differences between
forecasts with and without the special initial
wind data identify the impact of this data. Oscil-
lations indicative of adjustment processes with
time scales of 1/2 and 3 h are evident in the in-
sertion cases. The primary impact of the insert-
ed data is to alter the amplitude of mesoscale
features that develop in the control forecast.

KEYWORDS: Satellite winds, mesoscale models, in-
itialization, model diagnostics, scale decomposition

1. INTRODUCTION

In recent years special observing programs such as
SESAME and observing systems such as the geosta-
tionary satellites have begun to provide mesoscale
data sets that approach the level of comprehensive-
ness needed for the general study of mesoscale
phenomena and for their simulation by numerical
techniques.

A major effort is now needed to develop the cap-
ability to utilize the information contained in
these mesoscale observations. The synthesis of
data from a wide range of sources will be required
and comprehensive numerical models will be essen-
tial. The strategy for and implications of insert-
ing such basically nonhomogeneous data into a
mesoscale prediction model will require extensive
numerical experimentation and numerous case studies
that encompass the range of mesoscale dynamical
situations.

In this study attention is focused on the impacts
of mesoscale wind data as part of an initial
specification for a dynamical numerical model.
Mesoscale wind initialization has been considered
by Tarbell, Warner and Anthes (Ref. 8). Studies
concerning the contributions of mesoscale mass and

moisture observations will also be required in
order to fully handle the study of mesoscale
analysis, synthesis and prediction. This invest-
igation is quite preliminary since the wind data
available lack the full four dimensional charac-
ter needed for optimal experimental design. In
addition, defining the most meaningful measures
of impact awaits better understanding of the
structure and dynamics of mesoscale systems. In
this paper one case study is examined and a
variety of diagnostic methods are tested.

2. SYNOPTIC SITUATION AND MESOSCALE DATA

The case study centers on activity in the eastern
portion of a developing trough moving into the
south central region of the United States. At
1800 GMT 20 May 1977 there is a broad area of low
level southerly wind coming into the region of
interest. At the middle and upper levels, a
general flow of southwesterly difluent winds
accompanies a jet approaching the region studied.
Only at levels below 700 mb is there a broad area
of moisture drawn in by the southerly flow. A
major thunderstorm band is developing near the
northwestern part of Texas. By 0000 GMT 21 May the
low level flow has increased in speed and a deeper
layer shows high moisture content. The jet stream
is now centered in the area studied and strong
convective thunderstorm bands exist in the south-
western area of this study.

The satellite wind data used in this study are
averaged wind vectors obtained from four high-
resolution SMS visible images from 1742 to 1800
GMT on May 20 in the Kansas, western Missouri,
Oklahoma and north central Texas area. The data
set was produced by the McIDAS developed by the
Space Science and Engineering Center at the
University of Wisconsin. The final data set
consisted of 287 low level wind vectors as shown
in Fig. 1. The wind vectors were obtained from
low level cumulus clouds with top heights ranging
about from 700 to 900 mb.

Special upper air sounding data (SESAME) were
available at 17 stations for 1800 GMT 20 May over
the south central United States. Hourly surface
observations were reported at 36 stations in the
area in which the satellite wind vectors were
obtained. This surface wind data set was combined
with the satellite wind data set to initialize the
numerical model.

The vertical wind shear was examined analyzing the
vertical profile of the low level soundings from
900 to 700 mb over the four stations (TOP, UMN, OKC
and SEP) which are located within the satellite wind
data domain of this study (see Fig. 1). No profiles
showed directional wind shear greater than 30 de-
grees in the 900-700 mb layer which corresponded to
the layer of the satellite wind data. The winds
at TOP, UMN and SEP veered with height while the
winds at OKC backed with height. It was concluded
that using layer-averaged satellite wind data in the
900-700 mb layer would not introduce an unreasonably
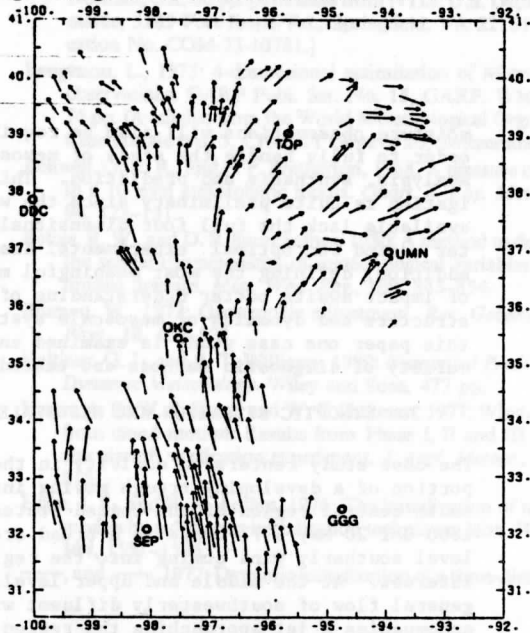large change in the vertical shear characteristics.

*Fig. 1.   Satellite wind data for the case study.
The length of the vector is proportioned to wind
speed. The locations of the upper air stations in
the region are shown by hollow circles.*

Direct correspondence of satellite winds with
rawinsonde winds is not expected due to the dif-
ference of measurement character and the incom-
patibility in spatial as well as temporal resolu-
tion. There have been, however, a number of studies
to determine the relationship of satellite wind to
conventional wind data. Quality estimates of the
satellite wind data were made comparing the two
data sets in terms of magnitude and direction.

The RMS vector differences between satellite winds
and layer-averaged rawinsonde winds in the 900-
700 mb layer were computed for satellite winds
within prescribed distances of the rawinsonde
stations. These circular regions had radii ranging
from .25 to 2.00 degrees of latitude around each
rawinsonde station using increments of .25 degrees
of latitude. The difference between the mean
of satellite winds within the circles and the
center point rawinsonde wind was also determined.
The results at two stations (TOP and SEP) are
shown in Fig. 2. Increasing the number of satellite
winds around a rawinsonde station tends to improve
the correspondence of the satellite and rawinsonde
wind information. The RMS values also indicate
mesoscale spatial variability as a function of
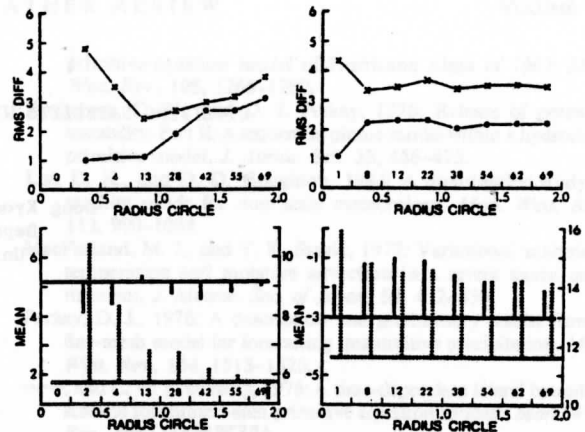distance between winds. Generally, these RMS

*Fig. 2.   Comparison of RMS and mean vector dif-
ferences between satellite wind and rawinsonde
wind at TOP (left panels) and SEP (right panels).
For the RMS difference the lines with hollow
circles are for u-component wind and the lines
with X are for v-component. For the mean differ-
ence the horizontal lines indicate layer-averaged
rawinsonde wind and vertical lines represent the
difference between the mean of satellite winds
within the given circles and the rawinsonde wind.
Solid and dashed lines denote u-component and
v-component values, respectively. The number of
individual satellite wind vectors within the given
circles are also shown above the abscissa axis.
The units are m s^{-1}.*

values (about 3 m s^{-1}) are comparable to those
reported in other studies (Bauer (Ref. 1) and
Wilson and Houghton (Ref. 4)).

The streamlines and isotachs in the region of
study for both the satellite and rawinsonde data
are shown in Fig. 3. Wind direction and flow
patterns correspond well between the two data sets.
Velocity gradients agree but magnitudes of maximum
speed show differences. Small scale features are
noted in the isotach analysis of satellite data.

There is some similiarity of the surface flow field
to the satellite winds. However, the vorticity
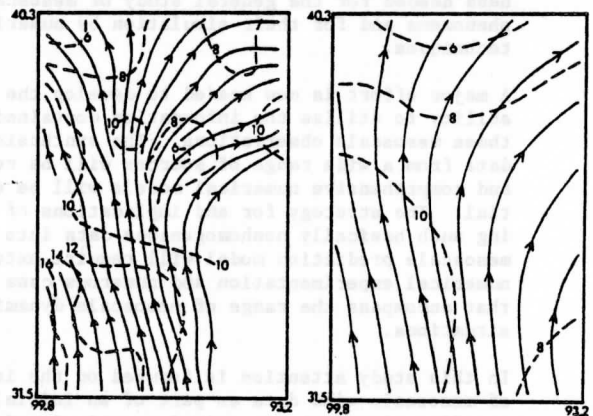and divergence patterns do not correspond well.

*Fig. 3.   Streamlines and isotachs for the satel-
lite wind data (left panel) and the rawinsonde
wind data in the same area (right panel). Dashed
lines are isotachs with units of m s^{-1} with a
contour interval of 2 m s^{-1}.*

The signal (magnitudes) of mesoscale vorticity and divergence is much more apparent in the satellite winds than in the surface data.

3. NUMERICAL MODEL EXPERIMENTS

1. Experimental Design

The numerical model used is a version of the fine mesh regional scale hydrostatic primitive equation model described by Perkey (Ref. 7) and Kreitzberg (Ref. 5). It has 15 levels from 0 to 16.0 km with higher resolution in the surface boundary layer. The horizontal grid spacing is 35 km and the time step is 50 seconds. The model uses NMC initial data or radiosonde data for initial specification. The porous sponge conditions are applied in the lateral boundary zone of the model. Satellite and surface wind data are interpolated to model grid points using an objective analysis scheme developed by Barnes [Houghton, Lee and Chang (Ref. 4.)].

Three 6-hour simulation cases are made starting from 1800 GMT. The first, referenced the "control" case, is initialized using 6 h forecast fields from a coarser mesh model run (140 km horizontal grid) that used 1200 GMT rawinsonde information as input. The second, referred to as the "initially imposed insertion" case, is handled identically to the first except for the initial time insertion of the satellite and surface wind data set into a sub-domain of the model (see Fig. 4). The third, referred to as the "gradually imposed insertion" case, is identical to the second except for gradual insertion of the special mesoscale wind data. The gradual insertion is done updating continuously a linearly combined wind of the special observational data set and the model wind data set from 1800 to 1830 GMT; i.e. α (observational wind) + $(1-\alpha)$ (model wind). The weight factor, α, increases linearly from zero at 1800 GMT to unity at 1815 GMT and then decreases linearly to zero at 1830 GMT. This gradual insertion technique is equivalent to the nudging process in the dynamic-initialization developed by Hoke and Anthes (Ref. 3).
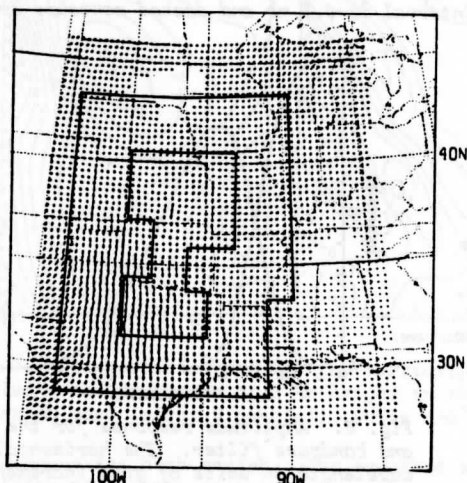

Fig. 4. Horizontal domain for insertion of satellite wind data into the model showing grid point vectors at the 2 km height. The inner enclosed area is the insertion area. The transition boundary none is between the two solid perimeter lines within the grid point region.

The domain of insertion along with the horizontal grid resolution is shown in Fig. 4. For the insertion cases, a special transition boundary zone is made to reduce the discontinuties in the wind fields at insertion boundaries. It is a band of 9 grid increments width surrounding the insertion area. The vertical specification is done by replacing the model data with insertion data from levels 1 to 7 (0 to 3 km). Surface wind observations replace the model winds at level 1, satellite wind data replace the model winds at levels 5, 6 and 7, and averaged values of surface and satellite wind data replace the model winds at levels 2, 3 and 4 in the insertion area. Levels 5 to 7 (1.25 to 3 km) correspond closely to the 900 to 700 mb height layer originally assigned to the satellite wind vectors.

After all initial data has been assembled in the model, an adjustment is made in the horizontal velocity field so that vertical motion is zero at the upper boundary. This minimizes the initial excitation of spurious external wave modes. This is done by an iterative procedure making corrections at all levels and is applied to the entire model domain including the region where the special observational wind data has been added in the insertion cases. In the insertion region the adjustment procedure suppresses slightly amplitudes of divergence in the satellite wind data but it does not effect the phase and patterns of the small scale features. At upper levels it results in adding divergence of opposite sign to that in the satellite wind data at lower levels. Contributions to the vorticity and divergence fields from the surface wind data is minimal.

2. Results

The insertion cases show that meaningful signatures the satellite wind data are added to the solution of the control case. The patterns and phases of vorticity in the satellite data are persistent for the model forecasts. The strong divergence fields in the insertion area for the insertion cases are not persistent for the entire 6 h but they alter the mesoscale features developed in the control case.

The insertion of satellite data produces pressure changes for both the initially and the gradually imposed insertion cases. Fig. 5 shows the pressure difference fields between the insertion cases and the control case, respectively. These pressure difference fields indicate the presence of both internal and external modes in the mesoscale features introduced from the satellite wind data insertion. For the gradually imposed insertion case the external modes show evident oscillations propagating outward with a speed of 280 m s^{-1}. For the initially imposed case the external modes are not found in the 1/2 h interval output and presumably are of very small amplitude.

Characteristics of the satellite wind data in the model solution are examined in detail by isolating scales of the motion solutions. In order to decompose vorticity and divergence fields for the results of the insertion case, a digital filter is constructed. The response function of this digital filter is

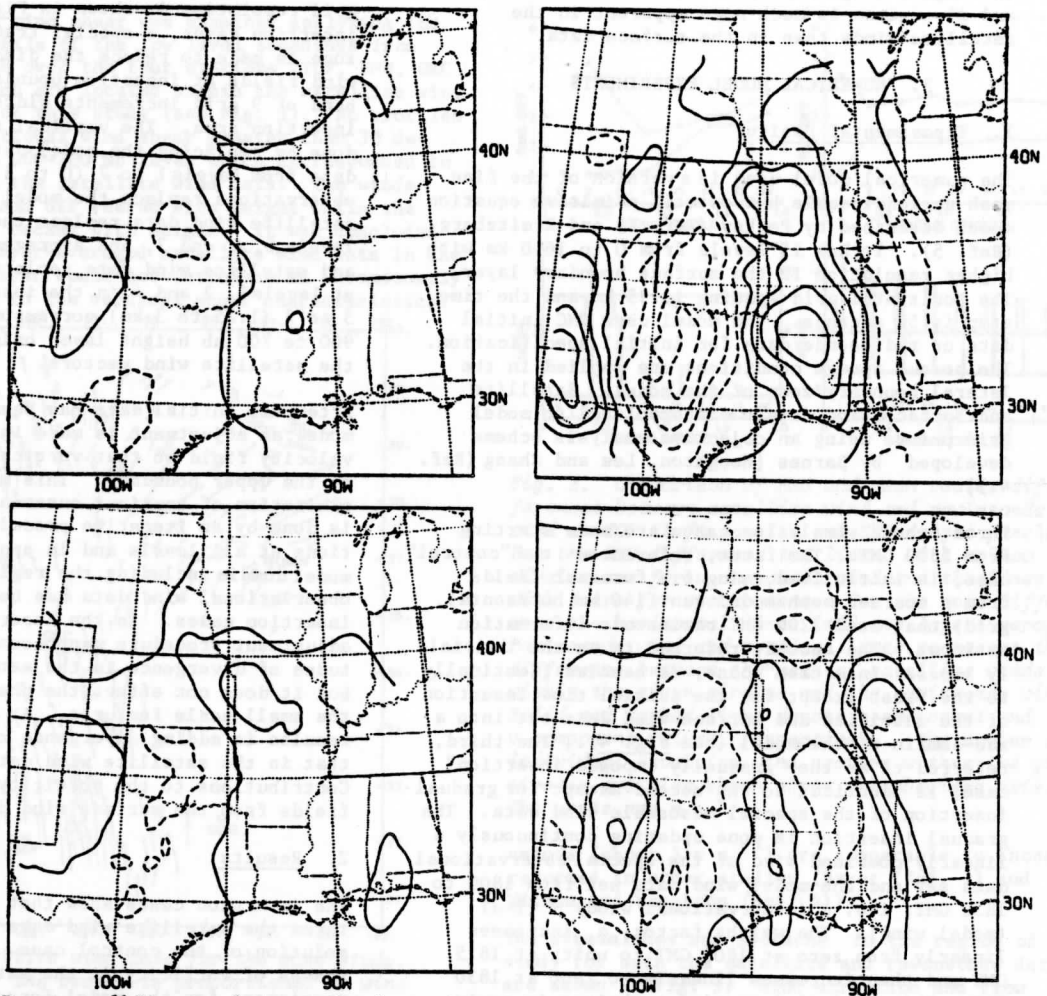$$R^m(L) = [1 - \sin^4(\frac{\Pi\Delta}{L})]^{2m} \qquad (1)$$

Fig. 5. Pressure difference between the insertion cases and the control case at 2 km height. The left two panels are for the difference between the initially imposed insertion and the control cases at 1 h and 1-1/2 h and the right two panels are for the difference between the gradually imposed insertion and the control cases at the same times. Contour interval is 0.5 mb and dashed contours are negative values.

Where L is wave length, m number of repeated applications and Δ horizontal grid size (35 km). Bettge and Baumhefner (Ref. 2) and Maddox (Ref. 6) discussed filtering techniques. Two low-pass filters are made by applying this filter 3 and 50 times to remove the small scale features up to wavelengths of 3 Δ and 8 Δ, respectively. The difference between these two low-pass filters gives the band-pass filter whose peak response is near the 8 Δ wavelength with a bandwidth of roughly 13 Δ, i.e., from 16 to 3 Δ. The lowpass filter made by applying the filter 50 times and the bandpass filter are shown in Fig. 6. The signals of the insertion data for wavelengths less than 3 Δ are not examined because it is difficult to isolate them from noise. The waves within the bandwidth of the bandpass filter dominate in the satellite data while waves longer than 8 Δ dominate in the control case.

The low-pass filter and the bandpass filter are used for the initially imposed insertion case and control case solutions. The long waves isolated by the low-pass filter are referred to as smoothed (large) scale fields while the waves from 3 Δ to 16 Δ provided by the bandpass filter are termed the small scale fields. Fig. 7 shows the decomposition results for vorticity at 0, 3, and 6 h
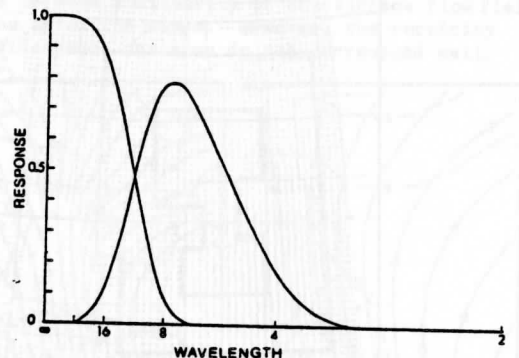

Fig. 6. Amplitude response for the low-pass filter and bandpass filter. The horizontal axis shows wavelength in units of grid increments based on a 35 km grid spacing.

in both cases. For the initially imposed case the wave patterns of both scales specified by the satellite data change gradually in time and exhibit slowly decreasing amplitudes. Some of the wave patterns in the insertion area merge with other waves or diminish in time and become indistinct. Satellite wind signals, however, are persistent
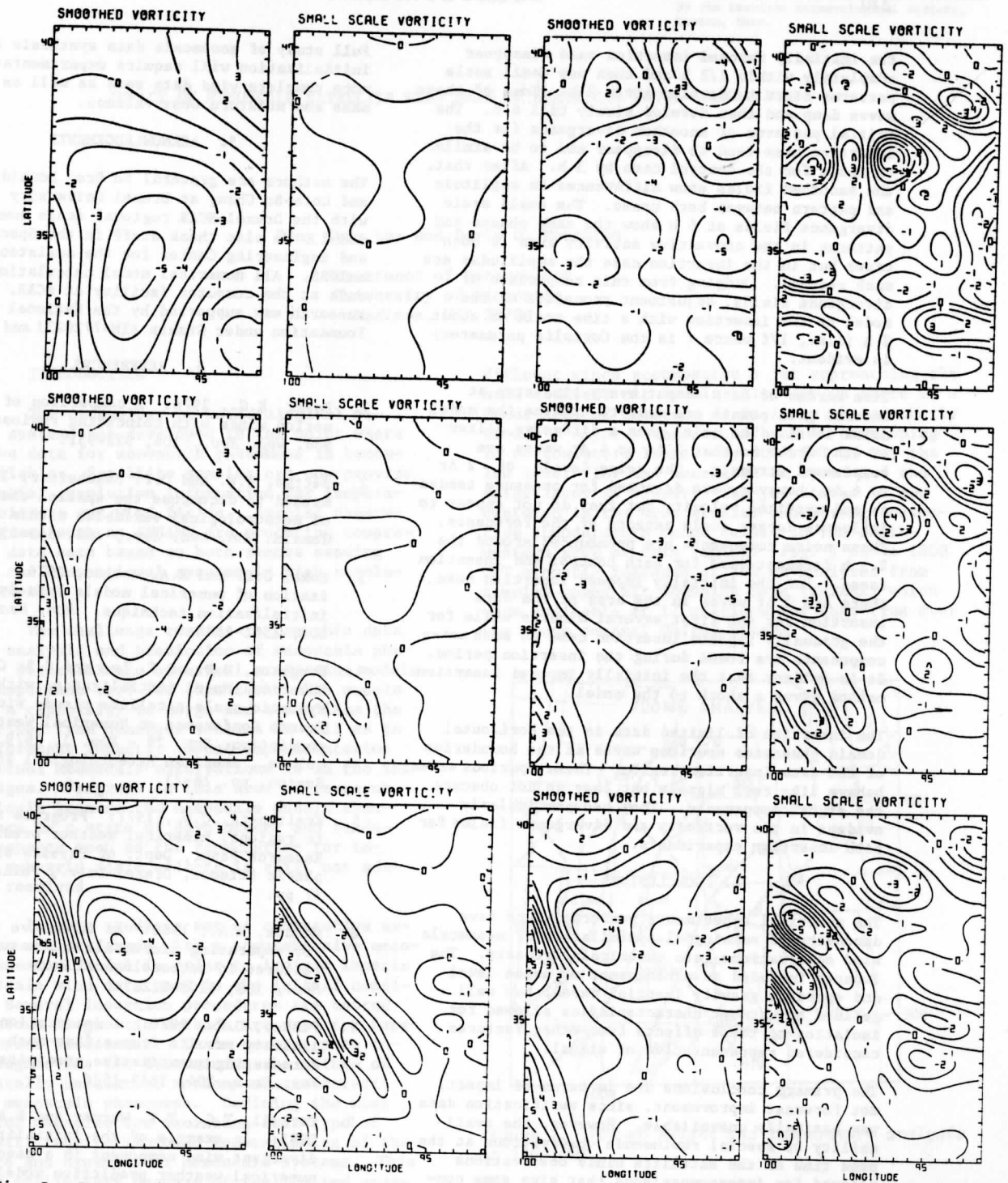
Fig. 7. Decomposition results for vorticity at 0 h (upper panels), 3 h (middle panels) and 6 h (lower panels) model forecasts at 2 km height in the control case (left 6 panels) and in the initially imposed insertion case (right 6 panels). Units are 10^{-5} s^{-1}. Contour interval is 1×10^{-5} s^{-1}.

for 6 hours for both scales. The smoothed scale vorticity fields propagate north northeast with the speeds of 5–15 m s^{-1} while the propagation of small scale vorticity fields is similar to the low level wind flow direction with similar speeds to those of the smoothed scale. For the control case, the smoothed scale vorticity which is dominated by larger scale features than those for the insertion case propagate to the north with the same speeds

as for the insertion case. The small scale vorticity for the control case is not evident initially in the data insertion area but this scale dominates in the region of the convective activity by 6 h.

The scale decomposed fields for horizontal divergence at the 2 km height were also examined. The initial patterns of small scale divergence for

the initially imposed insertion case disappear completely within 1/2 h and then new small scale patterns start to develop after 2 h. Some of these waves damp and then develop slowly till 6 h. The initial patterns of smoothed divergence for the insertion case tend to disappear and to be similar to those for the control case by 3 h. After that, the smoothed fields show differences in amplitude and pattern between both cases. The small scale divergence fields at 6 h show the same phases and patterns in the convective activity area in both cases but in the insertion case the amplitudes are much reduced. Judging from this comparison of divergence fields, adjustment processes of the model to the insertion with a time scale of about 3 h (i.e., $1/f$ where f is the Coriolis parameter) is evident.

Time series of data output every time step at several grid points are made to examine the model noise level. The model uses a diffusive filter of 4th order so that $2 \Delta t$ or $4 \Delta t$ waves are suppressed strongly. The noise levels of $2 \Delta t$ to $4 \Delta t$, however, are detected for pressure tendency and vertical velocity but they do not appear to influence larger scale aspects of the forecasts. These noise components are pronounced around the 2.5 h forecast time for both control and insertion cases. For the initially imposed insertion case there are $2 \Delta t$ waves in the area of the data insertion for the first several minutes while for the gradually imposed insertion case no such noise components are found during the insertion period. It is evident that the initially imposed insertion method gives a shock to the model.

The insertion of limited data in the horizontal domain generates spurious waves at the boundaries of the data insertion region. These spurious waves behave like real signals but they do not obscure the signal components. They are particularly evident in the vorticity and divergence fields for both insertion experiments.

4. CONCLUSIONS

The numerical experiments performed here have demonstrated meaningful assimilation of mesoscale wind observations into numerical forecasts. The impacts included an enhancement of noise level and spurious gravity inertial waves, but well defined adjustment characteristics allowed for isolation of these effects from other features considered representative of signal.

The primary conclusions are in terms of impact, not forecast improvement, since verification data was basically unavailable. However, the availability of special rawinsonde observations at the same time as the satellite winds observations allowed for intercomparisons that give some confidence in the realism of the initial mesoscale data. The surface wind reports were not the prime source of mesoscale signatures.

The range of diagnostic procedures considered served to demonstrate the complexity of determining forecast impacts. Scale decomposition and time series analysis were shown to be useful techniques. Obviously many forms of diagnostics will have to be tried and the direction of such analysis awaits the emergence of relevant dynamic models and better understanding of mesoscale phenomena.

Full study of mesoscale data synthesis and model initialization will require experimentation with more complete wind data sets as well as mesoscale mass and moisture observations.

6. REFERENCES

1. Bauer, K.G., 1976: A comparison of cloud motion winds with coinciding radiosonde winds. *Mon. Wea. Rev.*, 104, 922-931.

2. Bettge, T.W. and D.P. Baumhefner, 1980: A method to decompose the spatial characteristics of meteorological variables within a limited domain. *Mon. Wea. Rev.*, 108, 843-854.

3. Hoke, J.E. and R.A. Anthes, 1976: The initialization of numerical models by a dynamic initialization technique. *Mon. Wea. Rev.*, 104, 1551-1556.

4. Houghton, D.D., D.K. Lee and C.B. Chang, 1979: Numerical Model initialization with sub-synoptic-scale satellite cloud-wind data. Fourth Conference on Numerical Weather prediction, Oct. 29 - Nov. 1, 1979, Preprint volume., American Meteorological Society, Boston, pp. 16-23.

5. Kreitzberg, C.W., 1977: Progress and problems in regional numerical weather prediction. Research Paper, Dept. of Physics and Atmospheric Science, Drexel Univ., Philadelphia, 27 pp.

6. Maddox, R.A., 1980: An objective technique for separating macroscale and mesoscale features in meteorological data. *Mon. Wea. Rev.*, 108, 1108-1121.

7. Perkey, D.F., 1976: A description and preliminary results from a fine-mesh model for forecasting quantitative precipitation. *Mon. Wea. Rev.*, 104, 1513-1526.

8. Tarbell, T.C., T.T. Warner and R.A. Anthes, 1981: An example of the initialization of divergent wind component in a mesoscale numerical weather prediction model. *Mon. Wea. Rev.*, 109, 77-95.

9. Wilson, T.A. and D.D. Houghton, 1979: Mesoscale wind fields for severe storm situation determined from SMS cloud observations. *Mon. Wea. Rev.*, 107, 1198-1209.

5.8

IMPACT OF MESOSCALE SATELLITE WIND DATA ON NUMERICAL MODEL SIMULATIONS

Dong Kyou Lee and David D. Houghton

Department of Meteorology
University of Wisconsin
Madison, WI 53706

1. INTRODUCTION

The technology of meteorological observing systems has developed to the point where extensive data for mesoscale phenomena is becoming available. Satellite sensing can now provide high spatial resolution information for temperature, moisture and wind fields. Special observing programs such as SESAME are producing comprehensive data sets based on both remote sensing systems and conventional systems in high resolution networks.

The challenge remains to use this data for the analysis and prediction of mesoscale phenomena. Deterministic numerical prediction models are an important tool for this task. The models provide a capability to merge and assimilate the data derived from numerous sources as well as to assess forecast impacts. Model experimentation using actual mesoscale observations is in the initial stages. Progress in this area of research is difficult because the mesoscale models themselves are in a state of development and fundamental aspects such as the formulation for important sub-grid scale effects is still not adequately resolved.

In this study, a set of comparative experiments are performed with a comprehensive mesoscale numerical model in order to isolate impacts of mesoscale wind data used in the initial conditions. Several insertion procedures are tested and numerous diagnostic methods are used for forecast impact assessment. It is necessary to include diagnostics for determining the nature of fundamentally unbalanced motions characteristic of some mesoscale phenomena. Defining the most meaningful measures for isolating this type of motion will require improved understanding of the structure and dynamics of mesoscale systems. This study is preliminary because of the limited mesoscale wind data available and the restriction to a single case study.

2. SYNOPTIC CASE AND MESOSCALE DATA

The case study involves convective systems in the eastern portion of a developing trough moving into the south central region of the United States. At 1800 GMT 20 May 1977 there is a broad area of low level southerly wind coming into the region of interest. At the middle and upper levels, a general flow of southwesterly

diffluent winds accompanies a jet approaching the area studied. At levels below 700 mb there is a broad area of moisture drawn in by the southerly flow. A major thunderstorm band is developing in northwestern Texas. By 0000 GMT 21 May the low level flow has increased in speed and the moist layer is deeper. The jet stream is now centered in the area studied and strong convective thunderstorm bands exists in the southwestern area of this region. Fig. 1 shows 1800 GMT synoptic features at 700 mb analyzed from special upper air sounding data (SESAME) which were available at 17 stations for this time over the south central United States.
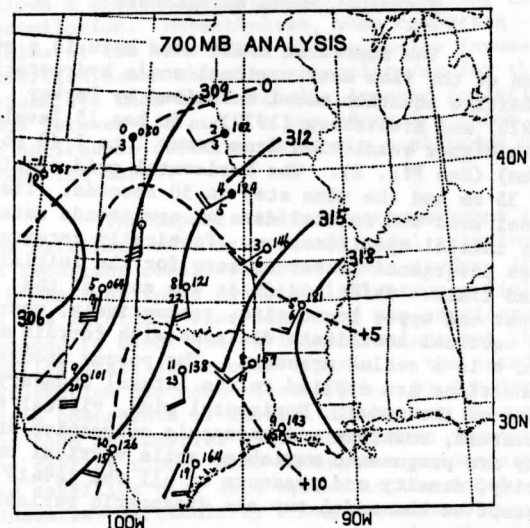

Figure 1. 700 mb height and temperature analysis at 1800 GMT.

The satellite wind data used in this study are averaged wind vectors obtained from four high-resolution SMS visible images from 1742 to 1800 GMT on May 20 in the Kansas, western Missouri, Oklahoma and north central Texas area. The data consisted of 287 low level wind vectors produced by the McIDAS of the Space Science and Engineering Center at the University of Wisconsin. The wind vectors were obtained from low level cumulus clouds with top heights ranging about from 700 to 900 mb. The vertical wind shear was examined at low levels (900 to 700 mb) from

soundings at the four stations which are located within the satellite wind domain. It was concluded from the results that using layer-averaged satellite wind data in the 900-700 mb layer would not introduce unreasonably large changes in the vertical shear characteristics. Hourly surface observations were reported at 36 stations in the area over which attempts were made to determine satellite wind vectors. There was some similarity of the surface flow field to the satellite winds. However, the vorticity and divergence patterns do not correspond well. The magnitudes of mesoscale vorticity and divergence were considerably larger in the satellite data than in the surface data.

Satellite and surface wind data were interpolated to model grid points using an objective analysis scheme developed by Barnes (1973). Before the Barnes method was selected to provide the grid point data set, several objective analysis methods were tested on the satellite wind data set to determine sensitivity to analysis procedure (See Houghton et al. (1979)). For initialization of the numerical model, the rotational (non-divergent) component of wind alone as well as total wind data was used. Rotational component winds were obtained using an iterative scheme developed by Shukla and Saha (1974). Hereafter the combined satellite and surface wind data is referred to as the satellite wind data.

3. NUMERICAL MODEL EXPERIMENTS

The numerical model used here is a version of the fine mesh regional scale hydrostatic primitive equation model described by Perkey (1976) and Kreitzberg (1977). It has 15 levels with higher resolution from level 1 to 7 (0 to 3 km) (See Fig. 2). The horizontal grid spacing is 35 km and the time step is 50 seconds. The model uses NMC initial data or rawinsonde data for initial specification. Vertically integrated mass divergence is set to zero for the initial wind field. dh/dt and dπ/dt are zero at the lower and upper boundaries, respectively, where h is vertical coordinate distance with terrain effect and π is a scaled pressure. The porous sponge conditions are applied in the lateral boundary zone of the model. Horizontal wind, virtual temperature, moisture and mesoscale convective activity are prognostic variables while vertical velocity, density and pressure at all the levels except at the model top are diagnostic variables.

Four 6-hour simulation experiments are made starting from 1800 GMT. The first, referenced the "control" case, is initialized using 6 h forecast fields from a coarser mesh model run (140 km horizontal grid) that used 1200 GMT rawinsonde information as input. The second, denoted the "initially imposed insertion" case, is handled identically to the first except for the initial time insertion of the satellite wind data set into a sub-domain of the model. The third, termed the "gradually imposed insertion" case, is identical to the second except for gradual insertion of the satellite wind data set. The gradual insertion is done updating continuously from 1800 to 1830 GMT (0 to 1/2 h forecast) with a linearly combined wind obtained from the satellite wind data set and the existing model wind
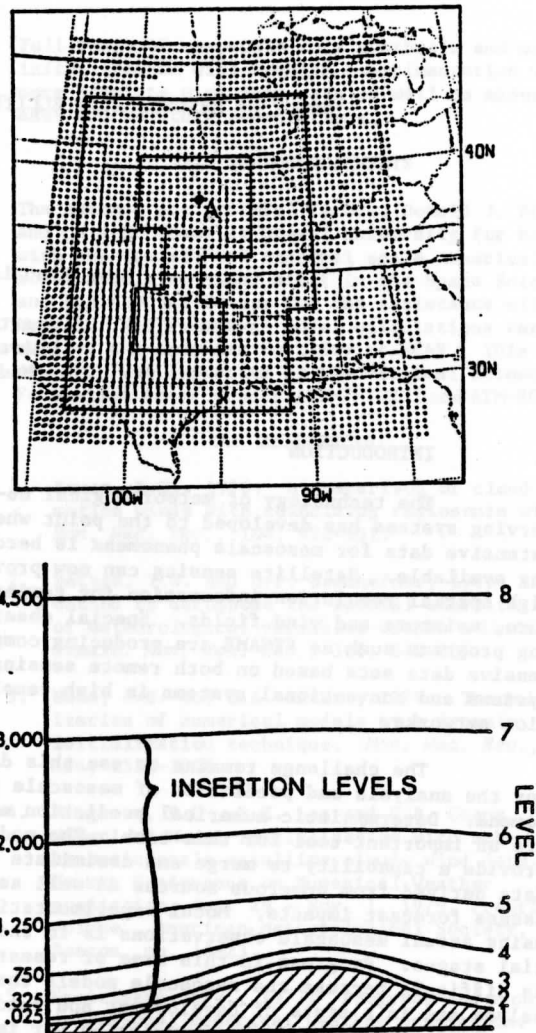

Figure 2. Horizontal (top panel) and vertical (lower panel) model domains for insertion of satellite wind data. In the top panel, grid point vectors at the 2 km height are shown. The inner-most enclosure is the insertion area. The transition boundary zone is between the two solid perimeter lines within the grid point region. The grid point A marks the location at which time series data are collected. In the lower panel, only the lower portion of the 15 layer model is depicted.

field. The updated value is given by α (satellite wind) + (1-α) (model wind) where α is a weighting factor increasing from zero at 1800 GMT linearly to unity at 1815 GMT and then decreasing linearly to zero at 1830 GMT. The fourth, referred to as the "gradually imposed rotational wind insertion" case, is exactly identical to the third except using only the rotational component of satellite wind data set. The initial mass and pressure fields in both initially and gradually imposed insertion cases are same as in the control case. The gradual insertion technique in this study is equivalent to the nudging process in the dynamical initialization developed by Hoke and Anthes (1976).

172

The domain of insertion along with the horizontal grid and vertical resolution is shown in Fig. 2. The model domain ranges from (north) latitudes 27.18 to 45.94 degrees and from (west) longitudes -104.83 to -84.02 degrees. For the insertion cases, a special transition boundary zone is made to reduce the discontinuities in the wind fields at insertion boundaries. It is a band of 9 grid increments width surrounding the insertion area. Model data is replaced with insertion data from levels 1 to 7. Surface wind observations are used at level 1, satellite wind data are used at levels 5, 6 and 7, and averaged values of surface and satellite wind data replace the model winds at levels 2, 3 and 4 in the insertion area. Levels 5 to 7 (1.25 to 3 km) correspond closely to the 900 to 700 mb height layer originally assigned to the satellite grid vectors.

After all initial data has been assembled in the model, an adjustment is made in the horizontal velocity field so that vertical motion is zero at the upper boundary. This minimizes the initial excitation of spurious external wave modes. This is done by an iterative procedure making corrections at all levels and is applied to the entire model domain including the region where the special observational wind data has been added in the insertion cases. In the insertion region the adjustment procedure suppresses slightly amplitudes of divergence in the satellite wind data but it does not effect the phase and patterns of the small scale features. At upper levels it results in adding divergence of opposite sign to that in the satellite wind data at lower levels. Contributions to the vorticity and divergence fields from the surface wind data is minimal.

Model data outputs were made every 1/2 h for all prognostic and diagnostic variables as well as parameters involved with precipitation. Time series of data output every time step at several grid points selected were also made for important variables. Most of discussions about model solutions hereafter are given at the 2 km level unless otherwise mentioned. This 2 km level (approximately 800 mb) is in the middle of the three levels (level 5, 6 and 7) where satellite wind data was added.

4.   MODEL RESULTS

The model dynamics behaved in a consistent manner for all the cases responding stably to the insertion techniques. The control case showed that with 35 km horizontal grid spacing the model would develop smaller scale features (up to 10 Δ, where Δ is horizontal grid spacing) from larger scale initial data, which were of similar scale to some features in the satellite wind data. The primary impact of the inserted data is to alter the amplitude of mesoscale features developed in the control case. In addition, initial patterns and phases of the rotational and divergent component in the satellite wind data showed some persistence in the forecasts. All of these components had characteristics of internal modes in the model solutions. The model made generally realistic forecasts for the major convective activity that developed in the area. The mid level vertical motion fields were generally consistent with the low level divergence patterns and do not need to be discussed separately.

For the control case the initial larger scale vorticity patterns are persistent for the entire time period while the smaller scale features which are resolved by higher horizontal grid resolution begin to appear at about 2.5 h. The initial patterns of larger scale divergence also show some persistence and smaller scale divergence in the control solution begin to appear at 1/2 h indicating more sensitivity of the model to the divergent components. For all insertion cases, vorticity patterns introduced by the satellite data insertion change gradually in time with slowly decreasing amplitudes for the entire forecasts. Propagation of the vorticity fields generally is similar to low level wind flow direction which is southerly in the southern part of the insertion area and southwesterly in the northern part. Small scale divergences in the satellite wind data disappear rapidly in the model solutions and the dominant larger scale positive divergence field in the insertion data starts to break down into small scale features at approximately 2 h while at the same time new small scale patterns start to develop in that area.

The various wind data assimilation techniques used in the insertion cases resulted in larger changes in the amplitude than in the pattern and phase of wind fields. After the 1/2 h of gradual insertion, local extrema of vorticity and divergence are slightly smaller than those in the initial satellite wind data. This implies that gradually imposed insertion allows a smoothing in the solutions during the assimilation. Nevertheless, when comparing fields at the same time, the gradually imposed insertion cases show larger amplitudes for these parameters than the initially imposed insertion case between 1/2 and 3 h but after 3 h there are no noticeable differences of the amplitudes between the cases.

The impact of divergent component in the satellite wind data on the model solution is an important consideration in this study. After 1 h the amplitudes of initial divergence fields in the satellite wind data area are considerably reduced to about 30% of initial values but the smaller scale divergence signals in the satellite information has lost after 1/2 h. By 3 h larger scale components of initial divergence disappear and then new smaller scale components develop for the rest of time. Also divergence components of the satellite wind data spread to the model boundaries particularly along a northeast-southwest axis which approximates the direction of flow at upper tropospheric levels.

In order to examine in more detail characteristics of divergent component of the satellite wind information, divergence fields for the control and the initially imposed insertion cases are decomposed using a digital filter. Bettge and Baumhefner (1980) discussed digital filtering techniques and applications. Waves longer than 10 Δ which dominate in the control case and waves within the bandwidth from 4 to 10 Δ which correspond to smaller scale features in the satellite data are distinguished in the decomposition process. The former is referred to as smoothed scale field. Fig. 3 shows the decomposition results for divergence in the insertion
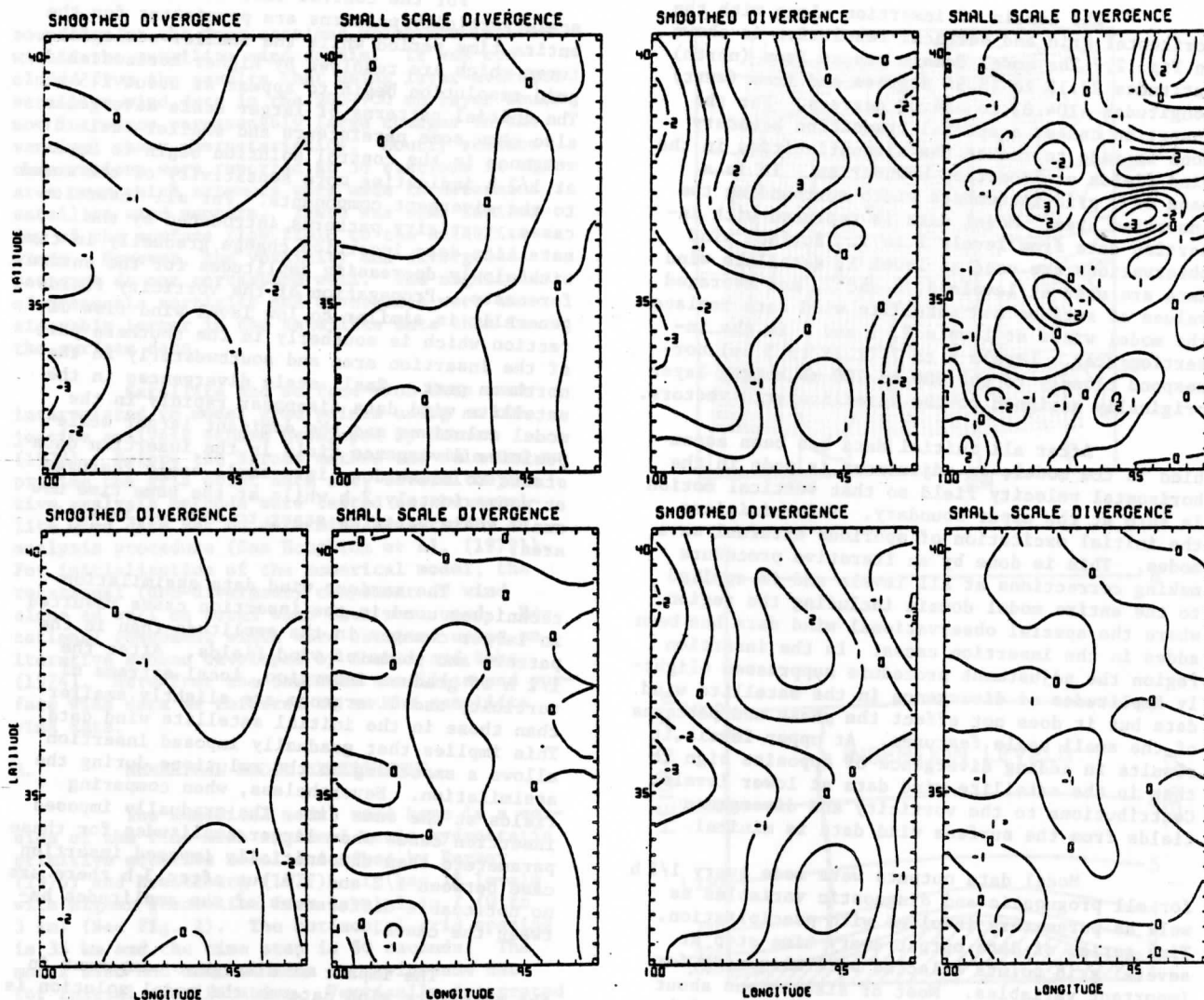
Figure 3. Decomposition results for divergence at 0 h (upper panels) and 1/2 h (lower panels) model forecasts at 2 km in the control case (left 4 panels) and in the initially imposed insertion case (right 4 panels). Units are 10^{-5} s^{-1}. Contour interval is 1 x 10^{-5} s^{-1}.

area at 0, 1/2, 3 and 6 h for both cases. This decomposition result reveals very well the phenomena of divergence which were discussed earlier. The small scale divergence fields at 6 h have the same phases and patterns in the convective activity area in both cases but in the insertion case the amplitudes are much reduced. In contrast, the smoothed divergence fields at 6 h for the insertion case show different phases and patterns from those for the control case. Differences for both scales between the two cases are more obvious in the 6 h solutions than in the 3 h solutions.

It is useful to consider general and broader scale features of the simulation process by examining total circulation and net outflow of the entire data insertion area. To do this, the insertion area-mean vorticity and divergence are computed at levels 6 and 9 in the satellite data insertion area. These values calculated at level 6 are plotted with time in Fig. 4. It is evident that in the insertion cases general changes are

made in the model solution of the control case. Total circulations of the insertion cases tend to converge slowly to that of the control case. However, the net inflow produced in the insertion cases becomes the same as the control at about 2.5 h and thereafter shows more net inflow than the control. At level 9 the values of divergence are shown with opposite effect to those at level 6 indicating the presence of internal mode structure in the mesoscale features introduced from the satellite wind data insertion. This aspect is also revealed well in the vertical motion.

For the insertion cases the satellite wind data produced pressure changes in the model solutions. Pressure difference fields between the insertion cases and the control case, respectively, are analyzed to examine characteristics of pressure response to the insertion data. These difference fields reveal both the internal and external modes in the mesoscale features produced. Also these difference fields correspond
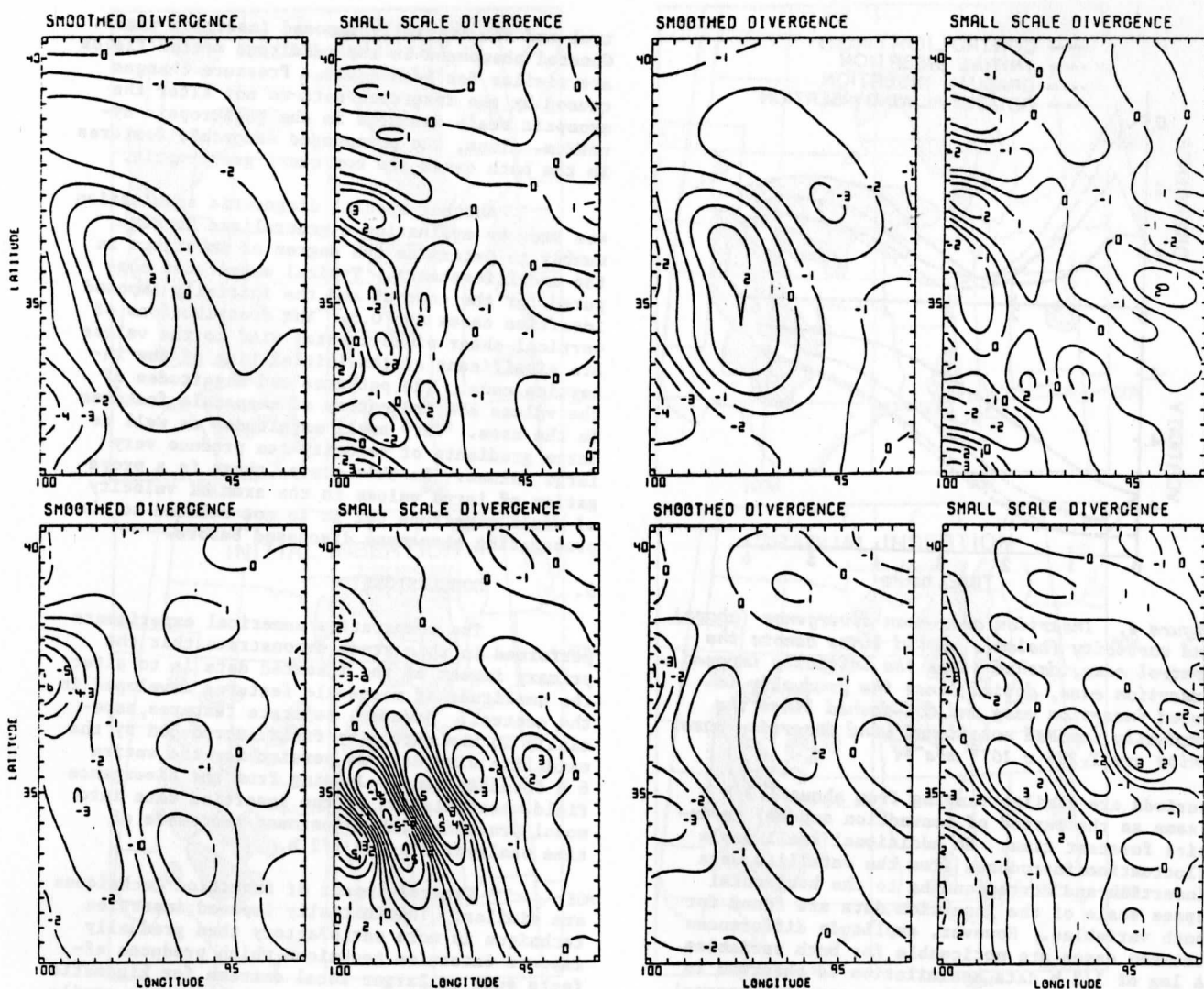
SMOOTHED DIVERGENCE   SMALL SCALE DIVERGENCE   SMOOTHED DIVERGENCE   SMALL SCALE DIVERGENCE

SMOOTHED DIVERGENCE   SMALL SCALE DIVERGENCE   SMOOTHED DIVERGENCE   SMALL SCALE DIVERGENCE

Figure 3. (Continued) Same as shown on the previous page except at 3 h (upper panels) and 6 h (lower panels).

to initial larger scale component of divergence fields indicating fundamental relation in the simple form of atmospheric governing equation. The vertical structure of these pressure differences fields reveals internal modes in the insertion cases. In the gradually imposed insertion cases there is much more significant gravity wave activity of Lamb wave type (external mode) which oscillates for the first 3 h of forecasts.

General effects of the data insertion on precipitation forecasts are examined. Fig. 5 shows comparisons of National Weather Service radar summary at 1935 GMT with convective precipitation rates at 1.5 h for the cases except the gradually imposed rotational wind insertion case which has results similar to the gradually imposed insertion case. For the first few hours the convective precipitation rates in the data insertion area correspond better to the radar summary in terms of location for the insertion cases than the control case and thus shows a favorable impact. This effect results from the broad area of low level positive divergence

introduced from the satellite data. In the later forecast period this initial low level positive divergence also affects convective activity in the southwestern area of the region studied and reduces its intensity showing an unfavorable impact of the insertion data. Tarbell et al.(1981) reported from an initialization experiment with a mesoscale numerical model that use of diagnosed divergence derived from the omega equation improved the first 3 h forecasts but the unbalanced data with observed divergence did not improve the forecasts.

Additional information about the features in the control case and the model response to the satellite data is obtained analyzing time series data at several grid points. Fig. 6 shows time series of pressure and vertical velocity at level 6 at a point (denoted as A in Fig. 2) in the insertion area for the control and the insertion cases. The gradually imposed rotational wind insertion case is not shown in the figure because of its similarity to the gradually imposed insertion case. For all cases fluctuation
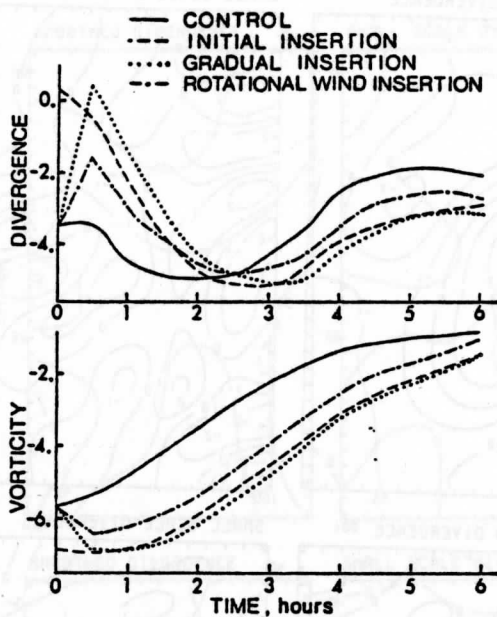
Figure 4. *Insertion area-mean divergence (above) and vorticity (below). Solid lines denote the control case, dashed lines the initially imposed insertion case, dotted lines the gradually imposed insertion case and dot-dashed lines the gradually imposed rotational wind insertion case. Units are 1.225 x 10⁻⁴ m²s⁻¹.*

periods are similar ranging from about 1/3 h (same as the period of convection scheme) to entire forecast time. No additional small scale fluctuations introduced from the satellite data insertion and corresponding to the horizontal space scale of the insertion data are found for both variables. However, amplitude differences between cases are noticeable for both variables. A lag of 1/2 h data assimilation is observed in the gradually imposed insertion case but general impact of insertion techniques are similar.

Adjustment processes of the model to the insertion are inferred from the characteristics of divergence and pressure fields. Persistence of the larger scale component of initial divergence up to 3 h forecasts of the insertion cases indicates an evident adjustment process with a time scale 3 h (i.e., 1/f where f is the Coriolis parameter). Area-mean divergence values in the insertion area and pressure oscillations in the gradually imposed insertion cases also indicate the same time scale. The disappearance of the smaller scale divergence component by the 1/2 h forecast time shows another adjustment process with 1/2 h or shorter time scale.

A diagnostic vertical motion equation was solved to partition the forecast motion into quasi-geostrophic and non quasi-geostrophic components. The vertical motion equation was formulated in the z-coordinate by combining geostrophic vorticity equation and the first law of thermodynamics. The diagnostic equation did not include diabatic heating term. Dominant forcing in the equation is differential relative geostrophic vorticity advection which is characterized by pressure fields. The diagnostic equation is applied to model solutions for both the con-

trol and the initially imposed insertion cases. General phenomena in the resultant motion fields are similar for both cases. Pressure changes caused by the insertion data do not alter the synoptic scale features in the geostrophic dynamics. Thus, the pronounced mesoscale features in the both cases are non quasi-geostrophic.

Another special diagnostic examination was made by evaluating a generalized Rossby number to determine the degree of imbalance in the model forecasts. Typical magnitudes computed for the control and the initially imposed insertion cases are 0.5. The contributions of vertical shear of horizontal wind to the values are significant at the initial time of the insertion case. The patterns and magnitudes of the values are indicative of mesoscale features in the area. Very small magnitudes as well as large gradients of velocity can produce very large values. In this study, there is a propagation of large values in the area of velocity of small magnitude but it is not related to the propagating phenomena discussed before.

5.   CONCLUSIONS

The comparative numerical experiments performed in this study demonstrate that the primary impact of the inserted data is to alter the amplitude of mesoscale features developed in the control. However, separate features, especially in the vorticity field introduced by the satellite wind data do persist for the entire 6 h forecast time. Judging from the divergence field, assimilation of the insertion data into model proceeds with adjustment processes of time scales of 3 h and 1/2 h.

General impact of insertion techniques are similar. The initially imposed insertion technique is more satisfactory than gradually imposed insertion technique which produces effects such as larger local extrema for kinematic parameters and an extra spurious pressure oscillation. The gradually imposed rotational wind case results are similar to those using the total wind.

It is not possible to show overall improvement of model performance due to inclusion of this satellite wind data because of inadequate verification data and limitations in the insertion data and in the experimental design. Nonetheless, there are noticeable differences in the insertion area of the 1 to 3 h precipitation forecasts between the experimental cases.

Various diagnostic studies considered serve to demonstrate the complexity of determining the forecast impacts. Scale decomposition and time series analysis are shown to be useful techniques. Defining the most meaningful measures of determining unbalanced motion characteristics requires understanding of the structure and dynamics of mesoscale systems.

Full study of mesoscale data synthesis and model initialization will require experimentation with more complete wind data sets as well as mesoscale mass and moisture observations.
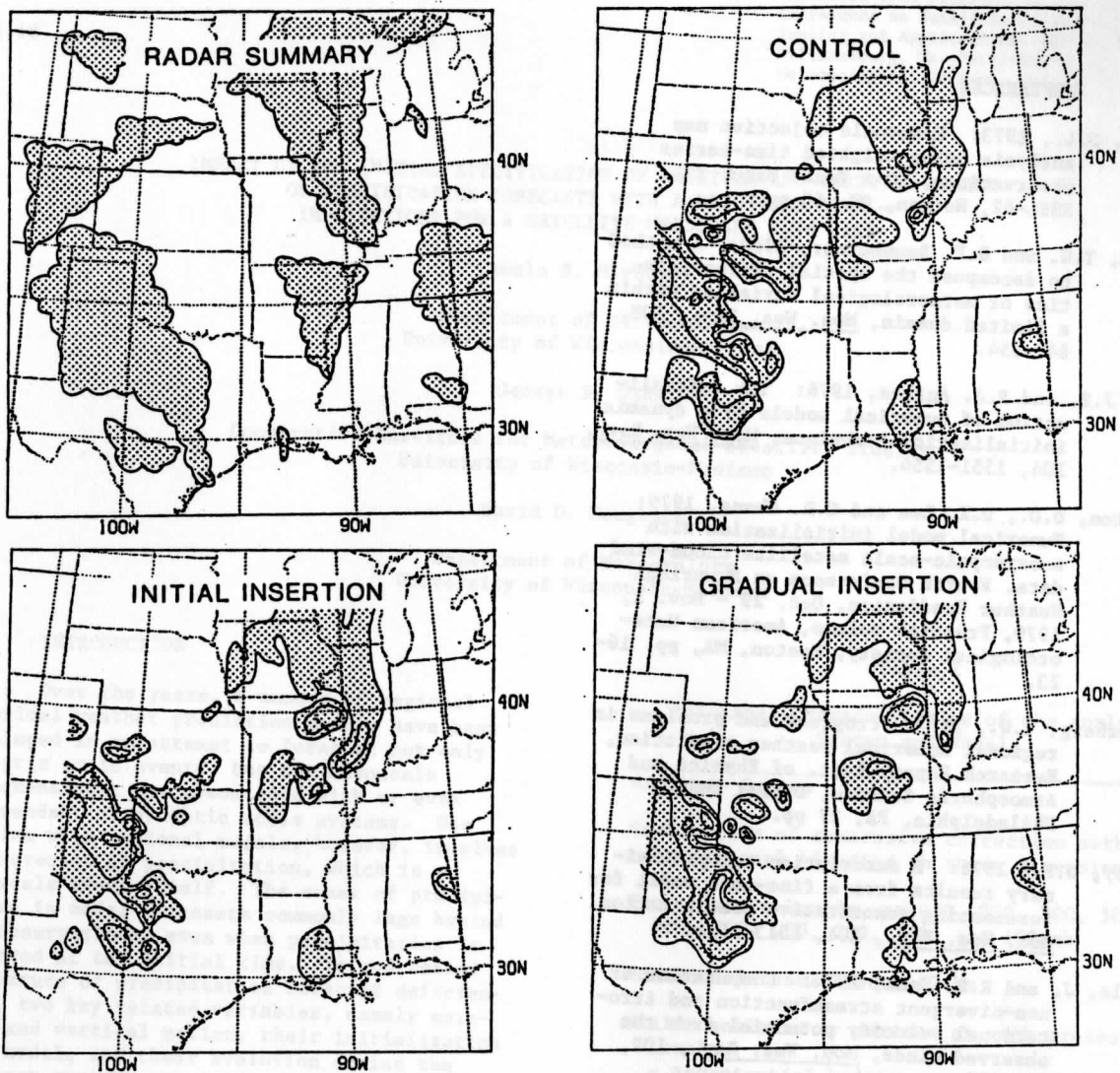
Figure 5. Comparison of radar summary at 1935 GMT with the 1.5 h convective precipitation rate forecasts for the control, the initially imposed insertion and the gradually imposed insertion cases. The radar echo regions and forecast convective precipitation rates are shaded. Units and contour intervals of forecast fields are 10^{-4} mms^{-1} and 4×10^{-4} mms^{-1}, respectively.
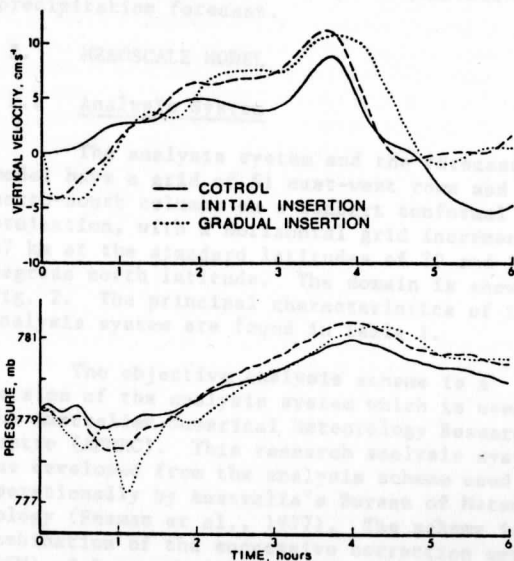

Figure 6. Time series of vertical velocity (above) and pressure (below) at 2 km for the grid point A which was shown in Figure 2. The solid lines are the control case, the dashed lines the initially imposed insertion case and the dotted lines the gradually imposed insertion case.

6.   ACKNOWLEDGMENTS

7.   REFERENCES

Barnes, S.L., 1973: Mesoscale objective map
          analysis using weighted time-series
          observations, NOAA Tech. Memo. ERL
          NSSL-62, Norman, OK, 60 pp.

Bettge, T.W. and D.P. Baumhefner, 1980: A method
          to decompose the spatial characteris-
          tics of meteorological variables within
          a limited domain, Mon. Wea. Rev., 108,
          843-854.

Hoke, J.E. and R.A. Anthes, 1976: The initiali-
          zation of numerical models by a dynamic
          initialization technique, Mon. Wea. Rev.,
          104, 1551-1556.

Houghton, D.D., D.K. Lee and C.B. Chang, 1979:
          Numerical model initialization with
          subsynoptic-scale satellite cloud-wind
          data, Fourth Conference on Numerical
          Weather Prediction, Oct. 29 - Nov. 1,
          1979, Preprint volume, American Mete-
          orological Society, Boston, MA, pp. 16-
          23.

Kreitzberg, C.W., 1977: Progress and problems in
          regional numerical weather prediction,
          Research Paper, Dept. of Physics and
          Atmospheric Science, Drexel Univ.,
          Philadelphia, PA, 27 pp.

Perkey, D.F., 1976: A description and prelimi-
          nary results from a fine-mesh model for
          forecasting quantitative precipitation,
          Mon. Wea. Rev., 104, 1513-1526.

Shukla, J. and K.R. Saha, 1974: Computation of
          non-divergent streamfunction and irro-
          tational velocity potential from the
          observed winds, Mon. Wea. Rev., 102,
          419-425.

Tarbell, T.C., T.T. Warner and R.A. Anthes, 1981:
          An example of the initialization of
          divergent wind component in a mesoscale
          numerical weather prediction model,
          Mon. Wea. Rev., 109, 77-95.

IMPACT OF THE INITIAL SPECIFICATION OF MOISTURE AND VERTICAL MOTION
ON PRECIPITATION FORECASTS WITH A MESOSCALE MODEL--
IMPLICATIONS FOR A SATELLITE MESOSCALE DATA BASE

Pamela E. Mlynczak

Department of Meteorology
University of Wisconsin-Madison

George R. Diak

Cooperative Institute for Meteorological Satellite Studies
University of Wisconsin-Madison

David D. Houghton

Department of Meteorology
University of Wisconsin-Madison

1. INTRODUCTION

Over the years, a number of regional
numerical weather prediction models have been
developed in an attempt to forecast not only
synoptic scale events, but the mesoscale
phenomena that are associated with or even
independent of synoptic scale systems. One
problem with regional models, however, involves
the forecast of precipitation, which is a
mesoscale event itself. The onset of precipi-
tation in model forecasts commonly lags behind
the observations, even when precipitation is
observed at the initial time. To understand
the nature of precipitation forecast deficien-
cies, two key related variables, namely mois-
ture and vertical motion, their initialization
in a model, and their evolution during the
forecast must be examined. In this study,
model simulations with modifications of the
initial specifications of moisture and vertical
motion will be examined to determine the
relative impact of the mesoscale component of
each parameter on the subsequent quantative
precipitation forecast.

2. MESOSCALE MODEL

2.1 Analysis System

The analysis system and the forecast
model have a grid of 51 east-west rows and 61
north-south columns on a Lambert conformal
projection, with a horizontal grid increment of
67 km at the standard latitudes of 20 and 50
degrees north latitude. The domain is shown in
Fig. 2. The principal characteristics of the
analysis system are found in Table 1.

The objective analysis scheme is a
version of the analysis system which is used by
the Australian Numerical Meteorology Research
Centre (ANMRC). This research analysis system
was developed from the analysis scheme used
operationally by Australia's Bureau of Meteo-
rology (Seaman et al., 1977). The scheme is a
combination of the successive correction method
(SCM) of Cressman (1959) and the variational

Table 1

Principal Characteristics of the Analysis System and Model

Analysis System

Combination of successive correction method and
variational blending in three dimensions

Ten pressure levels, p=1000, 850, 700, 500,
400, 300, 250, 200, 150, and 100 mb

Horizontal resolution: 67 km

Fields analyzed or derived at each pressure
level:
  - geopotential height
  - temperature
  - dewpoint
  - horizontal wind components
  - streamfunction

Forecast Model

Primitive equations model in σ-coordinates
Ten vertical levels at σ=0.09, 0.19, 0.29, ...,
0.99
Horizontal resolution: 67 km
Staggered horizontal grid (Arakawa "C" grid)
Semi-implicit time differencing (Δt=5 min)
Similarity theory surface layer
Stability-dependent vertical diffusion of
  momentum, heat, moisture above surface layer
  through depth of boundary layer
Surface shortwave and longwave flux modified by
  cloudiness
Surface energy balance equation
Large-scale precipitation
Kuo-type convective parameterization
Updated boundary conditions

blending technique of Sasaki (1958, 1970). The
research version contains three-dimensional
variational blending of geopotential. Mills
(1981) presents a qualitative discussion of the
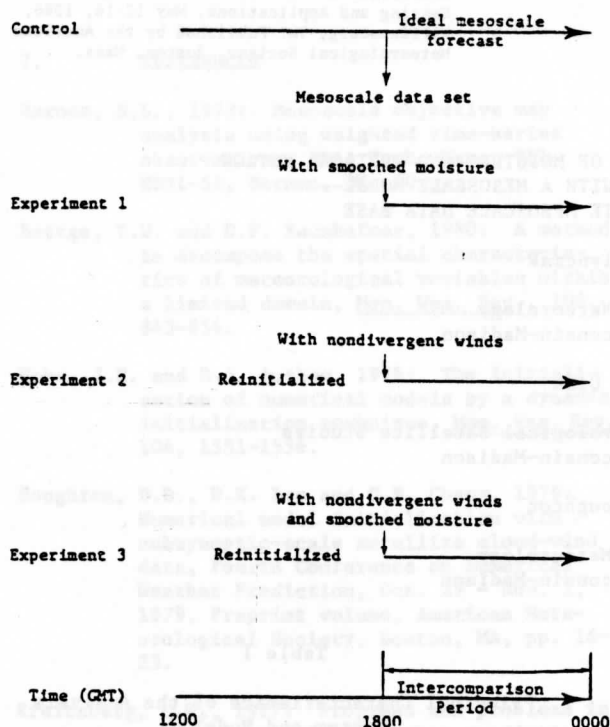analysis sequence.

Fig. 1. Schematic summary of experimental design. The duration for each simulation is indicated by horizontal arrows.

2.2 Forecast Model

The forecast model was developed from the Australian Region Primitive Equations (ARPE) model (McGregor et al., 1978). The subsynoptic Scale Model (SSM) of the Space Science and Engineering Center at the University of Wisconsin-Madison used in this study is an adaptation of the ARPE model to the North American region. In this adaptation on Kuo-type convective parameterization (Kuo, 1965, 1974) and a comprehensive planetary boundary layer scheme were incorporated into the model. Also, a finite differencing scheme discussed by Corby et al. (1972) which lessens truncation effects in regions of steep topography has been added. Further characteristics are found in Table 1.

3. EXPERIMENTAL DESIGN

Four simulations are made with the SSM to determine the impact of the initial moisture and vertical motion fields on the evolution of the precipitation forecasts. These are a control forecast 12-hour simulation that begins at 1200 GMT 6 March 1982 and three experiment simulations with modifications to the moisture and vertical motion fields incorporated at 1800 GMT. The experiment forecasts from 1800 GMT are compared to the second half of the control forecast. The experimental design is given in Fig. 1.

The 12-hour control simulation begins at 1200 GMT 6 March 1982 and develops precipitation by 1300 GMT. The model is still producing precipitation at 1800 GMT the time a data set is extracted for use in the three experiments.
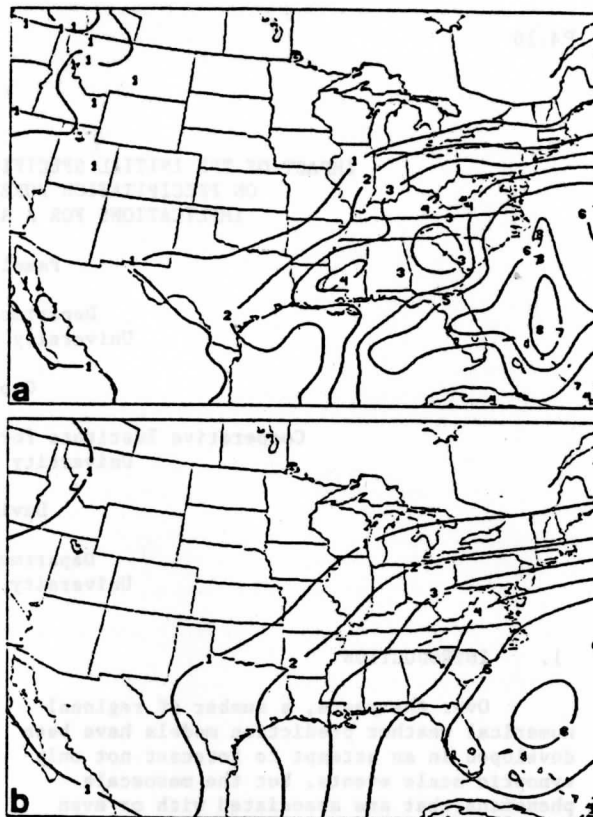

Fig. 2. Mixing ratio from the control forecast at 1800 GMT for the sigma level of 0.69; a) unsmoothed, b) smoothed. Contour interval is 1 g kg^{-1}.

Beginning at this time, changes in the precipitation rates and accumulations due to changes in the initial specifications will be most accentuated. The six-hour control forecast from 1800 GMT 6 March to 0000 GMT 7 March 1972 provides the "ideal forecast"—one that contains mesoscale moisture and vertical motion information from beginning to end.

Experiment 1 is run like the control forecast, except that at 1800 GMT, smoothed moisture fields replace the mesoscale moisture fields in the model. The moisture fields are smoothed to make them representative of fields that would be obtained from analyzed radiosonde data, usually considered to be at the synoptic scale. Fig. 2 shows the original and the smoothed mixed ratio fields for the sigma level of 0.69. Experiment 1 provides the precipitation forecast for the initial state with only a synoptic scale moisture field.

Experiment 2 is like the control forecast except that the initial wind fields are constrained to be nondivergent at 1800 GMT. The nondivergent wind components are derived from the model winds extracted from the control forecast data set and are inserted into the model. All of the other variables remain unchanged. Because the winds are nondivergent, the initial vertical motion is suppressed, particularly away from areas of significant topography (Fig. 3). Experiment 2 shows the effect of a nondivergent initialization of winds on the subsequent quantitative precipitation forecast.
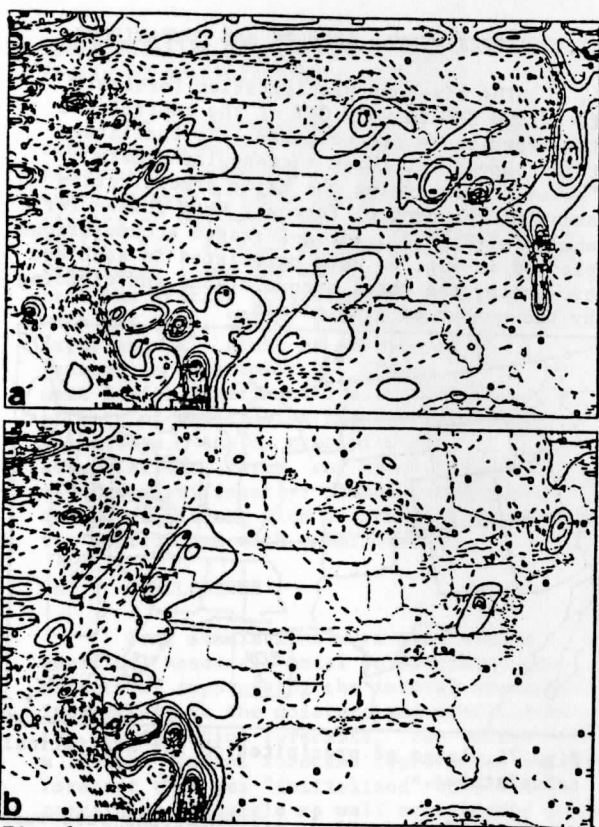
Fig. 3. Vertical motion σ̇ at 1800 GMT for sigma level of 0.49; a) control, b) experiment 2. Negative values (upward motion) are solid. Contour interval is 2×10^{-6} s^{-1}.

Fig. 4. 500-mb geopotential heights (m) and 500-mb relative vorticity (contour interval 40×10^{-6} s^{-1}, negative values dashed) at 0000 GMT; a) observed, b) control.

Experiment 3 is a combination of Experiments 1 and 2, containing both the initial smoothed moisture and nondivergent wind fields. This experiment is the most representative of a forecast beginning with synoptic analyses. It should be noted, however, that mesoscale and synoptic scale information from the six-hour control forecast remained in the height and temperature fields.

4.   CONTROL CASE OF 6 MARCH 1982

The purpose of this research to study the changes made to a precipitation forecast due to modifications of the initial moisture and vertical motion fields is achieved by comparing simulation of the three experiments to the control forecast. The performance of the control itself is discussed very briefly here, although its accuracy in terms of the observations is not central to the analysis.

The model performed well at 500-mb level, as shown in Fig. 4. The forecasted trough over the central U.S. is slightly behind that of the analysis, but the intensity is simulated well. The forecast, however, does not capture the short wave trough observed west of Florida. The forecast of mean sea level pressure was excellent, with accurate placement and strength of the features (not shown).

The precipitation forecast from the model was not as satisfactory as the height and mean sea level pressure forecasts. The model's placement of copious rainfall east of Virginia
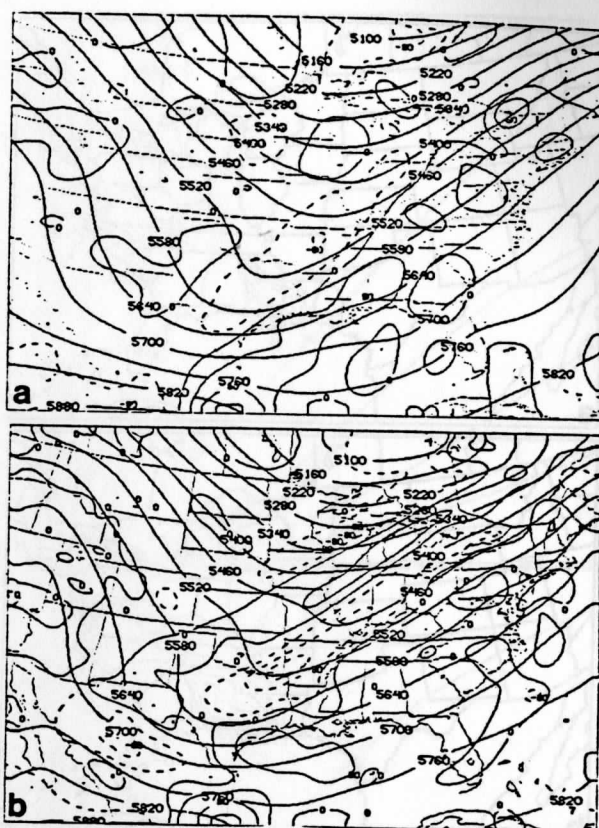
and North Carolina seems accurate, based upon comparing Figs. 5 and 6 with radar maps (not shown). Precipitation output from the model is shown in hundredths of centimeters. The development of the precipitation area over Ohio and Pennsylvania lagged four hours behind the observations, yet the model greatly over-forecasted the amounts in this region, producing as much as 2.00 cm (0.75 in.) while the observations were all less than 0.25 in. The model's performance in the Gulf region compared much less favorably to the observations than did the forecast off the East Coast and over the northeastern United States. The precipitation band observed over Louisiana, Mississippi, and Alabama was not forecasted at all. No rainfall greater than 0.25 in. was forecasted over the land. Instead, the model generated precipitation out over the Gulf of Mexico, but not until 1700 GMT. The validity of this feature is questionable because of the lack of verification data; however, satellite imagery did suggest that precipitation had developed here earlier before moving eastward. The forecasted feature, however, remained stationary.

It is unfortunate that the precipitation forecast produced by the control simulation was not more accurate. The purpose of this study, however, is to discuss changes in the forecasts brought about by modifications to the initial conditions. It is expected that the comparisons between the control and the experiments will be meaningful, regardless of the simulation deficiencies in the control forecast.
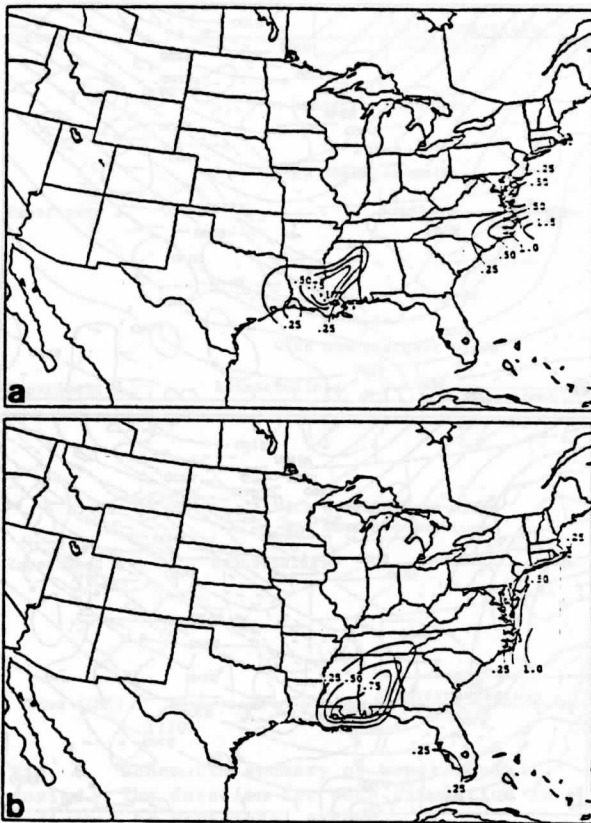
Fig. 5. Six-hour observed precipitation accumulations (in.) ending at (a) 1800 GMT, (b) 0000 GMT.
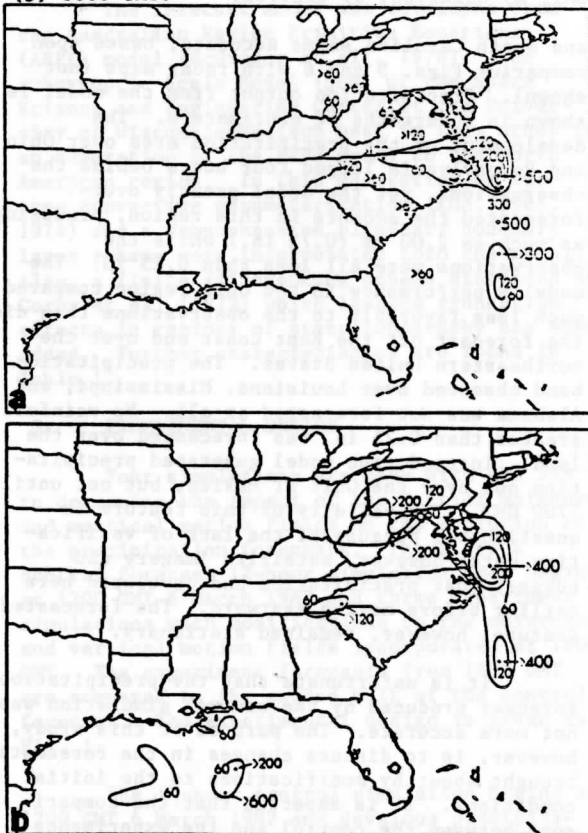

Fig. 6. Six-hour precipitation accumulations (hundredths of cm) from the control forecast ending at (a) 1800, (b) 0000 GMT.

5. EXPERIMENTAL RESULTS AND COMPARISONS

The six-hour precipitation forecasts from 1800 GMT to 0000 GMT of the control and the experiments are compared. To facilitate this comparison, three rectangular domain "boxes" encompassing the major precipitation areas of the control forecast were chosen for analysis (Fig. 7). Area-averaged accumulations, plotted in Fig. 8, were calculated in each box by summing the total accumulations and dividing by the number of grid points.
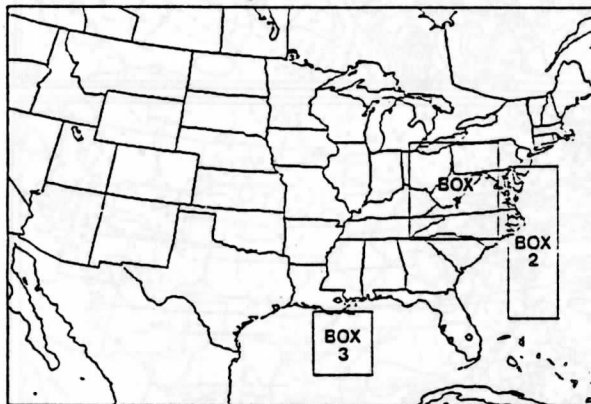

Fig. 7. Areas of precipitation for statistical calculations.

In Experiment 1, accumulations were much lower than those of the control, especially in boxes 2 and 3, where moisture values at 1800 GMT had been reduced by the smoothing process. In these two boxes, accumulations were only 24-30% of the control values. One precipitation maximum was reduced by 50%, and two other maxima found in the control were not forecasted in Experiment 1. Precipitation rates lagged behind the control forecast, and areal coverage was reduced to 68-77% of the control.

The reduced vertical motions of Experiment 2 resulted in lower accumulations that were 40-45% of the control values for the three boxes. Precipitation maxima for this experiment were positioned well when compared to the control, but most maxima were much lower. Area coverage was also reduced, while precipitation rates generally lagged behind the control.

As would be expected, Experiment 3, both lacking initial vertical motion and having lower initial moisture values than the control forecast in the precipitation regions, produced the lowest precipitation accumulations of the three experiments. Fig. 8 reveals that Experiment 3 yielded much lower average accumulations and precipitation rates than the control, with Box 2 having the largest differences. Average accumulations at the end of the forecast were only 4-22% of those from the control forecast, and precipitation covered 6-43% of the control's area of precipitation. This experiment missed completely the precipitation centers over the Atlantic and in the Gulf that were forecasted by the control (Fig. 6b). After beginning with primarily "synoptic scale" conditions, the model was unable to recover in the six-hour period and regenerate the mesoscale fields necessary to

139

yield detailed precipitation features and higher levels of precipitation accumulation.

An interexperimental precipitation comparison supports the results previously discussed. Comparing the precipitation forecasts between Experiments 2 and 3 shows the effects of smoothing the initial moisture fields, just as done by the comparison between Experiment 1 and the control. Fig. 8 shows that the average accumulations in Experiment 3 were, at most, 50% of the accumulations in Experiment 2. Areas of precipitation were also reduced in Experiment 3. Comparing Experiment 3 with Experiment 1 also showed the effects of suppressing the initial vertical velocities. Again, precipitation accumulations, rates, and areal coverage were reduced significantly. These comparisons are indeed consistent with the comparisons between the control and each experiment.

6. CONCLUSIONS

Four simulations were made with a numerical mesoscale model to determine the effects of suppressing the initial mesoscale information in the moisture and wind fields on the precipitation forecasts. The latter half of a 12-hour control forecast represented an ideal forecast that was "initialized" with fields containing mesoscale as well as synoptic scale structure. The three experiments were degraded versions of this ideal initialization and their forecasts were compared to the control forecast during the period from 1800 GMT 6 March to 0000 GMT 7 March 1982.

The characteristics of the precipitation forecasts of the experiments are not different enough to conclude that either mesoscale moisture or mesoscale vertical velocity at the initial time is more important for producing a forecast closer to that of the control. For example, at the end of the forecast, the average precipitation accumulation over a land area in the smoothed moisture experiment was 67% of the control forecast, while the non-divergent experiment produced accumulations that were 45% of the control. Over the oceans, however, the smoothed moisture experiment produced 24-30% of the control forecast, less than the nondivergent experiment, which produced 40-44% of the control forecast. No general statements can be made about this study, therefore, except to say that degrading one or both of these initial fields produces a drier forecast when compared to the control forecast. First of all, comparisons were made for only a six-hour period, and this may not have been sufficient time for the model to recover from the modifications made. Secondly, these experiments were performed on one case only, with just one model, and as such, generalizations regarding the relative worth of initial moisture and vertical velocities are inappropriate.

This research points out the need for proper initialization of mesoscale moisture and vertical motion information so that more accurate precipitation forecasts may be obtained. Improvement of the data base that is analyzed should be very helpful. More detailed moisture
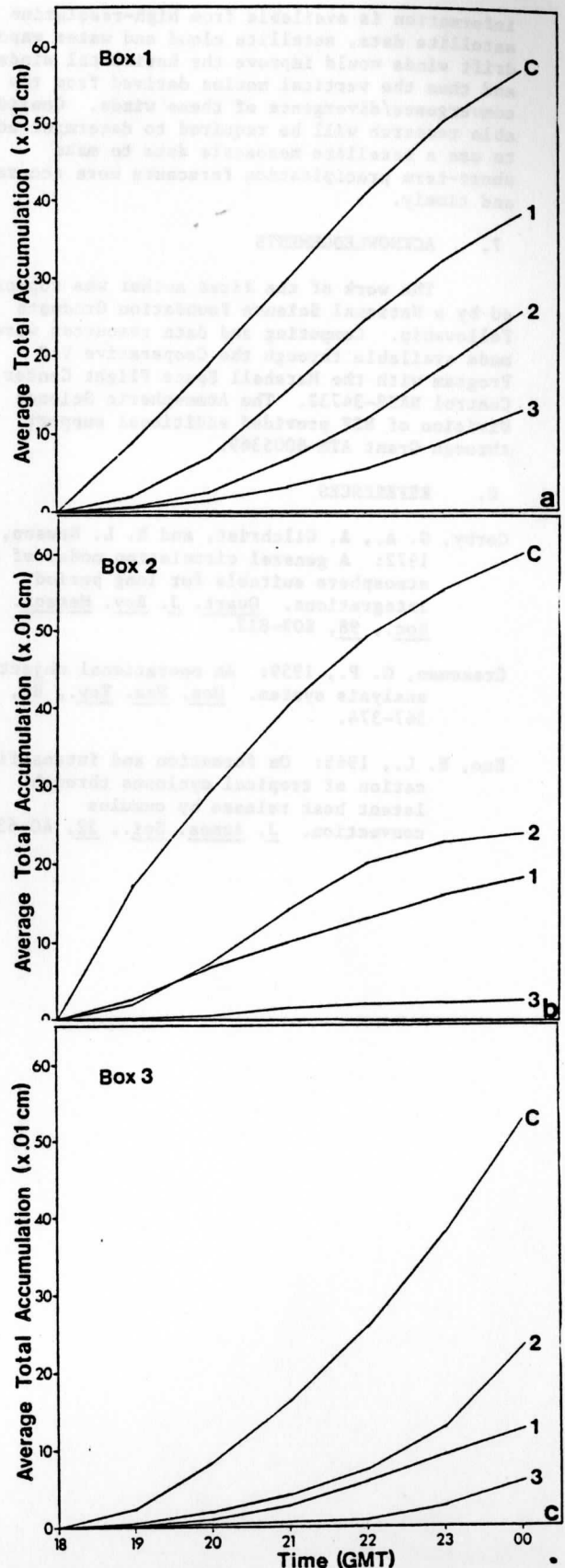

Fig. 8. Area-averaged precipitation accumulations (hundredths of cm) as a function of time for the control forecast (c) and the experiment for (a) Box 1, (b) Box 2, (c) Box 3.

information is available from high-resolution
satellite data, satellite cloud and water vapor
drift winds would improve the horizontal winds,
and thus the vertical motion derived from the
convergence/divergence of these winds. Consider-
able research will be required to determine how
to use a satellite mesoscale data to make
short-term precipitation forecasts more accurate
and timely.

7.   ACKNOWLEDGEMENTS

8.   REFERENCES

Corby, G. A., A. Gilchrist, and R. L. Newson,
        1972: A general circulation model of the
        atmosphere suitable for long period
        integrations. Quart. J. Roy. Meteor.
        Soc., 98, 809-832.

Cressman, G. P., 1959: An operational objective
        analysis system. Mon. Wea. Rev., 87,
        367-374.

Kuo, H. L., 1965: On formation and intensifi-
        cation of tropical cyclones through
        latent heat release by cumulus
        convection. J. Atmos. Sci., 22, 40-63.

_____, 1974: Further studies of the
        parameterization of the influence of
        cumulus convection on large scale flow.
        J. Atmos. Sci., 31, 1232-1240.

Le Marshall, J. F., W. L. Smith, and G. M.
        Callan, 1985: Hurricane Debby--an
        illustration of the complementary nature
        of VAS soundings and cloud and water
        vapor motion winds. Bull. Amer. Meteor.
        Soc., 66, 258-263.

McGregor, J. L., L. M. Leslie, and D. J.
        Gauntlett, 1978: The ANMRC limited-area
        model: Consolidated formulation and
        operational results. Mon. Wea. Rev.,
        106, 427-438.

Mills, G. A., 1981: An objective limited-area
        analysis/prognosis experiment using FGGE
        data in the Australian region. Mon.
        Wea. Rev., 109, 1898-1913.

Sasaki, Y., 1958: An objective analysis based
        on the variational method. J. Meteor.
        Soc. Japan, 36, 875-883.

_____, 1970: Some basic formalisms in
        numerical variational analysis. Mon.
        Wea. Rev., 98, 875-883.

Seaman, R. S., R. L. Falconer, and J. Brown,
        1977: Applications of variational
        blending technique to numerical analysis
        in the Australian region. Aust. Meteor.
        Mag., 25, 3-23.